An Experimental Study of Methane Hydrates in Sandstone Cores

Master Thesis in Reservoir Physics
By
Stian Almenningen

Department of Physics and Technology
University of Bergen

May 2015

Summary

Natural gas hydrates exist in large quantities around the world, located in the subsurface of permafrost and oceanic environments. Future energy harvest from production of methane gas encapsulated in natural gas hydrates can be made viable through extended research on fundamental characteristics of hydrates and proposed production schemes. Experimental studies of hydrates on core-scale give fast and valuable input to aid in planning of field tests, and the controlled environment in which laboratory tests are conducted enables the possibility to look at individual parameters. In this thesis methane gas hydrates have been formed in sandstone cores with high intrinsic permeability. The initial brine salinity has been kept at 3.50 wt% sodium chloride and initial water saturation has ranged between 0.57-0.70 [fraction of pore volume]. Three cores were subsequently injected with a mixture of 60% N_2 + 40% CO_2 [mole percent] and pure nitrogen to induce recovery of methane gas, and the potential of fluid flow through the cores were especially examined. A stepwise pressure reduction scheme was performed on cores containing both pure methane hydrates and mixed CH_4 + CO_2 hydrates. The pressure depletions were conducted from one end of the cores, and differential pressures were monitored along with recognitions of dissociation pressures. One MRI (magnetic resonance imaging) experiment was performed using cyclopentane hydrates at atmospheric pressure for initial testing of a new MRI instrument.

The formation of hydrates was conducted with temperatures varying between 0-4 °C, and the final hydrate saturation seemed to increase when formation temperatures were less than approximately 1 °C. Salinities and initial water saturations were kept fairly constant, but the results have been implemented with earlier research conducted by the hydrate research group at the Department of Physics and Technology. The observed trends related to hydrate growth can be summarized as followed: increased hydrate saturation for intermediate initial water saturations in the range of 0.50-0.70 [frac.], increased final water saturation with increased initial water saturation and increased hydrate saturation with decreased initial brine salinity. Two hydrate formations were complemented with resistivity measurements which indicated different growth patterns.

One successful CH_4-CO_2 exchange was carried through with injection of 60% N_2 + 40% CO_2 [mole percent]. Initial injection of pure nitrogen gas led to a vanishing differential pressure, and a conservative estimate of methane recovery from hydrates of 0.25 was obtained after injection of 3.5 pore volumes [frac.]. It was attempted to inject pure nitrogen in two other cores with the result of an immediate build-up of differential pressure due to clogging. Injectivity could only be regained by thermal stimulation inducing hydrate dissociation. This serves as evidence of nitrogen's incapability of guaranteeing fluid flow in hydrate-filled cores with excess water.

Stepwise pressure reductions showed that hydrate dissociation occurred at slightly elevated pressures compared with theoretical dissociation pressures. The observed dissociation pressures were not distinct and methane gas was liberated through a pressure range below the start of dissociation. The effect of a decreasing salinity is believed to contribute the most to gradual dissociation in core experiments containing a conserved mass of salt.

Acknowledgements

First of all I would like to thank my supervisor Associate Professor Geir Ersland for introducing me to the thrilling topic of gas hydrates and for providing me with an exciting task. Your relaxed way of being inspires to good dialogue and no question was too silly to ask.

I would also like to thank Professor Arne Graue who has contributed to make my research on gas hydrates possible and Associate Professor Martin Fernø for always giving good advices.

Thanks to PhD candidates Lars Petter Øren Hauge and Jarand Gauteplass for patiently answering my questions. The guidance from Lars Petter on both experimental work and numerical calculations has been invaluable.

Thanks to Chief Engineer Rachid Maad and the personnel at the mechanical workshop for fixing damaged equipment and for assistance with experimental design.

I would also like to thank fellow students at the department for a good working environment and for much laughter through the years. I would like to give a special thanks to fellow student Erik Vadla who has accompanied me through many hours at the laboratory and who has made my work with this thesis more cheerful.

Finally I would like to thank my family and friends for endless support and for always believing in me.

Thank you!

Table of Contents

Introduction

Natural gas hydrates are crystalline compounds existing at low temperatures and elevated pressures. The cage-like framework is constituted by hydrogen-bonded water molecules and is stabilized by non-polar guest molecules. Typical guest molecules will be methane, ethane, CO_2 and nitrogen, where methane is most predominant in nature. Natural gas hydrates are found all over the world and are mainly located in permafrost regions and in offshore sediments. This is where temperature and pressure settings coincide with hydrate stability, and where methane concentrations are high enough for hydrate formation.

The total amount of energy stored in natural gas hydrates is predicted to be twice as large as the energy-equivalent in conventional fossil fuels, i.e. natural gas, oil and coal (Kvenvolden, 1988). This is the main reason for a growing interest on natural gas hydrates during the last decades, especially in countries like Japan, South-Korea and China, seeking to be self-sustained in energy. In other countries, e.g. Norway, natural gas hydrates are seen as a possible energy resource satisfying the growing energy need. The global energy demand is expected to increase by 37% by 2040, and the energy supply mix is anticipated to exist of four almost-equal parts: oil, gas, coal and low-carbon sources (International Energy Agency, 2014). This scenario will lead to an increase in energy-related CO_2 emissions by one-fifth (International Energy Agency, 2014). Exploitation of natural gas hydrates can contribute to decrease the necessity of oil and coal, and thereby assist in mitigation of CO_2 emissions. Methane gas is known to be the cleanest fossil fuel on combustion (Environmental Protection Agency US, 2013), and one proposed production technique has the additional benefit of injection and partial sequestration of CO_2.

The most promising production technique is considered to be pressure depletion and has been extensively tested on both small-scale and field-scale. The pressure is lowered below the hydrate stability line and the hydrate dissociates into liquid water and methane gas. This is of particularly interest when the hydrate reservoir is in contact with a free gas reservoir. Free gas can then be produced and the corresponding decrease in pressure will lead to dissociation of hydrates and subsequent replenishment of new gas. One key issue in this production scenario is sufficient permeability to allow for pressure perturbations to reach inside the hydrate reservoir and to allow for flow of dissociated gas. This problem has been addressed in this thesis by looking at controlled pressure depletions conducted on sandstone cores. Other drawbacks with the depressurization method are associated water production and possible geomechanical instabilities.

Another production scheme is based on the spontaneous conversion from methane hydrate to CO_2 hydrate as gaseous/liquid CO_2 is introduced to preexisting methane hydrate. The exchange technique, compared to pressure depletion, thermal stimulation and inhibitor injection, benefits of no large-scale dissociation and storage of a greenhouse gas (Graue *et al*., 2008). The conversion process was first introduced by Ohgaki *et al*. (1994) and has undergone considerable research the last two decades. In 2011-2012, a successful field trial was commenced on the North Slope of Alaska, demonstrating the viability of CH_4-CO_2 exchange as a future exploitation method (Schoderbek *et al*., 2012). Potential sources of concern include reformation of CO_2 hydrates with excess water which leads to a reduction in permeability. Nitrogen gas can be used to mitigate this problem and this has been investigated in this thesis. The rate and magnitude of conversion is also of important significance and will affect the potential of CH_4-CO_2 exchange as a production method.

x

1 Fundamentals

1.1 Natural gas hydrates

1.1.1 The water molecule

The water molecule is comprised of two hydrogen atoms and an oxygen atom with an H-O-H angle of 104.5° (Sloan, 1998). The hydrogen atom has the electron configuration $1s^1$ and is missing one electron to fulfill the orbital. The oxygen atom has the electron configuration $1s^2 2s^2 2p^4$ and is missing two electrons to fulfill the second electron shell. Accordingly, each of the two hydrogen atoms will form single covalent bonds to the oxygen atom. The electron pair in each covalent bond will reside closer to the oxygen atom due to difference in electronegativity between hydrogen and oxygen atoms. On the Pauling scale, oxygen and hydrogen have electronegativities of 3.44 and 2.20, respectively (Allred, 1961). It follows that the oxygen atom has a negative charge of approximately 0.7e and the two hydrogen atoms divide the equal positive charge equally (Chaplin, 2014). This charge distribution within the water molecule gives rise to attractions between hydrogen atoms and oxygen atoms residing on different water molecules, known as hydrogen bonds. Each oxygen atom can bond with two hydrogen atoms and the two hydrogen atoms can bond with one oxygen atom each, resulting in a total of four hydrogen bonds from one water molecule, as illustrated in Figure 1.1.1.
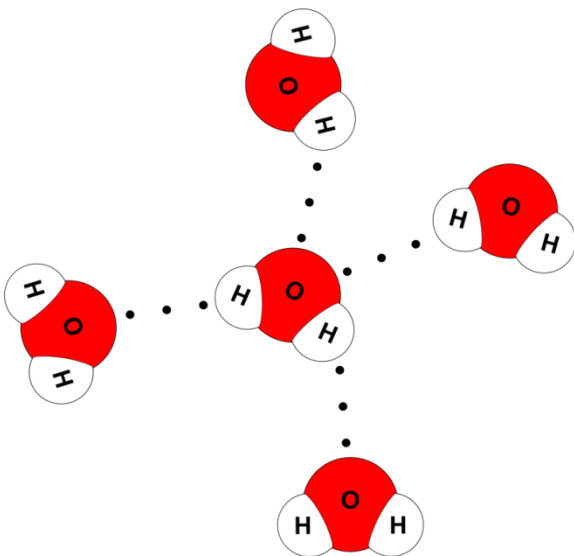
Figure 1.1.1: Hydrogen bonding between water molecules (Conn, 2012).

"The strengths of hydrogen bonds (≈ 5 kcal/mole) are normally intermediate between those of weak van der Waals interactions (≈ 0.3 kcal/mole) and those of covalent chemical bonds (≈ 100 kcal/mole)" (Stillinger, 1980). The relative high strength of hydrogen bonds explain some of the notable physical properties displayed by water (excerpt from Stillinger (1980)): (i) negative volume of melting; (ii) density maximum in the normal liquid range (at 4°C); (iii) numerous crystalline polymorphs (at least

nine, including those that form at elevated pressure); (iv) anomalously high melting, boiling, and critical temperatures for a low-molecular-weight substance that is neither ionic nor metallic.

1.1.2 Hexagonal ice and similarities to hydrates

There are up to sixteen known forms of ice (Finney, 2006), but the most common solid form of water is known as hexagonal ice (ice Ih). In ice Ih each water molecule is hydrogen bonded to four others with an O-O-O angle of 109.5°. The tetragonal hydrogen-bonded water molecules form in non-planar hexagonal rings, rather than planar sheets. In comparison, natural gas hydrates consist of approximately 85 mole per cent water in tetrahedral structures similar to that of ice (Sloan, 1998). With such high water contents, the properties of natural gas hydrates and ice Ih are very similar. The differences in bulk and shear modulus are very small, and this makes it difficult to differentiate between ice and hydrates in the reservoir by use of seismicity. One of the most distinguished features between ice and hydrates (except that hydrates can burn) is the thermal conductivity, where ice has a thermal conductivity of approximately five times higher than that of gas hydrates (Sloan, 1998). The mechanical strength of hydrates is 20 times stronger than ice Ih (Durham *et al.*, 2003).

1.1.3 Hydrate structures and cavities

Natural gas hydrates consist of water molecules which are hydrogen-bonded in a structured way and stabilized by guest molecules. Dependent upon the type of guest molecule, the hydrates will contain different cavities yielding different hydrate structures, see Figure 1.1.3. The basic building block, present as the small cavity in all hydrate structures, is the pentagonal dodecahedron. The cavity arises when combining twelve pentagons and is denoted 5^{12}. The next cavity type, tetrakaidecahedron, consists of twelve pentagonal and two hexagonal faces and is denoted $5^{12}6^{2}$. These two cavity types are the building blocks of the most common hydrate structure called structure I (SI). The SI cubic cell is a result of vertex-linking of the 5^{12} cavities in three dimensions, and consists of two small cavities (5^{12}) and six large cavities ($5^{12}6^{2}$) with a total of 46 water molecules (Sloan, 1998).

When the 5^{12} cavities are face-shared in three dimensions, the spaces between the cavities will form the larger cavities $5^{12}6^{4}$. These cavities are made up of twelve pentagonal and four hexagonal faces and are called hexakaidecahedron. Structure II (SII) hydrate consists of 16 small cavities (5^{12}) and eight large cavities ($5^{12}6^{4}$) with a total of 136 water molecules within each cubic cell. In addition to SI and SII, it has been proposed a list of five hydrate structures, possibly more, but these have not yet been formed with hydrocarbons as guest molecules. The hydrate structure known as the third structure, SH, consists of hexagonal space cells and is made up of three small cavities (5^{12}), two medium cavities ($4^{3}5^{6}6^{3}$) and one large cavity ($5^{12}6^{8}$) with a total of 34 water molecules (Sloan, 1998).
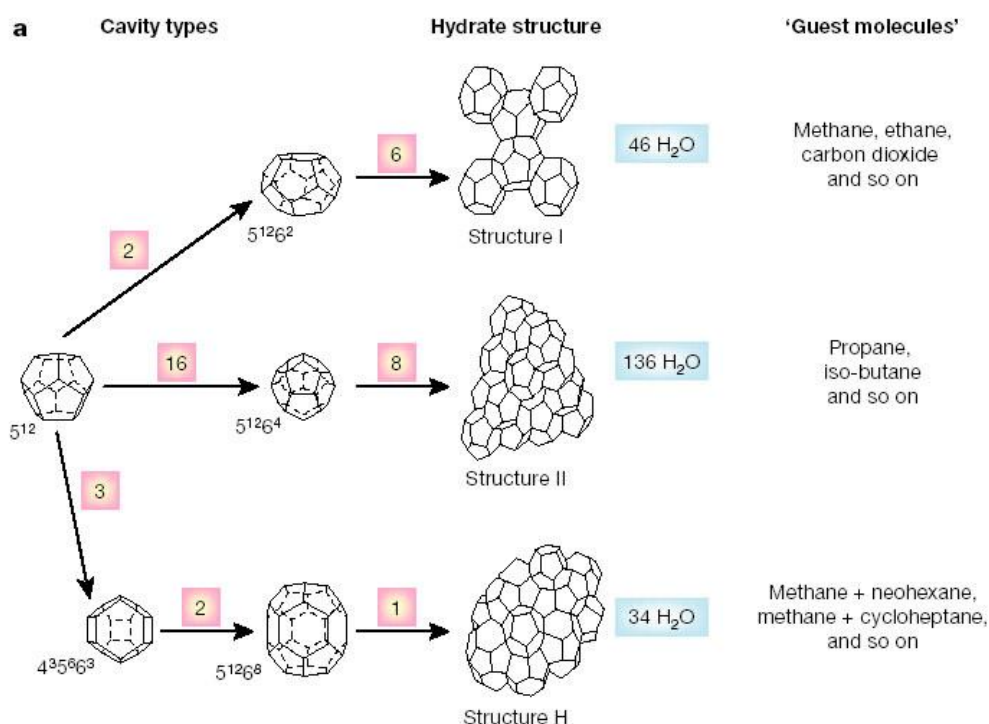
b

Hydrate crystal structure	I		II		H		
Cavity	Small	Large	Small	Large	Small	Medium	Large
Description	5^{12}	$5^{12}6^2$	5^{12}	$5^{12}6^4$	5^{12}	$4^3 5^6 6^3$	$5^{12}6^8$
Number of cavities per unit cell	2	6	16	8	3	2	1
Average cavity radius (Å)	3.95	4.33	3.91	4.73	$3.91^†$	$4.06^†$	$5.71^†$
Coordination number*	20	24	20	28	20	20	36
Number of waters per unit cell	46		136		34		

*Number of oxygens at the periphery of each cavity.
†Estimates of structure H cavities from geometric models.

Figure 1.1.3: Hydrate structures and cavities (Sloan, 2003).

1.1.4 Hydrate guest molecules

Natural gas hydrates cannot form without the presence of guest molecules. The guest molecules will enter the water cavities and prevent the cavities from collapsing by van der Waals interactions. For this reason the guest molecules are constrained both in chemical composition and size. In order not to interfere with the hydrogen bonds between water molecules, the guest molecules must contain neither a single strong hydrogen-bond group, nor a number of moderately strong hydrogen bonding groups (Sloan, 1998). Jeffrey and McMullan (1967) proposed a scheme for a chemical subdivision of guest molecules, where the two first groups were denoted 1) hydrophobic compounds and 2) water soluble acid gases. Of the gases studied in this thesis, methane and nitrogen will belong to group one and CO_2 will belong to group two.

With respect to molecular size, the guest molecule must be big enough to contribute to cavity stability, but at the same time be able to fit into the cavity without distortion. The guest molecules must have a ratio of molecular to cavity diameter of about 0.76 to 1.0 (Sloan, 1998). Methane has a molecular diameter of 4.36 Å and will stabilize the 5^{12} cavities of structure I and also occupy all of the

large $5^{12}6^2$ cavities. Methane will not be able to stabilize the bigger $5^{12}6^4$ cavities of structure II and forms structure I. CO_2, which has a molecular diameter of 5.12 Å, will not fit into the small 5^{12} cavities but will give best stabilization to the $5^{12}6^2$ cavities of structure I. Nitrogen, being the smallest natural gas hydrate former, will give better stabilization to the 5^{12} cavities of structure II rather than the slightly bigger 5^{12} cavities of structure I. Since structure II has a fractionally higher number of small cavities in the unit cell, nitrogen will form structure II (Sloan, 1998).

The above discussion of guest size and hydrate structure is only valid for simple hydrates, i.e. hydrates with only one guest species. It is also possible to have mixed hydrates, in which cages of the same kind are occupied by two types of molecules, with the restriction of at most one molecule per cage (Sloan, 1998). This implies the possibility of having mixed hydrates where methane occupies the small cages and some of the large cages, and CO_2 occupies the rest of the large cages (Ota *et al.*, 2005).

The hydration number, n_w, is the ratio between water molecules and guest molecules in a unit cell of the hydrate (Sloan, 1998). For structure I, the ideal value will be n_w = (46 water molecules/(2+6) guest molecules), giving a hydration number of 5.75. But studies (Anderson, 2004; Circone *et al.*, 2005) have shown that hydrates will experience non-stoichiometry and all of the cavities will not be filled. Circone *et al.* (2005) have measured the hydration number to be 5.99(±0.07) for similar temperatures and pressures (0-4 °C and 83 bar) as in experiments conducted in this thesis, and this value of hydration number will be used for later calculations.

1.1.5 Hydrate stability

When water and guest molecules are present, there must exist a thermodynamic driving force for hydrates to form. For natural gas hydrates, this means low temperatures (< 10 °C) and high pressures (> 30 bar). The actual temperature and pressure range where the hydrate is stable will be given by the composition of hydrate (type of guest molecule), but can also be altered by thermodynamic inhibitors. Figure 1.1.5 shows hydrate stability regions as functions of temperature and pressure for the three guest molecules used in this thesis. CO_2 is the most stable hydrate former below 10 °C because methane needs a higher pressure to form hydrate. In region four, both methane and CO_2 hydrate will be stable and when both gases are present a mixed hydrate will form. But when methane hydrate (structure I) within region four is introduced to CO_2, the more stable hydrate former will enter the large cavities and a spontaneous exchange between CO_2 and methane will occur (Ota *et al.*, 2005). At even more elevated pressures (> 100 bar), all of the three gases will form hydrate. In order not to enter the stability region of pure nitrogen hydrates, the experiments in this thesis are conducted with a temperature between 0 and 4 °C and a pressure of 83 bar. These conditions will also exclude the possibility of forming ice.
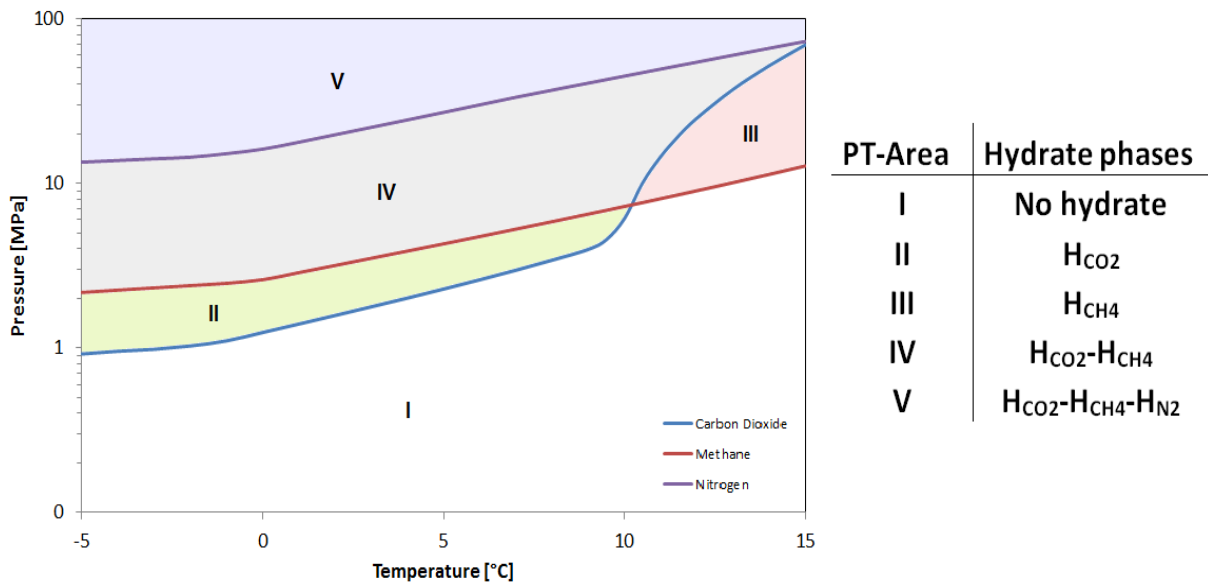
Figure 1.1.5: Hydrate stability regions for different guest molecules. Modified from Husebø (2008).

1.1.6 Hydrate formation and dissociation

Hydrate formation can commence once the water and guest molecules are within hydrate stability conditions. The formation of hydrates can be divided into nucleation, induction time and growth with reference to Figure 1.1.6.
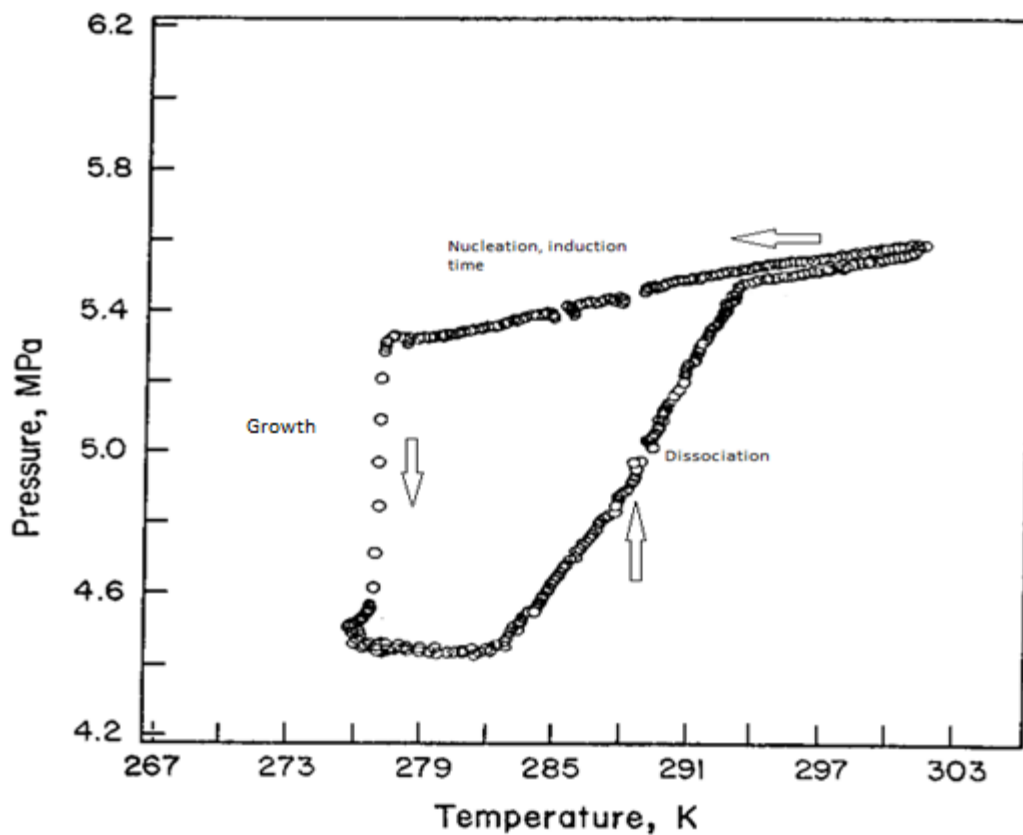
Figure 1.1.6: Temperature and pressure trace for formation of simple hydrates. Modified from Sloan (1998).

15

Nucleation

Hydrate nucleation is the process, during which small hydrate crystals grow and disperse in an attempt to achieve critical size for continued growth. The nucleation is governed by the minimization of Gibbs free energy which is a competition between surface excess free energy and volume excess free energy (Sloan, 1998). For a spherical hydrate crystal it can be written as (Kvamme, 2014):

$$\Delta G = \Delta G^{surface} + \Delta G^{phase\ trans.} = 4\pi r^2 \gamma + \frac{4}{3}\pi r^3 \rho_N^H \Delta g^{phase\ trans.} \leq 0 \qquad (1.1.6)$$

where Υ is the interfacial free energy [J/m^2], r is the crystal radius [m], ρ_N^H is the molecular density [mole/m^3] and $\Delta g^{phase\ trans.}$ is the intensive change in Gibbs free energy related to the phase transition [J/mole]. The favorable negative free energy change from the phase transition must overcome the penalty from creating new surface area. Once the critical size is achieved, the Gibbs free energy change is solemnly negative and the hydrate nuclei start to grow without dispersing. The critical size has been modelled from simulation to be a couple of nanometers and can be reached within nanoseconds (Kvamme, 2014). It is thus very difficult to observe experimentally.

Nucleation can be divided into homogenous and heterogeneous nucleation. Homogenous nucleation is a solidification process in the absence of impurities which involves many more molecules than could collide simultaneously. This involves guest molecules dissolved into a pure water phase without impact from the solid material containing the water phase. This is very uncommon, or virtually impossible to achieve, so the nucleation is usually heterogeneous. Then the nucleation occurs in the presence of a foreign body or surface, and the critical size for the nuclei will in fact be lowered (Sloan, 1998). The mass transport will also be quicker for heterogeneous nucleation as the process goes from three dimensional to two dimensional on the foreign surface (Kvamme, 2014). In a porous media, the nucleation will indeed be heterogeneous as there are a lot of possible nucleation sites and an abundant amount of impurities.

Induction time

Induction time (lag time) is often used in literature as a synonym for nucleation time. This is incorrect as induction time is the timespan from hydrate stability is reached until onset of massive growth. Compared to nucleation which is a microscopic (nanoscale) phenomenon, induction time is a macroscopic event and is determined by visual hydrate growth. The induction time will depend on type of hydrate measurements, for example human visual inspection, and is often in the time range of minutes or hours (Kvamme, 2014). But the induction time will vary independent of measuring device and is a stochastic event. Haymet and Barlow (2006) observed a stochastic variation in induction time for identical freezing of water, and one would expect more difficulties with prediction of a more complex system like gas hydrates (≥2 components and ≥2 phases). The system becomes more predictable with increasing driving forces, i.e. higher degree of supercooling (Sloan, 1998).

Growth

After the stochastic nature of hydrate crystal nucleation and induction time, hydrates will start to grow. The growth rate will be governed by availability of water and guest molecules and a coupling of mass transport and heat transfer (Kvamme, 2014). Adding of hydrate inhibitors will also affect the growth rate and will be discussed later. Hydrate formation is an exothermic process and the released heat can induce local temperature increases which counteract the formation. The experiments in this thesis are conducted with constant temperature, and good heat transfer throughout the core is

assumed. The most limiting factor will be mass transport and availability of water and guest molecules, since initial hydrate films at the interface will act as transport barriers for further growth (Kvamme, 2014).

The growth period is characterized by a sudden decrease in pressure in Figure 1.1.6, as the gas is volumetrically concentrated by a factor of 164 when entering the hydrate (Moridis *et al.*, 2009). Another possibility is to keep the pressure constant by injecting gas during the hydrate formation. The formation is then quantified by a consumption of gas and this has been done in this thesis.

Hydrate dissociation
Hydrates can be dissociated by removal of one of the hydrate components, thermal stimulation, depressurization, thermodynamic inhibiting or a mixture of these. Thermal stimulation and depressurization will bring the hydrate outside the hydrate stability region whereby the last method will shift the equilibrium line and the hydrate becomes unstable at the given temperature and pressure (Kvamme, 2014). Hydrate dissociation is carried out by an increase in temperature in Figure 1.1.6, and is followed by an increase in pressure as the gas is released from the hydrate. The dissociation of hydrates is an endothermic reaction and the heat acquired can induce local temperature reductions. Dissociation of hydrates as a production method will be discussed later.

1.1.7 Hydrate inhibition

All of the above processes for dissociation of hydrates are a part of hydrate inhibition, but this chapter will mainly deal with thermodynamic inhibitors. Thermodynamic inhibitors will make a shift in the equilibrium line by reducing the chemical potential of water. The water molecules will seek to minimize the energy and will favor the phase in which they have the lowest chemical potential. The chemical potential for water inside the hydrate is given by the great canonical ensemble (Kvamme, 2014):

$$\mu_w^H = \mu_w^{H,0} - RT \sum_i v_i ln \left(1 + \sum_j h_{ij} \right)$$

(1.1.7a)

where $\mu_w^{H,0}$ is the chemical potential of water in empty hydrate [J/mole], v_i is the fraction of cavity type *i* per water and h_{ij} is the cavity partitioning function for guest molecule type *j* in cavity *i*. This is usually given by:

$$h_{ij} = c_{ij} f_j^H$$

(1.1.7b)

where c_{ij} is the Langmuir constant and f_j^H is the fugacity of guest molecule type *j* in the hydrate. The chemical potential of water in the liquid phase is given by (Atkins and De Paula, 2010):

$$\mu_w^{liq} = \mu_w^{pure\ liq} + RT ln(x_w \gamma_w)$$

(1.1.7c)

where x_w is the mole fraction of water in the liquid phase and γ_w is the activity coefficient of water. Adding a thermodynamic inhibitor to the system will lower the mole fraction of water as well as the activity coefficient of water in the liquid phase. From Eq. 1.1.7c, this implies a reduction of the

chemical potential of water in the liquid phase and when the value becomes lower than the chemical potential given by Eq. 1.1.7a, the hydrate will dissociate.

The most common thermodynamic inhibitors include alcohols, glycols and salts. Alcohols and glycols will hydrogen bond with the water molecules and thereby lower the water activity. Salts will create electrostatic ion-dipole bonds with the water and lower the activity even more. The reduction is stronger for divalent ions than monovalent ions (Kvamme, 2014). All the experiments in this thesis are conducted with water containing 3.50 wt% sodium chloride, which is a good approximation to normal seawater (Anderson, 2008). Nitrogen gas can also act as a thermodynamic inhibitor and can dissociate more stable hydrate species like methane and CO_2 hydrates. Nitrogen gas dilutes the hydrate guest molecules in the gas phase and makes the hydrate to dissociate towards the gas phase where the chemical potential is lower (Kvamme, 2015).

Kinetic inhibitors and anti-agglomerates can prevent, or at least delay hydrate growth, and are used in industry to prevent hydrate plugging in gas transportation. Most of the kinetic inhibitors are polymer-surfactants and one mechanism of which they act is steric blocking of water molecules (Kvamme, 2014).

1.2 Hydrates in nature

1.2.1 Hydrates as an energy resource

During the beginning of the twentieth century, the research on gas hydrates focused mainly on identifying hydrate guests and corresponding compositions. Gas hydrates were seen as a problem in industrial equipment with potential to block and damage flow lines. In the 1960s it was recognized that methane-rich gas hydrates exist in large quantities in nature. Over time, estimated reserves have varied from 530 000 Gt C to a minimum estimate of 100 Gt C. Current estimates show hydrates could contain from 10^{15} to more than 10^{17} m^3 of methane at standard temperature and pressure. This equals a range from 500 to 63 400 Gt C. These refined estimates are based upon both empirical observations and more recently mechanistic models (Hester and Brewer, 2009). Kvenvolden (2002) has reported the worldwide fossil fuel reserves to be 5000 Gt C, which indicates that the amount of hydrated methane can be as high as twelve times that of conventional fossil fuels (coal, oil and natural gas). The conventional natural gas accumulations are estimated to be 1.2x10^{14} m^3 (Ahlbrandt, 2002), about one tenth of the conservative estimate of methane gas in hydrates. These examples show the enormous energy potential of gas hydrates, but one has to take into consideration whether the accumulations are technically recoverable and economically producible.

1.2.2 Hydrate formation in nature

Methane gas is the most common hydrocarbon source for formation of hydrates in nature. However, it has been reported of instances of hydrate formation from hydrocarbon liquids, but this process is rare and is not considered further. The origin of methane gas stems from either thermogenic or biogenic generation. Thermogenic generation is characterized by high temperatures (>373 K) and is the source for most of the natural gas reservoirs. As a result of the high catagenesis temperature, the gas has to migrate a long pathway to enter the hydrate stability region and hence thermogenic hydrates are not common in nature. Biogenic methane gas stems from a low temperature, organic

diagenesis. This process involves many stages in which organic matter is oxidized and reduced to give a number of products. One of the products is methane gas characterized by low contents of ethane and propane. This is one way of differentiating between biogenic methane and thermogenic methane. Another method suitable to differentiate between the gases is based on the ratio difference between different carbon isotopes (Sloan, 1998).

Once the methane is produced, density differences cause it to percolate upwards either as free gas or as gas-saturated water. Eventually, if not already created inside, the methane will enter the region of hydrate stability. If then the upward moving methane is sealed by an impermeable layer of rock which causes the methane to reside inside the stability region, methane formation can take place (Sloan, 1998).

There exist three different models of hydrate formation in nature. The first one is based on formation by *in situ* produced biogenic methane. To date, there is no agreement between researchers on the amount of hydrate resulting from this process. The second model is based on formation by migration of free gas. The free gas may come from biogenic produced gas or from hydrates that have been dissociated by progressive burial through time. Formation of hydrates by free gas bubbles has been verified experimentally. The last model is based on formation from gas dissolution of upward moving water. As the rising under-saturated water experiences lower temperature and pressure, the water gets supersaturated with methane and enables hydrate formation. This model is also under debate regarding the obtainable methane concentration and expected hydrate saturation, and comprehensive solubility data are needed (Sloan, 1998).

1.2.3 Hydrate accumulations

To date, more than 90 sites have been directly or indirectly identified to contain natural gas hydrates. Inferred hydrate deposits are identified with indirect hydrate markers, mainly from seismic reflectors and pore-water freshening in core samples. Known hydrate deposits are areas where hydrates have been directly sampled from ocean drilling and remote-operated vehicle expeditions (Hester and Brewer, 2009). Makogon (2009) reports of more than 230 gas hydrate deposits around the world, shown in Figure 1.2.3a.
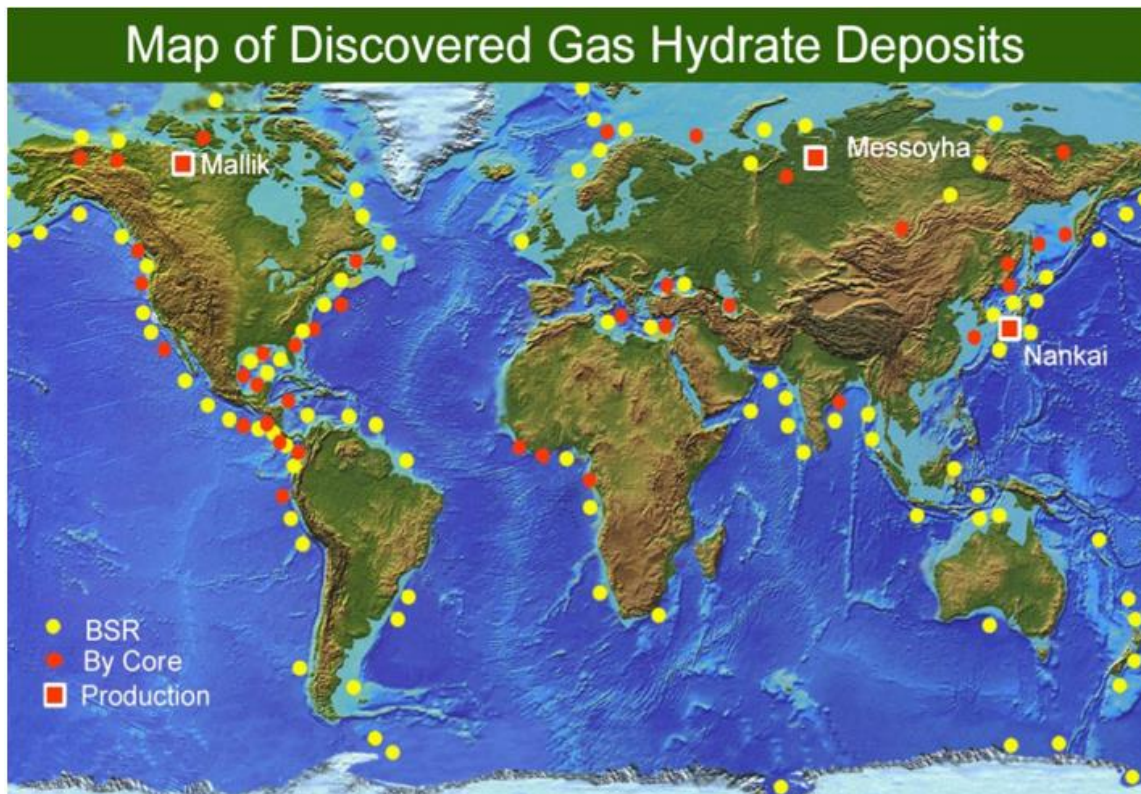
Figure 1.2.3a: Distribution of discovered gas hydrate deposits. BSR = bottom simulating reflector. The Mallik and Nankai sites have only performed test-production (Makogon, 2009).

Most of the hydrate deposits are located in oceanic and permafrost sediments where the temperature and pressure conditions are suited for hydrate formation. This is illustrated in Figure 1.2.3b.
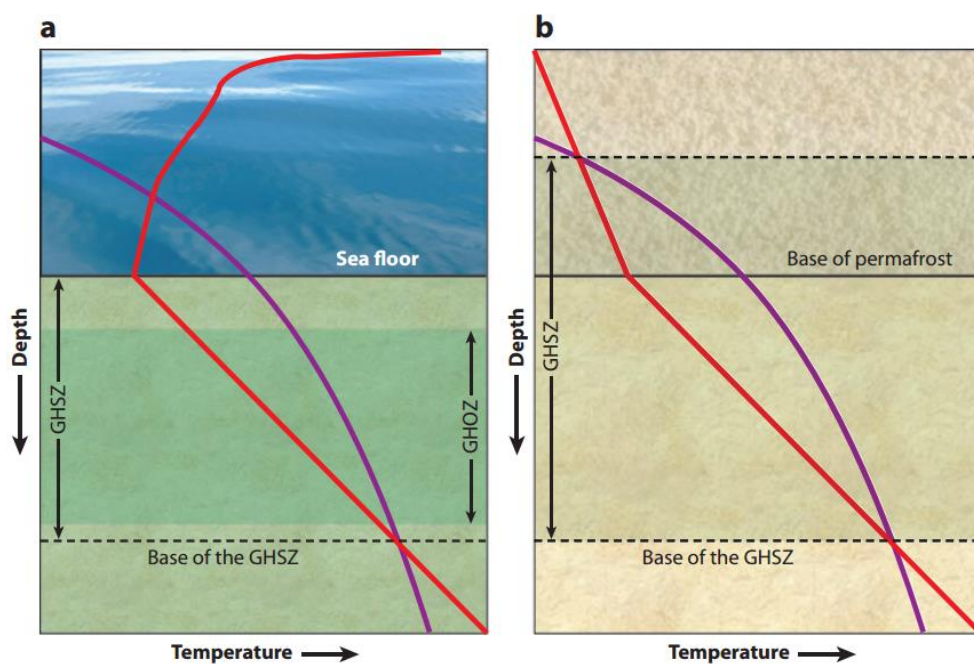
Figure 1.2.3b: Gas hydrate stability zone (GHSZ) for (*a*) marine and (*b*) permafrost settings (Hester and Brewer, 2009).

The purple line is the hydrate stability curve and hydrates will be stable to the left of this line. The red line is the ambient temperature profile, and the gas hydrate stability zone (GHSZ) is defined by the area where the temperature profile is to the left of the hydrate stability curve.

For marine systems, the GHSZ typically begins below 300-600 m of water depth and can extend hundreds of meters below the sea floor, with a general temperature range from 2 to 20 °C. Just below the sea floor, sulfate reduction and anaerobic oxidation of methane lead to methane concentrations below saturation limits. Hydrate formation is thus limited to the gas hydrate occurrence zone (GHOZ). For permafrost systems, the GHSZ typically occurs around 100-300 m depth and can extend hundreds of meters based on the base of permafrost; the general temperature range is from -10 to 20 °C. In these settings, an ice + gas two-phase system exists until pressures are high enough to allow for hydrate formation. The GHSZ extends through the base of permafrost until temperatures exceed hydrate stability, resulting in a gas + liquid two-phase region (Hester and Brewer, 2009).

Makogon (2009) has divided the gas hydrate deposits into primary and secondary deposits. A primary deposit is one which does not melt after its formation, and are usually found in deep water. They are formed by the gases dissolved in the reservoir water, and are located in the near seafloor sediments, characterized by high porosity, low temperature and low rock strength. The hydrate begins to form in the pore space and eventually plugs the migration paths which trap more hydrates. Secondary deposits are usually located in the Arctic onshore. They are associated with natural gas reservoirs, located under the impermeable cap rocks in structural or stratigraphic traps. Upon temperature decrease in the formation, hydrates may form and overlie a region with free gas.

Another classification of hydrate accumulations that is useful for the later discussion of production methods, divides hydrate deposits into four classes. Class 1 accumulations are composed of two zones: the hydrate interval and an underlying two-phase fluid zone with free (mobile) gas. Class 2 deposits include two zones: a hydrate-bearing interval on top of a mobile water zone with no free gas. Class 3 accumulations consist of a single zone: the hydrate interval, and are characterized by the absence of an underlying zone of mobile fluids (Moridis and Collett, 2003). The fourth class (class 4) is equivalent to class 3, but the hydrate-bearing layer lacks confining strata (Moridis and Sloan, 2007). The different types of hydrate accumulations are summarized in Figure 1.2.3c.

Deposit type	Zones present	Mobile phases	Confining strata
Class 1	Two zones: hydrate-bearing layer (HBL) above two-phase zone	Free gas, water	Yes
Class 2	Two zones: HBL above one-phase zone	Water	Yes
Class 3	One zone: HBL	None	Yes
Class 4	One zone: HBL	None	No

Figure 1.2.3c: Classification system for the production of hydrate reservoirs (Hester and Brewer, 2009).

Class 1 can further be divided into class 1W and class 1G. Class 1W involves water and hydrate in the hydrate-bearing layer while class 1G involves gas and hydrate. The occurrence of class 1W is rare (Moridis *et al*., 2009) and the later discussion of class 1 is based on class 1G.

1.2.4 Hydrate accessibility

The accessibility of hydrate accumulations will depend on the geological setting from which they were formed, hydrate saturation and possible vicinity of already existing infrastructure. Boswell and Collett (2006) have presented a diversification of gas hydrate resources within the context of a gas hydrates resource pyramid. The resource pyramid displays the relative size and producibility of different hydrate accumulations, with the most promising resources at the top and the most technically challenging at the base. This is shown in Figure 1.2.4 along with a schematic and scaled resource pyramid for conventional natural gas resources to the right.
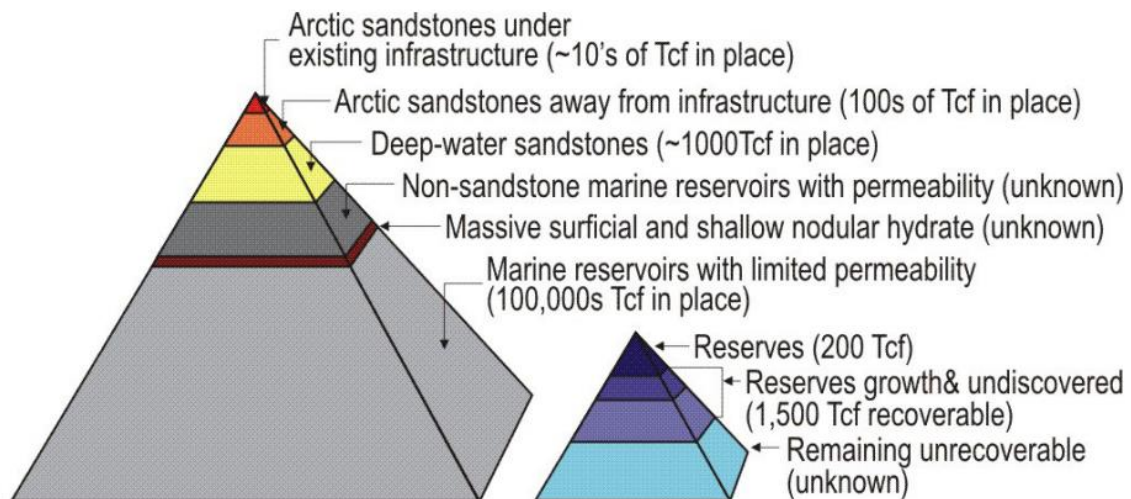
Figure 1.2.4: Gas hydrates resource pyramid (left) and an example of a gas resource pyramid for all non-gas-hydrate resources (right) at the appropriate scale (Boswell and Collett, 2006).

The following section is an abbreviated rendering of the discussion presented by Boswell and Collett (2006). The peak of the gas hydrates resource pyramid is represented by gas hydrates that exist at high saturations within quality reservoir rocks under existing Arctic infrastructure. Reservoir modelling suggests that as much as 12 Tcf of gas-in-place may be technically recoverable on the North Slope of Alaska. The next largest class of hydrate resources is those less well-defined accumulations that exist in similar geologic settings on the North Slope, but away from existing infrastructure. The current estimate for total North Slope resources is approximately 590 Tcf of gas-in-place. The next most challenging group of resources includes gas hydrates of moderate-to-high concentrations that occur within quality sandstone reservoirs in the marine environment. Because these resources will be challenged by the likely high costs of extraction from very deep water, the most favorable accumulations are those found in the Gulf of Mexico that lie in the vicinity of oil and gas production infrastructure. The next two classes of resources are massive deposits of gas hydrates generally found encased in fine-grained muds and shales, and massive gas hydrate mounds that lie exposed on the seafloor and extend to unknown depths. These classes are very uncertain, both with respect to amount and possible production methods. At the base of the pyramid are those finely-disseminated accumulations in which large volumes of gas hydrates are relatively evenly distributed through vast volumes of fine-grained and relatively undeformed sediment at low saturations. To date, there are no prospects for economic recovery of this resource class without huge improvements in the production technology.

Based on the above considerations, the most promising hydrate resources are located in sandstone reservoirs with good permeability. This is the reason why sandstone samples (porosity around 22% and permeability around 1 Darcy) have been used in this thesis.

1.2.5 Production scenarios

Production by dissociation

Gas can be produced from gas hydrates by inducing dissociation by one of the following main methods: depressurization, thermal stimulation and thermodynamic inhibiting. Depressurization is carried out by removal of reservoir fluids and is a consequence of all production wells. Thermal stimulation can be conducted by injection of steam or hot water, *in situ* combustion or radiation (Kvamme, 2014). Thermodynamic inhibitors, like alcohols, glycols and salts, must be injected into the reservoir and the mechanism for dissociating hydrates is treated in Chapter 1.1.7. Another production method involves methane exchange with another hydrate-forming gas (e.g. CO_2) through a thermodynamically favorable reaction (Moridis *et al.*, 2011). This method has been investigated in these experiments and will be discussed in the next chapter. Hydrate production can be performed with one of these techniques, but long-term production strategies often utilize a combined effect of two or more methods (Moridis *et al.*, 2011).

Moridis and Collett (2003) have investigated production from the three first classes of hydrates by numerical simulation. They found that the appeal of depressurization decreases from class 1 to class 3, while that of thermal stimulation increases. In class 1, the bottom of the hydrate stability zone usually coincides with the bottom of the hydrate interval. This necessitates only small changes in pressure to induce dissociation. One can produce free gas from the underlying layer and the corresponding pressure drop will induce dissociation of hydrates which will replenish the produced gas. The initial rate of methane release will be good and increasing with pressure drop. After a while the rate will decline as the effect of increasing depressurization is overcome by the counter-acting progressive cooling of the hydrate (Moridis and Collett, 2003). The rapid expansion of gas and the endothermic heat of hydrate dissociation might lead to formation of secondary gas hydrates or ice, and thermal stimulation or inhibitor injection will be needed (Ruppel, 2011). The Messoyakha field on the eastern border of West Siberia, is believed to be an example of a class 1 reservoir (Makogon, 2009) and will be discussed later.

Class 2 reservoirs can give more effective depressurization due to the near-incompressibility of water which yields a stronger pressure disturbance. The relatively high heat capacity of water can also provide an additional significant heat reservoir to supply the needs of the endothermic dissociation reaction. However, based on simulations class 2 hydrates reveal serious shortcomings related to water production. In single well configurations, gas production can be accompanied by water production that represents up to 98 % of the total produced mass. Disposing of such large volumes of water in environmentally sensitive areas is complicated, and the pumping out and disposing of water are expensive (Moridis and Collett, 2003). Moridis (2002) proposed an approach involving multi-well (five-spot) systems with net zero water withdrawals that could maximize production from class 2 hydrate accumulations. Reservoir fluids were produced from four production wells at rates determined by the relative permeabilities, and hot water was injected into the center-well at a rate equal to the production rate. The advantage of this scheme is a combination of depressurization at the production well and thermal stimulation at the injection well. The effectiveness of the method

will strongly depend on the intrinsic permeability of the formation, relative permeabilities of fluids and thermal properties of the system.

Promising class 3 hydrate deposits should contain a high hydrate saturation, which in turn reduces the effective permeability of reservoir fluids and limits the reach of depressurization to a narrow zone in the vicinity of the low-pressure well. Depressurization may be an option only if the hydrate saturation is low (reducing their value as a production target) and the intrinsic permeability is high (Moridis and Collett, 2003). Thermal stimulation alone will lead to relatively slow, conduction-limited dissociation and is very energy intensive (Ruppel, 2011). Class 3 is also associated with high water production (Moridis and Collett, 2003). Despite these challenges, simulations have showed that gas can be produced at high rates over long times by constant pressure depressurization, i.e. maintenance of a constant pressure at the well (Moridis et al., 2009).

Class 4 is typical for many oceanic accumulations and involves dispersed, low-saturation hydrate (<10%) deposits. Based on numerical simulation, these deposits are not considered as promising targets for gas production. It cannot be identified any conditions leading to economically viable gas production from this hydrate class (Moridis and Sloan, 2007).

Injection of inhibitors may be used during some stages of production, for instance to dissociate reformed hydrate in the near-well area, but will not be the primary means of dissociating gas hydrate nor used for an extended period or on a large scale (Ruppel, 2011). Use of alcohols and glycols are expensive and necessitates separation of the produced gas. Injection of salt is less expensive but will lead to corrosion and deposition inside well casings and production equipment (Kvamme, 2014). All inhibitors will experience rapid reduction in effectiveness as the inhibitors are diluted by water released from dissociation (Moridis et al., 2009).

Production by CH_4-CO_2 exchange

Production of methane gas by CH_4-CO_2 exchange is based on the spontaneous conversion from methane hydrate to CO_2 hydrate when the original methane hydrate is contacted by CO_2. This conversion is a result of CO_2 hydrate being significantly more stable than natural gas hydrate (Kvamme et al., 2007), as seen from Figure 1.1.5. As the exchange takes place, the liberated methane molecules can be produced as methane gas without melting of the hydrate structure and associated water production. A conceptual drawing of the exchange process is given in Figure 1.2.5.
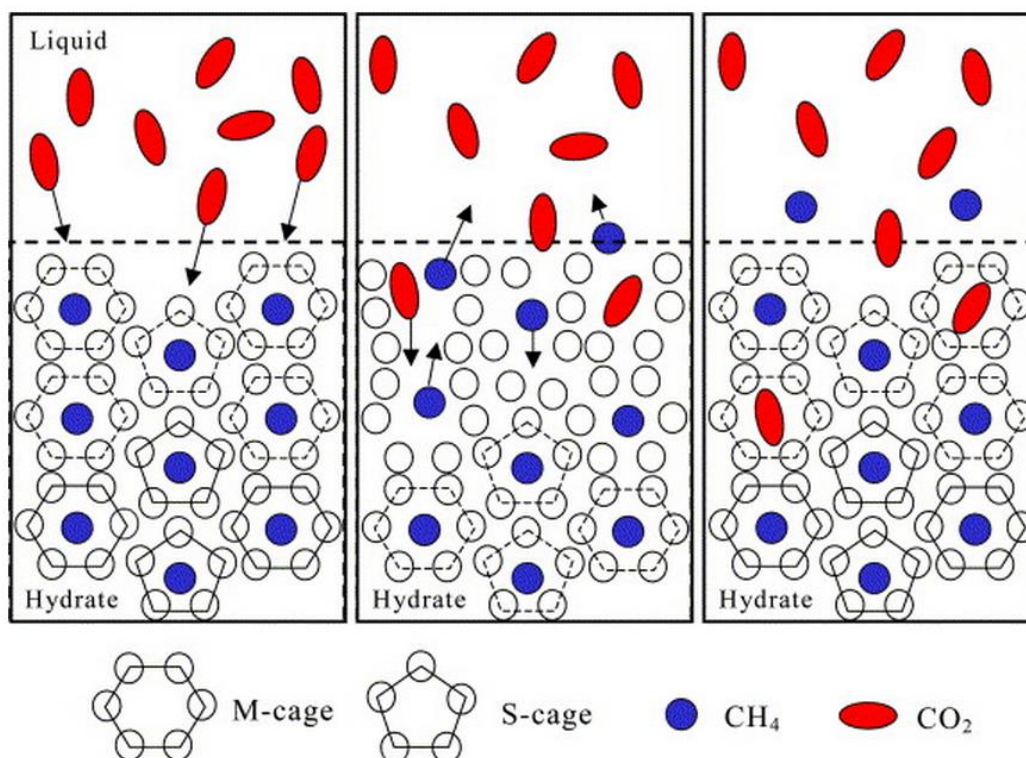
Figure 1.2.5: Conceptual drawing of guest molecule replacement and re-occupation (Ota *et al*., 2005).

The CO_2 molecules will replace methane molecules in the large cavities (M-cage) of structure I (Ota *et al*., 2005). The conversion process is rather slow as it is based on solid state diffusion, and keeping the concentration of liquid/gaseous CO_2 high will enhance the diffusion process (Kvamme, 2014). However, the exchange process can be accelerated by absorbed liquid-like structures on the mineral surfaces, which may act as transport channels for CO_2 and hence change the solid state diffusion to a faster liquid diffusion. These liquid channels can also act as escape routes for the released methane gas (Kvamme *et al*., 2007). The CO_2 can create hydrates with existing free water and the released heat of formation can dissociate methane hydrates. The exothermic heat of CO_2 hydrate formation is -57.9 kJ/mole, which is greater than the endothermic heat of methane dissociation of 54.5 kJ/mole. The combined process of melting and reformation is thus exothermic (McGrail *et al*., 2007). The impact of formation/dissociation compared to solid state conversion is not clearly understood, but experiments have shown that CH_4-CO_2 exchange takes place with no associated water production (Graue *et al*., 2008; Ersland *et al*., 2010).

Production of methane hydrates by CH_4-CO_2 exchange was initially considered as a slow process and hence unfeasible as a large scale production method. But the early experiments were based on bulk hydrate systems, and further research found that the process is accelerated in a porous media due to larger surface areas (Schoderbek *et al*., 2012). A series of laboratory experiments conducted by the Reservoir Physics group at the University of Bergen in collaboration with ConocoPhillips, resulted in a multi-year field trial in 2011. A test well was drilled in the Eileen Trend in the North Slope of Alaska, and the results of the CO_2 injection will be presented later.

1.2.6 Environmental aspects

Climate change

Gas hydrates are known to be a storehouse of organic carbon with potential linkages to global carbon cycling and global climate. Although gas hydrates are not considered to be a significant source for atmospheric greenhouse gases at present, there are clearly events in geologic history where significant releases of methane from gas hydrates have likely impacted global climates (Moridis *et al*., 2011). The mechanisms for destabilization of hydrates include ocean warming, changes in sea level, mass wasting on continental slopes and thawing of permafrost. But the mechanisms are not clearly understood, nor the rate of dissociation and the pathways from the underground to the atmosphere (Hester and Brewer, 2009). The effect of global warming is expected to affect oceanic and onshore hydrates different. A warmer climate will lead to melting of onshore glaciers, which in turn decreases the pressure gradient and permafrost hydrates can dissociate. At the same time, melting of glaciers will lead to an increase in sea water level resulting in increased pressure and increased stability for oceanic hydrate accumulations (Kvenvolden, 1993). One should keep in mind that the hydrate deposits that are most closely coupled to the atmosphere/ocean system are not targets of gas hydrate production research. Targets for hydrate production reside in sand reservoirs deep into the subsurface and represent only a small fraction of the total hydrate resources. Production from hydrates will induce rapid pressure and temperature perturbations unlike global climate changes that will lead to relatively small but long-term perturbations that propagates deep into the subsurface. It is thus important to do improved research on both short-term and long-term effects of hydrate production (Moridis *et al*., 2011).

Anthropogenic greenhouse gas emissions have increased since the pre-industrial era and are likely to have been the dominant cause of the observed warming since the mid-20th century (IPCC, 2014). The most abundant of these greenhouse gases is CO_2, and it is more or less global consensus on the need to reduce CO_2 emissions. Production of methane hydrate by CO_2 injection will benefit from energy production and at the same time store a potent greenhouse gas; the sequestered CO_2 hydrate will be more thermodynamically stable than the produced methane hydrate. Methane is the cleanest fossil fuel on combustion and produces half as much carbon dioxide and less than a third as much nitrogen oxides than coal-fired energy generation (Environmental Protection Agency US, 2013). Methane hydrate can be a good energy source until renewable energy can sustain the growing global demand. However, production must take place under safe and controllable circumstances, as release of methane to the atmosphere is much worse than CO_2. The overall greenhouse effect of methane is approximately 20 times bigger than CO_2, although the residence time of methane is limited in the atmosphere (Moridis *et al*., 2011).

Geomechanical stability

Production of hydrates is accompanied by changes in the bulk volume of the sediment, where depressurization yields the biggest volume change. This can lead to changes in sediment properties, loss of integrity for boreholes and possibly regional subsidence of the ground surface (Lee *et al*., 2010b). Deposits that are suitable for hydrate production often involve poorly consolidated sediments that are usually characterized by limited shear strength (Moridis *et al*., 2011). Regardless of growth habit, hydrate stiffens sediments in which it exists and dissociation can trigger submarine slides (Kleinberg *et al*., 2003). One of the largest submarine slides ever discovered, was the Storegga Slide outside Norway in the Norwegian Sea. The slide occurred 8200 years ago and generated a

tsunami that ran up 10-12 m of the west coast of Norway. Many processes contributed to an increase in pore pressure and a following decrease of the effective soil strength, and local destabilization of gas hydrates is one of them (Bryn *et al.*, 2005).

Laboratory experiments have shown that volume changes in low specific surface sediments, i.e. having a rigid sediment skeleton like sand, are much lower than those measured in high specific surface sediments, e.g. clay (Lee *et al.*, 2010b). All of the experiments in this thesis have been conducted with well-consolidated sandstone samples, and geomechanical stability has not been addressed.

In general, the magnitude of subsidence will be much larger in the case of oceanic hydrate-bearing sediments because of a larger magnitude of pressure decline than in the case of a permafrost-associated hydrate deposit. The subsidence is also reduced due to a relatively stiff permafrost overburden (Moridis *et al.*, 2011). Numerical simulations conducted on oceanic hydrates resulted in subsidence in the order of several meters. In addition, the stability of hydrate-bearing sediments in the vicinity of warm pipes may be strongly affected, especially near the ocean floor where the sediments are unconsolidated and more compressible. This can result in a collapse of the formation around the wellbore (Rutqvist and Moridis, 2007). Numerical studies based on depressurization-induced gas production from the Mallik and Mount Elbert permafrost deposits, indicate subsidence of only a few cm. Moreover, the vertical compaction is expected to be relatively uniform, leading to uniform settlements of the ground surface. The potential shear failure within the reservoir might be a more serious issue, as the fracturing can lead to a reduction in permeability and sand production (Rutqvist *et al.*, 2009).

1.2.7 Field projects

The last decades of natural gas hydrate research and the growing global energy demand, has contributed to an effort to map and characterize the potential of production from hydrate accumulations. Countries like the United States, Japan, China, South Korea and India, all have national gas hydrate research programs, and are the leading players in the development of future hydrate production (Collett, 2008). But other countries are also making an effort, and this chapter will summarize two field projects conducted in Canada and the U.S., besides the accidental discovery of gas hydrates in a Russian gas field. In addition, the first field trial of gas production from marine hydrate deposits was conducted in March 2013 in the Eastern Nankai Trough off the coast of Japan. The data obtained during the test is still under investigation, but the preliminary results show that hydrate production by depressurization is possible even in marine sediments (Yamamoto *et al.*, 2014).

Messoyakha

The Messoyakha Gas Field was discovered in 1967 in the permafrost of eastern Siberia. The field is enclosed in an anticlinal structural trap and was put to production in 1970. As the production commenced and through the shutdown in 1979-82, it became clear that the field did not only consist of free gas. An increase in average reservoir pressure during shut-in, no change in gas-water contact during production and perforation blocking, led to the assumption of an overlying hydrate layer (Grover *et al.*, 2008). The upper part of the reservoir is within hydrate stability conditions and the lower part is outside the stable boundary. It is believed that hydrate dissociation replenishes the

produced free gas and explains the anomalously pressure curves, as seen in Figure 1.2.7a (Grover *et al.*, 2008).
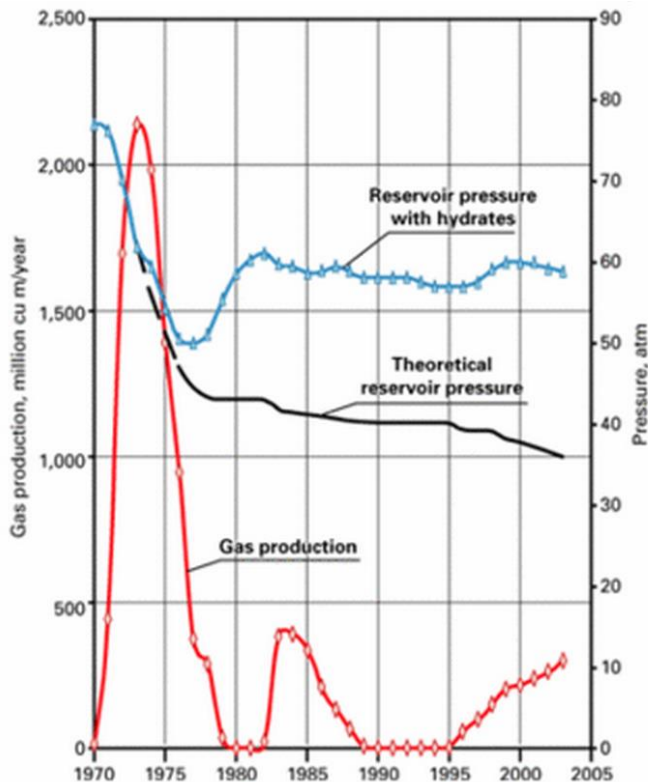
Figure 1.2.7a: Gas production and reservoir pressure in Messoyakha (Makogon *et al.*, 2005).

The observed reservoir pressure, blue line in Figure 1.2.7a, is higher than the theoretical reservoir pressure, which is based on the initial assumption of only free gas. Makogon *et al.* (2005) reports of initial free gas reserves in the amount of 848 Bcf, and have estimated the producible reserves of gas in hydrated state to be 424 Bcf. The Messoyakha field is an example of a class 1 reservoir and has inspired for further research on production from onshore arctic gas hydrate reservoirs.

Mallik

The Mallik Field, located in the Mackenzie Delta in the Northwest Territories of Canada, has been subjected to a total of three gas hydrate production research programs. The first well was drilled in 1998 to test equipment developed by Japan National Oil Corporation and to prepare for test drilling in the Nankai Trough. The drilling revealed several forms of hydrate in a variety of sands and gravels, with a total thickness of the gas hydrate layer of approximately 150 m (Collett, 2008).

The promising results of the first test well were followed by three new wells in the period from December 2001 to March 2002. One of these wells was the first modern, fully integrated production test from a natural gas hydrate accumulation. The primary aim for this second research program was to evaluate the effect of depressurization and thermal stimulation, and to provide input for numerical simulation of long-term production. It was proven that production from natural gas hydrates is technically feasible, and the permeability of the hydrate-bearing layers was bigger than expected. It also showed that depressurization is the most favorable production method compared

28

to heating alone, with a combination of the two methods yielding the largest amount of gas (Collett, 2008).

The last research program was initiated in the winter 2007 and started with a modification of the existing well from 1998. This time, the research program was hoping to develop new insight by undertaking a simple long-term depressurization. First, a 60 hours production test was conducted which showed the necessity of sand screening to avoid sand production (Yamamoto and Dallimore, 2008).
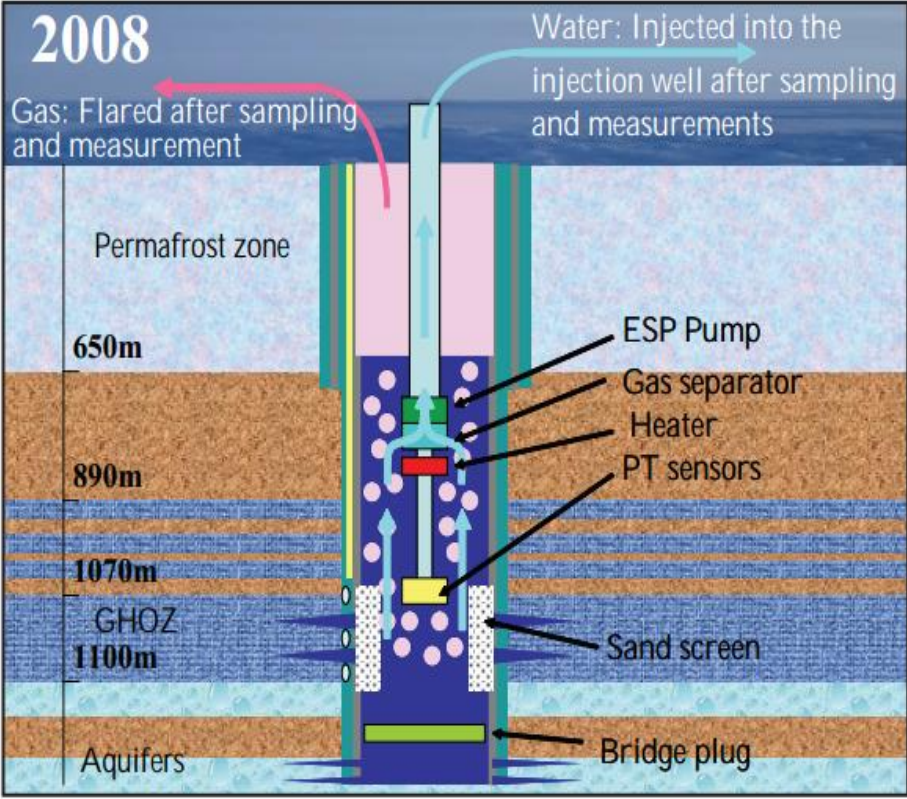
Figure 1.2.7b: Schematic of depressurization system used in 2008 during long-term production test (Yamamoto and Dallimore, 2008).

After the technical problems had been addressed, the main production started on March 10 and lasted for a preset time of 139 hours. The pump generated stable pressure conditions throughout the test and continues gas flow ranging from 2000-4000 m^3/day was maintained. The test was considered a success and showed the feasibility of depressurization as a production method (Yamamoto and Dallimore, 2008).

Iğnik Sikumi

The Iğnik Sikumi #1 was drilled on April 16, 2011 in the Eileen Trend on the North Slope of Alaska. The area was known to contain four hydrate-bearing sandstones, and the layer targeted for injection had a homogenous, thick-bedded character. NMR logging indicated a hydrate saturation of 75% and the remaining pore volume was filled with water. The high water content raised the concern of additional hydrate formation when injecting CO_2, especially in the near well-bore area. The weight of a liquid CO_2 column would also exceed the fracture pressure of the sandstone formation. It was therefore decided to dilute the liquid CO_2 with nitrogen to obtain a single phase gas. The optimal

ratio between nitrogen and CO_2 was calculated from simulations to balance the exchange process against nitrogen-induced dissociation. This led to injection of a gas with composition of 23% CO_2 + 77% N_2 (mole percent). A total volume of approximately 210 Mscf of gas was injected during a time period of thirteen days (Schoderbek *et al.*, 2012).

The field trial was conducted with four different stages of production. The first stage consisted of 34 hours with unassisted flow-back driven by the reservoir pressure. The next three stages consisted of jet pumping above methane hydrate stability pressure, jet pumping near methane hydrate stability pressure, and jet pumping below methane hydrate stability pressure. These stages lasted seven days, to and a half days and 19 days, respectively. The total produced volume of gas reached approximately 998 Mscf, with methane accounting for 821 Mscf of this volume (Schoderbek *et al.*, 2012). The recovery of the injectant is shown in Figure 1.2.7c.
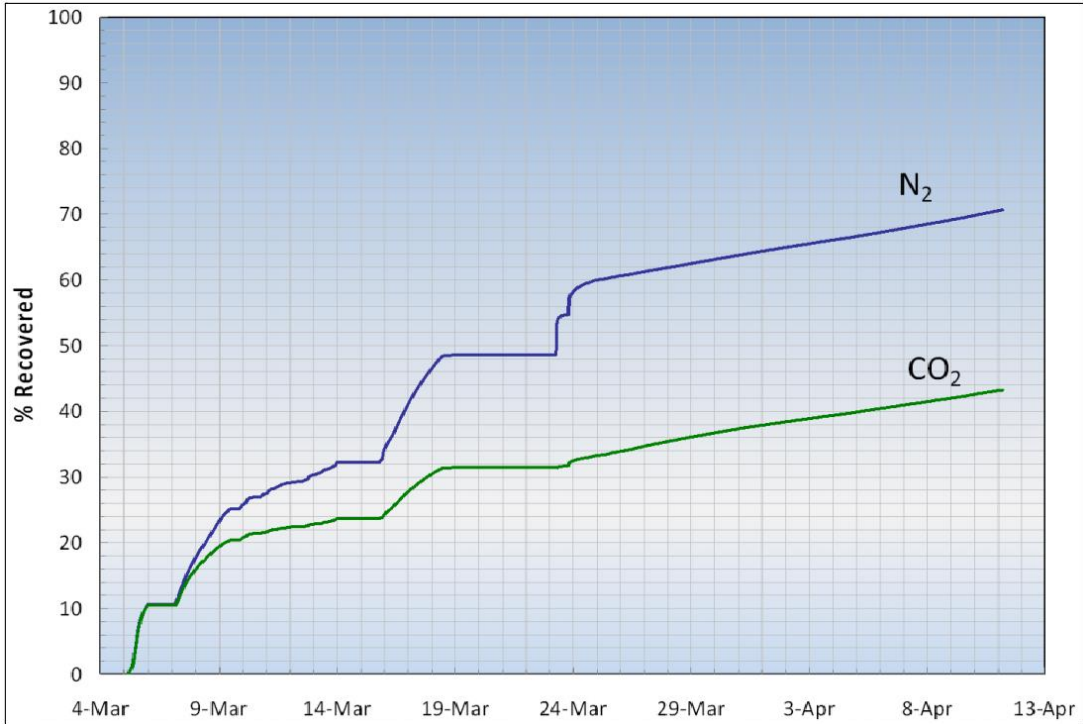
Figure 1.2.7c: Recovery of injectant as a function of time (Schoderbek *et al.*, 2012).

The horizontal parts of the recovery functions in Figure 1.2.7c denote the shut-in periods between different production stages. Approximately 70% of the nitrogen was recovered and more than half of the CO_2 was sequestered in the formation. This shows the potential of CO_2 storage in permafrost hydrate accumulations, in addition to beneficial production of methane gas. The mixture of CO_2 and nitrogen proved to be an effective way of maintaining injectivity during injection, and the field trial demonstrated that the exchange technology may be commercially viable in the future (Schoderbek *et al.*, 2012).

1.3 Measurement techniques for hydrate formation and dissociation

1.3.1 MRI imaging

MRI (Magnetic Resonance Imaging, also called Nuclear Magnetic Resonance) is a widely used imaging technique, especially within medical science but also within petroleum technology. The technique is based on interactions between magnetic dipole moments of charged particles when placed in a static magnetic field. The particles will precess around the magnetic field direction with a given frequency, yielding a net magnetization in that direction. By applying an additional dynamic magnetic field, rotating with the same frequency as the particles, one can tilt a predetermined proportion of the magnetic dipoles in the opposite direction. The potential energy will then increase and the dipoles will individually switch back whilst emitting energy. If all of the magnetic dipoles are tilted, the net magnetization is reversed, and the relaxation time T_1 (spin-lattice) will indicate the time needed to restore orientation. If half of the magnetic dipoles are tilted, the opposite magnetizations will cancel each other and result in zero magnetization in that direction. However, the dipole moments will initially rotate in phase and thereby create a rotating net magnetization perpendicular to the static field. The relaxation time T_2 (spin-spin) will indicate the time needed to terminate this phase coherence. The two relaxation times can be estimated by generating different pulse sequences with the high frequency field, and then measure the received energy as the dipole moments fall back to their original orientation. These relaxation times can be used to calculate porosity, pore size distribution, permeability and saturation (Lien, 2004).

In the context of hydrate experiments, MRI can be used to survey both formation and dissociation of hydrates. Hydrogen isotopes ($_1^1H$ and $_1^3H$) have a high resonance frequency and provide strong signal quality (Lien, 2004). This makes it possible to image hydrogen atoms in water and methane. In the hydrate structure, hydrogen atoms experience short relaxation times and are not detected. Hydrate formation is measured as a drop in signal intensity when water and methane combine to give hydrates. The signal will reappear when hydrates dissociate and one can create 3D images showing local distribution of hydrates.

1.3.2 Resistivity measurements

The electrical resistivity R [Ωm] is a measure of the specific resistance of a material and is given by:

$$R = r\frac{A}{L} \qquad (1.3.2a)$$

where r is the total resistance [Ω], A is the cross-sectional area [m²] and L is the length [m] of the medium. The expression is only valid for a DC (direct current) circuit, and resistance r is exchanged by impedance Z when dealing with AC (alternating current) circuits. This impedance is actually a complex value and the absolute value $|Z|$ is defined by its real part (resistance) and a phase angle ϑ. The expression for the resistivity becomes:

$$R = |Z|\frac{A}{L}\cos(\theta) \qquad (1.3.2b)$$

The cosine term disappears when the phase angle ϑ is zero (DC circuit), and the absolute value of the impedance resolves to the resistance r.

The correlation between resistivity values and important reservoir parameters such as porosity and saturation was investigated by Archie (1942). He found an empirical relation between the formation factor F and the porosity, later known as *Archies 1. law*:

$$F := \frac{R_o}{R_w} = a\varphi^{-m} \qquad (1.3.2c)$$

where R_o is the resistivity of completely brine saturated formation, R_w is the resistivity of the brine itself, a is a proportionality constant dependent on tortuosity and pore size distribution, ϕ is the porosity [frac.] and m is the cementation constant. The cementation exponent will depend on the ratio between pore size and pore throat size and the number of closed channels (Lien, 2004). Archie (1942) also found an empirical relation between the resistivity index I and the water saturation, later known as *Archies 2. law*:

$$I := \frac{R_t}{R_o} = bS_w^{-n} \qquad (1.3.2d)$$

where R_t is the actual resistivity of formation filled with water and hydrocarbons, b is a proportionality constant dependent on tortuosity, S_w is the brine saturation [frac.] and n is the saturation constant. The saturation exponent will depend on wettability and is expected to be approximately 2 for a uniformly water-wet core sample (Birkedal *et al.*, 2011).

Resistivity measurements can be a good tool to aid interpretation of hydrate saturation during hydrate formation and dissociation. Natural gas hydrates are electrical nonconductive and the core resistivity will increase as the hydrate blocks off pore channels. The transport of electrical current will experience more difficulties as the brine becomes more constrained during hydrate formation. At the same time, the salinity will increase and enhance the electrical conductivity since salt is expelled from water entering hydrate cavities. The overall effect on resistivity will be a settlement between hydrate saturation and salt content, and on local heterogeneities in fluid saturation.

1.4 Calculations

1.4.1 Hydrate formation/dissociation

The hydrate formation calculations conducted in this thesis are based on consumption of methane gas as hydrates form under constant temperature and pressure. The hydrate volume is then given by:

$$V_H = \left(\frac{\left(\frac{V_{CH4} * \rho_{CH4}^{pump}}{Mm_{CH4}} \right) * n_w * Mm_w}{\rho_w^{core}} \right) * 1.26 \qquad (1.4.1a)$$

where V_{CH4} is the measured pump volume [mL], n_w is the hydration number, ρ is density [g/mL] and Mm is molar mass [g/mole]. The last factor, 1.26, is the expansion of water as water molecules converts from liquid to hydrate form (Lee *et al.*, 2010b). This expansion will displace methane gas and the measured pump volume will be an underestimation of the amount of gas that has entered the hydrate. To account for this expansion, one has to iterate Eq. 1.4.1b until the volume of expansion, V_{exp}, converges to zero (approximately five steps).

$$V_H^1 = V_H^0 + \left(\frac{\left(\frac{V_{exp}^0 * \rho_{CH4}^{core}}{Mm_{CH4}} \right) * n_w * Mm_w}{\rho_w^{core}} \right) * 1.26 \qquad (1.4.1b)$$

The same iteration process is necessary to account for contraction during hydrate dissociation. Density values of methane (and CO_2) for different temperatures and pressures are obtained from Wischnewski (n.d.).

The final volume of water after hydrate formation is calculated from the initial water saturation and the amount of water entering the hydrate, but the salinity will increase since salt does not enter the hydrate cavities. This salinity [wt%] increase is given by:

$$Salinity_{after} = \frac{V_w^{ini} * \rho_w^{ini} * salinity_{ini}}{(V_w^{ini} * \rho_w^{ini}) - (n_w^H * Mm_w)} \qquad (1.4.1c)$$

where n_w^H is the amount of water entering the hydrate [mole] and the super/subscript *ini* denotes initial conditions, i.e. prior to hydrate formation. This equation is used to compute brine salinities corresponding to different water saturations during hydrate formation. The salinity values are used as input to calculate R_o from the following empirical relation (Birkedal *et al.*, 2011):

$$R_o = 16.176 * (C)^{-1.04} \qquad (1.4.1d)$$

where C is the salt concentration [wt%]. This equation is based on Bentheim sandstone cores similar to the ones used in this thesis, and yields a dynamic resistivity index that accounts for varying brine

conductivity. R_t is found by using Eq. 1.3.2b and neglecting the phase angle ϑ (Birkedal *et al*., 2011)*,* and is implemented in conjunction with R_o in *Archies 2. law.* The proportionality constant *b* is defaulted to unity and a value of 2.17 is used for the saturation exponent (Pearson *et al*., 1983). Finally, the water saturations can be calculated and compared with saturations obtained from PVT data.

1.4.2 CSMGem

CSMGem is a hydrate equilibrium program developed by Colorado School of Mines. It can predict stable hydrate structures and cage occupancies at given pressures, temperatures and compositions (Colorado School of Mines, 2009). This program has been used to aid the interpretation of results from depressurization and needs some comments on its viability.

The program is tailored to the hydrocarbon industry and is based on equilibrium calculations on bulk hydrate systems. In a porous media however, true equilibrium cannot be obtained. This can be shown by a short study of *Gibbs phase rule*:

$$\tau = n - \pi + 2 \qquad\qquad (1.4.2)$$

where *n* is the number of components, π is the number of phases and τ is the number of variables that must be defined in order to reach equilibrium. The components which actively distribute between phases are only water and methane, but the different phases can be numerous. There is a water phase, a gas phase and a hydrate phase, with additional absorbed phases on both hydrate and mineral surfaces. When local temperature and pressure are set, the system becomes over-determined and equilibrium cannot be reached. The hydrate in a porous media will thus be in a semi-stable state with possibly many different hydrate compositions (Kvamme, 2014), compared to the scenario described by the program with equilibrium between phases and no impact of solid surfaces.

2 Literature Survey

2.1 CH$_4$-CO$_2$ exchange

The first dedicated research on the topic of CH$_4$-CO$_2$ exchange was conducted by Ohgaki *et al.* (1994; 1996). They showed the up-concentration of CO$_2$ in the hydrate phase compared with the gas phase for a methane and CO$_2$ hydrate bulk system. Seo *et al.* (2001) advanced the concept and created hydrates from liquid water and a mixture of methane and CO$_2$ gas. They found that 40 mole% CO$_2$ in the gas phase yielded hydrates with 90 mole% CO$_2$ (at 35 bar and 0.5 K below three-phase equilibrium). This clearly showed the hydrates affinity towards CO$_2$ compared with methane. Further research conducted by Uchida *et al.* (2001) investigated the effect of introducing CO$_2$ to already existing methane hydrate. Microscopic Raman measurements showed that more than 80% of the methane molecules at the interface were replaced by CO$_2$ molecules (at -2.2 °C and 29 bar), and that CO$_2$ mainly occupied the large cavities. But kinetics was slow and the induction period was estimated to 50 hours. The slow kinetics was underpinned by the results of McGrail *et al.* (2004), who measured the penetration rate of CO$_2$ into bulk methane hydrate. By the use of scanning laser Raman spectrometry they found the penetration rate to be 1.3 mm/hr at 4.5 °C and 34.5 bar. Lee *et al.* (2003) stated, inferred from experimental results along with some assumptions, that the recoverable amount of methane could reach 64%.

Experimental research on bulk methane hydrates contacted by CO$_2$ molecules has revealed some distinct features of the exchange process. One of them is increased replacement rate and reaction time when using liquid CO$_2$ instead of gaseous CO$_2$. The exchange rate will also increase with temperature at constant pressure. The experiments show that the ratio between released methane and consumed CO$_2$ is nearly unity, and this indicates the dominance of the exchange reaction with CO$_2$ molecules occupying previously methane filled cavities. This exchange mainly proceeds in the large cavities. Finally, the research concludes with overall slow reaction rates. After a rapid initial (about 10 hours) reaction rate at the interface between hydrate and gas/liquid, the rate drops as the CO$_2$ must diffuse progressively deeper into the bulk hydrate (Zhao *et al.*, 2012).

In order to investigate the exchange process in a porous media, a series of core experiments were conducted utilizing MRI as imaging technique (Kvamme *et al.*, 2007; Graue *et al.*, 2008; Baldwin *et al.*, 2009; Ersland *et al.*, 2010). Hydrate was created inside Bentheim sandstone cores from methane gas and water with salinities ranging from 0.1 to 5.0 wt%. After completion of hydrate formation, the cores were flooded with liquid CO$_2$ (at 83.75 bar and 4 °C) and the subsequent exchange process was monitored by MRI. All of the cores exposed to CO$_2$ were modified and contained a small longitudinal spacer dividing the core in two symmetrical halves. This spacer served to increase the surface area between CO$_2$ and methane hydrate, and to create an open volume for collection and detection of produced methane gas. The spacer also hindered possible formation of CO$_2$ hydrate with excess water and prevented clogging of the core. The initial (ca. 100 hours) exchange rate was fast but terminated after a while, and some of the cores were reflooded with CO$_2$. The fresh CO$_2$ displaced produced methane from the spacer and thereby further increased the diffusion driven exchange process. Graue *et al.* (2008) reported a recovery of 50-85% of the gas originally in the hydrate after conducting three CO$_2$ flushes. None of the experiments detected any measurable hydrate dissociation (within the resolution of MRI) and no heat was added to the system. Simulations based on Phase Field Theory were used to reesemble the experimental production rates, and a best fit was

found with a diffusivity coeffisient of CO_2 equal to $1.7*10^{-9}$ m^2/s. This value is approximately the same as the diffusivity coeffisient of CO_2 in seawater and indicates the beneficial effect of surface absorbed liquid layers. In contradiction to this, Yang *et al.* (2008) have reported a decrease in reaction rate with increasing excess water. These experiments were conducted with methane hydrate and liquid CO_2 in a glass bead pack (at 84 bar and 10.8 °C). They suggested that the excess water offers a shielding effect between methane hydrate and CO_2 molecules which reduces the rate of mass transfer.

Park *et al.* (2008) investigated the effect of introducing methane hydrate to a binary N_2 + CO_2 gas (20 mole% of CO_2 and 80 mole% of N_2). They used NMR and FT-Raman spectrometry to quantify the recovery rate on methane hydrate in bulk (pressure and temperature not specified). Their experimental results showed a promising outcome of 85% methane recovery and was explained by additional recovery due to nitrogen attacking the small cavities of sI hydrate. Kang *et al.* (2012) obtained the same recovery rate on both a recovered hydrate sample in clay and a manufactured intercalated methane hydrate sample, but the exchange rate was slower than in the bulk hydrate case.

2.2 Depressurization

The work on depressurization of natural gas hydrates is numerous and has evolved from the beginning of the eighties. Much of the initial research was based on equilibria measurements of bulk hydrate systems. Later, when focus was shifted towards gas recovery from porous media, many production schemes based on depressurization were developed. All of these models pinpoint the important effect of heat conductivity and reservoir permeability, but do also indicate depressurization as the most favorable production method (Sloan, 1998). Gas production behavior during depressurization is known to depend on hydrate saturation, hydrate uniformity, difference between dissociation pressure and equilibrium pressure, and core sample size (will impact the heat conductivity during core experiments) (Haligva *et al.*, 2010).

Yousif *et al.* (1990) used Berea sandstone cores and examined the effect of depressurization from one end of the core. The experimental setup was similar to the one used in this thesis and depressurization was conducted with a temperature maintained at 0.6 °C and a constant pressure below equilibrium pressure. They found that the inlet pressure remained constant for a couple of hours after reducing the outlet pressure, indicating a hydrate dissociation front moving from the outlet. The missing immediate response of the inlet pressure highlights the low permeability of hydrate-filled sediments. This effect was also observed by Lee *et al.* (2010a), where the inlet of a Berea sandstone core (high intrinsic permeability) was insensitive to outlet pressure change. A similar experiment was conducted using Bentheim sandstone cores (Ersland *et al.*, 2009). The pressure was lowered in increments of 0.7 bars (constant temperature of 4 °C) from both ends, and received volume of gas was measured at each pressure step. The start of dissociation was determined to be below the equilibrium value, and they suggested that this could be explained by high hydrate saturation and very low permeability. In contradiction to this, Uchida *et al.* (2004) found porous media with small pores to have an inhibiting effect on hydrate growth. The maximum pore sizes that influenced hydrate equilibria were about 50 µm for Berea sand.

Based on own experimental results, Xiong *et al.* (2012) divided the depressurization induced dissociation process into three phases. Phase one consists of free gas release due to pressure

reduction. Phase two is dominated by rapid hydrate dissociation, accompanied by a sharp temperature decrease before heat transferred from the surroundings gradually increases the temperature. The final phase gives rise to small changes in temperature and the gas production slows down until complete dissociation.

3 Materials and Methods

3.1 Hydrate formation, CH$_4$-CO$_2$ exchange and depressurization

3.1.1 Experimental design

Most of the hydrate formation, CH$_4$-CO$_2$ exchange and depressurization experiments were conducted in the hydrate laboratory at the Department of Physics and Technology at the University of Bergen. The laboratory is equipped with three more or less equal setups (A, B and C), displayed in Figure 3.1.1a. The only difference in experimental design is that Setup A contains a different core holder which allows for resistance measurements. These three setups are a result of many years with design and improvements by earlier PhD and master students, and the setups have been further modified during the work conducted in this thesis. All experimental work has been conducted in collaboration with fellow master student Erik Vadla.
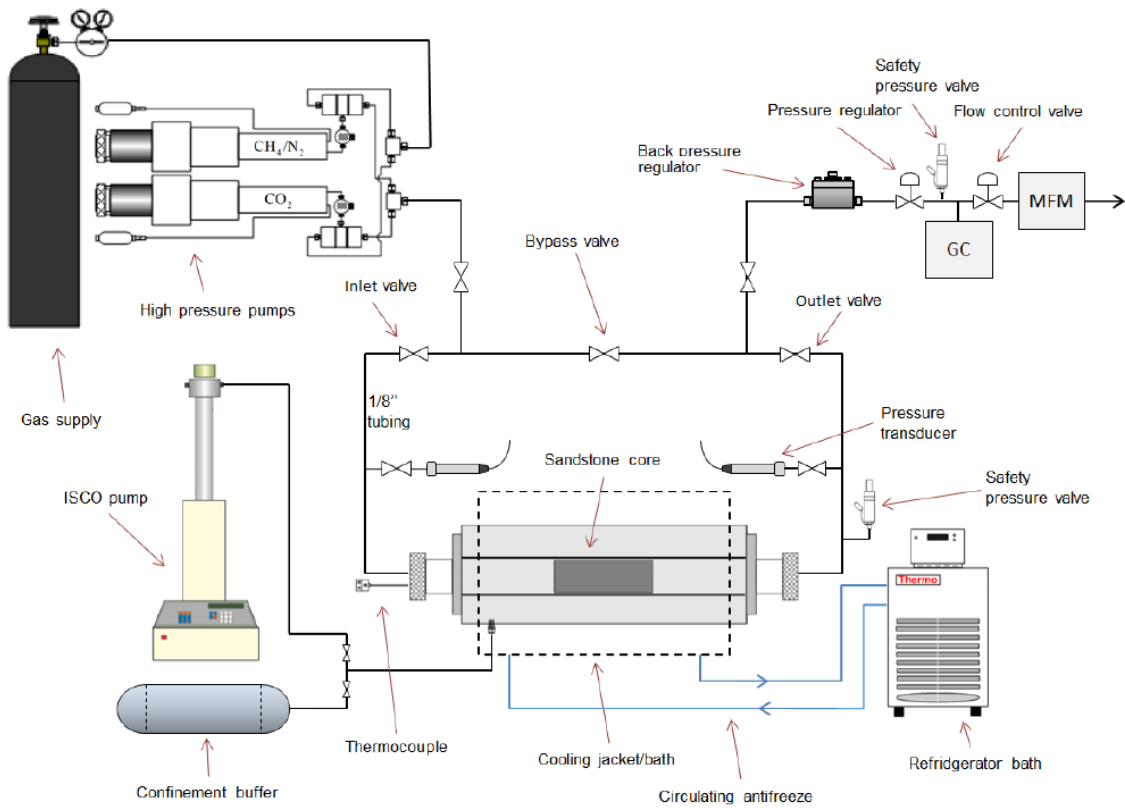

Figure 3.1.1a: General experimental design. Modified from Hågenvik (2013).

One Stigma 500 and two Stigma 1000 high pressure pumps were used to inject and reject fluids. Three pumps allowed for simultaneous hydrate formation in all three setups, but exchange experiments required two pumps connected to the same setup, as shown in Figure 3.1.1.a. The pumps were connected with the end-pieces at inlet and outlet of the core holder through 1/8" steel tubing provided by Swagelok. The core could be pressurized from both sides by having the bypass valve open. Valves at the inlet and outlet lines allowed for bypassing of fluids directly to production

equipment while keeping the core isolated. Pressure transducers were connected to inlet and outlet lines with separate valves. This made it possible to connect and disconnect the pressure transducers during ongoing experiments, and to monitor the pressure during disconnection between pump and core. A safety pressure valve was always connected at either inlet or outlet tubing.
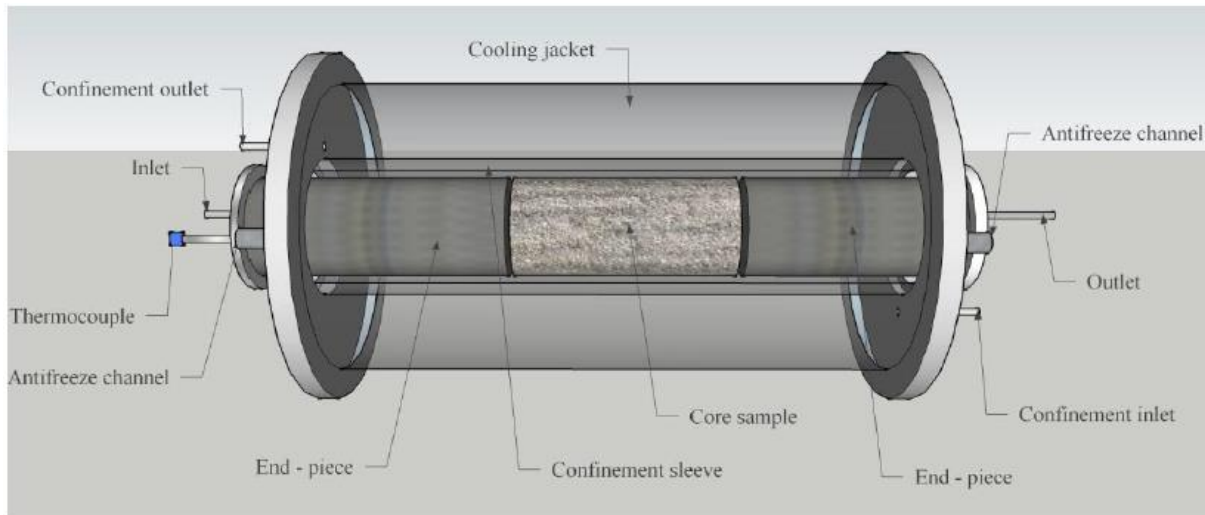
Figure 3.1.1b: Core holder used in setup B and C (Hossainpour, 2013).

The core holders used in setup B and C were Hassler core holders and had a fixed sleeve mounted inside, as shown in Figure 3.1.1b. The core holder in setup A was slightly different and is depicted later. End-pieces held the core in place and distributed the fluids at the core ends. The confinement oil was pressurized by an Isco D-series pump and was always held at a pressure at least 30 bar above pore pressure. The Isco pump was sometimes used to maintain constant pressure during experiments, but with only one pump and three setups it was also used confinement buffers. These buffers were made of a cylinder filled with confinement oil and nitrogen gas segregated by a piston. The end of the cylinder filled with oil was pressurized to a given pressure by the Isco pump, and the buffer was connected to the confinement system. The nitrogen gas in the buffer contributed to adjust for pressure changes in confinement oil during temperature fluctuations. One Isco pump and two confinement buffers were sufficient to operate all three setups, and confinement pressure was maintained within a few bars from set point. The core holders were coated by cooling jackets connected to a refrigerator bath. The cooling baths used were Grants instruments LTC 6-30 and Thermo Neslab RTE-17. With only two refrigerator baths available, the most powerful one of them (Grant) had to serve both setup A and B. A mixture of water and antifreeze was circulated to maintain the desired core temperature, which was measured by Omega HH506RA thermometers mounted at inlet or outlet surface of the core. The temperature readings were a measure of core surface temperature and showed fluctuations of ±0.3 °C during experiments.

The outlet lines were connected to a backpressure regulator (BPR) giving constant production pressure during CH_4-CO_2 exchange experiments. The produced fluid was then led through a pressure regulator to reduce the pressure to the operating condition of an Agilent 3000 Micro gas chromatograph (GC). To ensure that the GC experienced an acceptable pressure value, a safety pressure valve was also connected in front of the GC. A flow control valve was situated downstream of the GC to obtain steady flowrate to a CORI-FLOW mass flow meter (MFM). Finally, the produced gas was safely vented.

3.1.2 Floating end-piece in setup A

Setup A was equipped with a different core holder than in the two other setups. The sleeve was not fixed inside the core holder, see Figure 3.1.2. Instead, the core was placed inside the sleeve with the adjustable end-piece in one end, and pushed inside the core holder and connected to the other end-piece. When the confinement oil was introduced and with the corresponding increase in confinement pressure, the adjustable end-piece was pushed tight against the core end. This floating sleeve configuration permitted electrical resistance measurements by connecting wirelines on inlet and outlet tubing. The wirelines were connected to a Hewlett Packard LCR-meter for recording, and the resistivity was calculated from the resistance. Previous experiments have demonstrated that a computer will impact the signals when connected to the LCR-meter for logging, so a remote camera was used to monitor resistance readings.
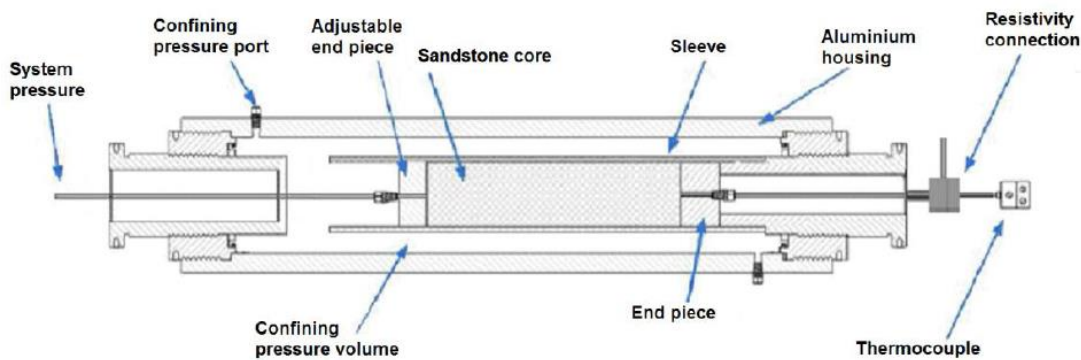

**Figure 3.1.2: Cross section of core holder used in setup A. Modified from Birkedal *et al*. (2011).**

3.1.3 Implemented modifications

Keeping the GC operational has been a persistent problem the last couple of years in the hydrate laboratory. The GC is set to monitor produced gas concentrations and is not compatible with liquid water. Although gas is mainly produced during CH_4-CO_2 exchange experiments, it will sometimes unintentionally be produced liquid water. This leads to errors in the GC and subsequent time-consuming maintenance. The GC is provided with a build-in particle filter but this is not enough to elude liquid water. During the work of this thesis, it was investigated on how to stop water from entering the GC, and a suitable moisture trap was ordered, tested and implemented in the preexisting production setup (Figure 3.1.3a).
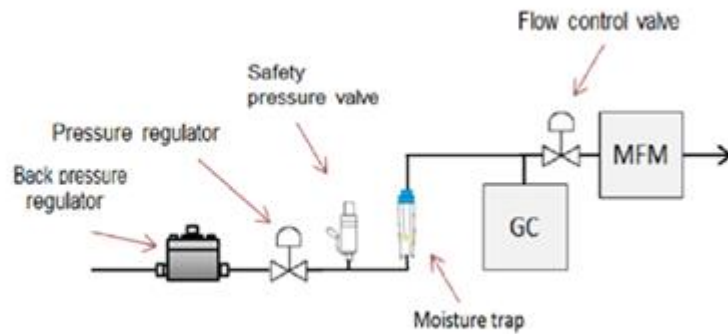
Figure 3.1.3a: Moisture trap to the left. Schematic of moisture trap placement to the right.

Another small but significant modification was done to enhance the information collected from CH_4-CO_2 exchange experiments. A common problem when injecting CO_2 or N_2/CO_2 into a hydrate-filled core with excess water is reformation of hydrates and possible clogging. With the preexisting setup, it was not possible to deduce whether it was the core itself being clogged, i.e. having approximately zero permeability, or just the end-pieces. This problem was solved by adding a new flow loop from inlet end-piece to outlet tubing, see Figure 3.1.3b. It was then feasible to do a flow test through the inlet end-piece and infer if the end-piece itself was clogged.
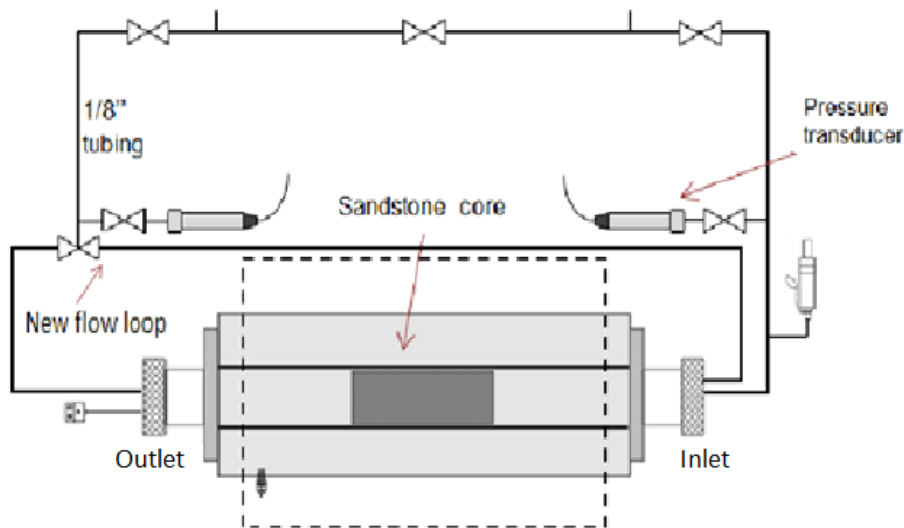
Figure 3.1.3b: Schematic of new flow loop in setup B.

3.1.4 Core preparations

The cores used in the experiments were outcrop Bentheim sandstone cores from a quarry in Germany. Graue *et al*. (2008) have used equivalent Bentheim cores and have reported porosities and permeabilities of 22% and 1.1 Darcy, respectively. The cores in these experiments are assumed to hold the same properties with a measured grain density of 2.65 g/cm³. The average pore diameter is 125 microns and the pore geometry is fairly uniform. The mineralogy was first assumed to be 99%

quartz with small amounts of kaolinite (Graue *et al*., 2008), but recent research has moderated the amount of quartz to around 95% (Ramstad *et al*., 2012). It was found trace amounts of K-feldspar, chlorite, kaolinite, carbonates and pyrite.

All of the cores were cut to approximately 15 cm and had a diameter of about 5 cm. After cutting, the cores were placed in a heating cabinet (60°C) for 24 hours. This was done to ensure no moisture or other contaminants prior to saturation. When the cores had cooled off, they were weighted and the diameter and length were measured. Three diameter measurements were taken along the length of the core and the average value was used. The same was done for the length; three measurements from different directions. To saturate the cores, it was used a 3.50 wt% brine solution made by mixing appropriate amounts of sodium chloride and distilled water. The cores were laid horizontally in a small plastic box and some of the brine was added, just enough to wet the lower parts of the cores. In the following minutes the water imbibed spontaneous upwards through the cores and the air was allowed to leave at the top. When the spontaneous imbibition was finished, the cores were completely submerged in brine and left for 24 hours. This procedure gave fairly consistent saturations ranging from 0.57 to 0.70, and saturations were calculated by weighing the saturated cores and thereby determine the mass of imbibed water. Some of the saturated cores were directly mounted in a core holder, while cores intended for CH_4-CO_2 exchange experiments were wrapped in aluminium foil. The aluminium foil protected the core holder sleeves from degradation by invading CO_2 molecules during experiments.

Figure 3.1.4: Bentheim sandstone core (upper left). Heating cabinet (upper right). Two cores during saturation (lower left). Core wrapped in aluminium foil (lower right).

3.1.5 Hydrate formation procedure

When the core had been placed in a core holder, the end-pieces were pushed inside and tightened. The confinement pressure was set to 30 bar. One Stigma pump with connected tubings leading to the setup was vacuumed. The inlet and outlet valves were closed (bypass valve open) and it was not possible to vacuum all the way to the end-pieces as this would reject water from the core. The pressure transducer valves were closed and the pressure transducers were not operated during hydrate formation. The Stigma pump (connected to the setup) was slowly filled with methane gas (>99.5%) and at one bar the inlet and outlet valves were opened. Pump and core were pressurized to 83 bar and confinement pressure was always kept 30 bar above pore pressure. The confinement oil was pressurized to 110 bar with the Isco pump and then connected to a confinement buffer. The Stigma pump was set to constant pressure 83 bar and the system was routinely checked for leaks. After approximately 24 hours one could estimate if the leakage rate was at a satisfactory level (<0.05 mL/h) and hydrate formation was initiated by turning on the refrigerator bath. The core surface temperature was monitored and logged, and the cooling bath temperature was tuned accordingly. Beside of core temperature readings, the pump volume was logged and used for calculations. Some of the experiments were conducted with resistivity measurements as described in Chapter 3.1.2. The hydrate formation was terminated when the pump volume reached a constant value, approximately after 200-300 h.

3.1.6 Procedure for CH_4-CO_2 exchange

When hydrate formation had proceeded, the pressure transducers were calibrated and pressure transducer valves were opened. Inlet and outlet valves were closed and the Stigma pump was emptied for methane gas and refilled with nitrogen gas (>99.6%). Nitrogen gas was injected to the production lines via the bypass valve and ensured a pressure of 83 bar at the BPR. Another Stigma pump was filled with CO_2 gas (99.999%) and pressurized to liquid CO_2 at 83 bar. The pumps were connected together and were set to inject a predetermined mixture of 40% CO_2 and 60% nitrogen [mole percent]. Inlet and outlet valves were now open but the bypass valve was closed, so the mixture was only introduced at the core inlet. The injection was set to constant rate and the pressure increased at the inlet, through the core and up to the BPR. At around 85 bar, which was the set pressure of the BPR, the fluids were allowed to be produced through the production equipment. The GC and MFM readings were logged with a computer, along with pressure transducers, core surface temperature and pump flow rate. Production was only carried out during the day when the equipment could be supervised regularly. The pumps were stopped and no flow went through the BPR during nighttime. Production continued until the produced fluids contained trace amounts of methane gas.

3.1.7 Depressurization procedure

The inlet and outlet valves were closed after completion of hydrate formation or CH_4-CO_2 exchange. In the aftermath of CH_4-CO_2 exchange, one Stigma pump was filled with methane and the tubings were flushed with methane. This was done to prevent reformation of CO_2 hydrates during depressurization. The pump volume was set to a low value, thereby creating space to accommodate for the produced gas, and the pressure was set to match the pore pressure. The inlet and outlet valves were opened and the pressure was reduced slowly from both sides of the core. When the pressure reached around 48 bar (at least above dissociation pressure), the pressure reduction was

continued with increments of 0.7 bar from inlet side of core (bypass valve closed). The pressure was quickly reduced (constant flowrate of 1-5 mL/min) by 0.7 bar, and then held at constant pressure until pump volume reached a constant value (approximately 24 hours). This stepwise pressure reduction was repeated until all hydrates dissociated. Some of the experiments were conducted with fewer and bigger pressure steps. Pump volume, core surface temperature and pressure readings were logged during the pressure depletion, and some experiments were complemented with resistivity measurements. The confinement pressure was always maintained at least 30 bar higher than the pore pressure.

3.2 MRI imaging

3.2.1 Experimental design

The MRI magnet used to image hydrate dissociation is located at Statoil's research department in Sandsli outside of Bergen. The instrument has a magnetic field strength of 4.7 T and a frequency of 150 MHz, and was acquired as late as fall 2014. It has been subjected to testing and calibration the last couple of months, and the imaging conducted as part of this thesis represents one of the first attempts on hydrate imaging. As a consequence of the newly established laboratory, there are per date no possibilities of cooling, injecting fluids or pressurizing cores inside the magnet. Core preparations were done in collaboration with fellow master student Erik Vadla, and master students Josef Flatlandsmo and Håkon Juliussen contributed on the imaging part.

3.2.2 Experimental procedure

A specimen of the same sandstone cores as described in Section 3.1.4 was completely covered with epoxy except at the core ends. The core ends were immediately fitted with plastic end-pieces which were held in place by the epoxy as it dried up. The core was now sealed and fluids could only be injected through the connections at the end-pieces, see Figure 3.2.2.

Figure 3.2.2: Sandstone core fitted with end-pieces and covered with epoxy.

The core was vacuumed and subsequently saturated with brine containing a salinity of 5 wt%. The brine used is standard sandstone water applied at the reservoir physics group, and contains small amounts of acid to inhibit bacterial growth. After obtaining a brine saturation close to unity, the core was flushed with cyclopentane until irreducible water saturation. The core was then flushed with brine again in order to achieve irreducible cyclopentane saturation. The ratio between water and hydrate former was now appropriate and the core was moved to Statoil and cooled to 2 °C. This temperature is well within cyclopentane hydrate stability under ambient pressure. Following one day with hydrate formation, the core was wrapped with bubble wrap and inserted into the MRI magnet. The bubble wrap was intended to prolong the dissociation time. The MRI software was set to obtain images every second hour for a total of 15 hours. It was used a spin-echo sequence named RARE.

4 Results and Discussion

It has been conducted fifteen successful hydrate formation experiments during the work of this thesis. All experiments are summarized in Table 4. Seven hydrate formations were formed with a temperature of 4.0 °C, while the remaining eight were carried through with temperatures varying between 0.0 and 2.5 °C. The formation pressure was maintained at 83 bar and initial water saturations were fairly constant; they were ranging between 0.57 and 0.70, with twelve of the experiments lying in the interval of 0.64-0.70. The initial salinity was kept at 3.50 wt% and final saturations were calculated from PVT-data. Experiment CO2_33 was subjected to injection of 60 mole% N_2 + 40 mole% CO_2 and the recovery of methane from hydrates was calculated to 0.25. It was also attempted to inject the same mixture into FOR_1 and DEP_11, but both cores experienced initial clogging, most likely due to formation of CO_2 hydrate with excess water. DEP_11 was successfully stimulated and connectivity was resumed, but further research on CH_4-CO_2 exchange was hampered since the gas chromatograph was out of order. All cores, except from FOR_1-4, were eventually depressurized with temperatures varying between -0.4 and 4.2 °C. One additional sandstone core experienced cyclopentane hydrate dissociation while MRI images were obtained. The uncertainties of reported values are briefly discussed at the end of the chapter.

Table 4: List of all experiments including formation temperatures, initial brine salinities and water, hydrate and gas saturations

| Core ID	Formation Temp. [°C]	Salinity [wt%]	S_{wi} [frac.]	S_{wf} [frac.]	S_H [frac.]	S_{gas} [frac.]
CO2_33	4,0	3,50	0,69	0,31	0,49	0,21
DEP_6	1,5	3,50	0,67	0,32	0,45	0,23
DEP_7	2,5	3,50	0,59	0,17	0,53	0,30
DEP_8	2,5	3,50	0,70	0,32	0,49	0,19
FOR_1	0,2	3,50	0,65	0,22	0,55	0,23
DEP_11	0,7	3,50	0,69	0,21	0,61	0,17
DEP_10	4,0	3,50	0,68	0,28	0,52	0,21
DEP_9	0,0	3,50	0,66	0,14	0,67	0,19
HR_57	4,0	3,50	0,66	0,25	0,53	0,22
DEP_13	4,0	3,50	0,66	0,24	0,55	0,22
DEP_12	4,0	3,50	0,67	0,23	0,56	0,21
HR_58	4,0	3,50	0,66	0,25	0,53	0,22
FOR_2	4,0	3,50	0,64	0,23	0,53	0,25
FOR_3	1,2	3,50	0,57	0,25	0,40	0,34
FOR_4	1,2	3,50	0,57	0,19	0,50	0,32

4.1 Hydrate formation

Research on hydrate formation and investigation of parameters that will affect hydrate saturation are important in order to characterize natural hydrate accumulations and to assess the potential for production. Experimental observations from hydrate growth on core-scale can also serve as input to numerical simulators and be used to validate numerical models. A typical hydrate formation curve is presented in Figure 4.1a. This figure shows the consumption of methane gas as hydrates form in core HR_57 (p=83 bar, T=4.0 °C, S_{wi}=0.66, salinity=3.50 wt%). The initial increase in volume is a result of cooling and subsequent contraction of methane gas. The pump has to inject some volume to maintain constant pressure. The following small plateau on the volume graph corresponds to the induction time. This time span varied between experiments as depicted in Figure 4.1b, and confirms the stochastic nature of induction times given in the literature (Sloan, 1998). The induction time is followed by an abrupt increase in volume as hydrates start to form. After about 20 hours, the increase slows down and the formation rate is fairly constant until 125 hours. The reduction in formation rate is a result of limitations in mass transport as hydrates form initially at the interface between water and methane gas. At the end the increase declines and hydrate formation is terminated after 236 hours. The graph is corrected for leakages and the amount of methane that has entered the hydrate is given by the final consumed volume, disregarding the initial cool-down period. This yields a volume of methane of 60 mL, but accounting for the expansion of hydrates mentioned in Section 1.4.1, the final volume increases to 69 mL. The temperature fluctuations shown in the figure is a result of room-temperature fluctuations during day and night. The cooling bath was not able to fixate the temperature completely.
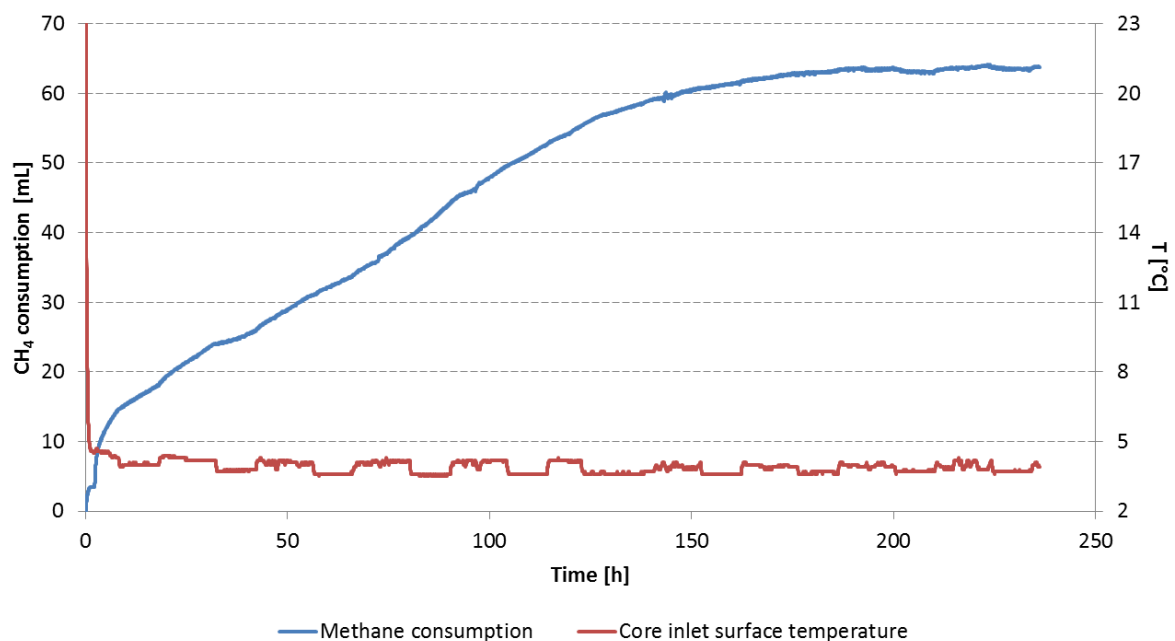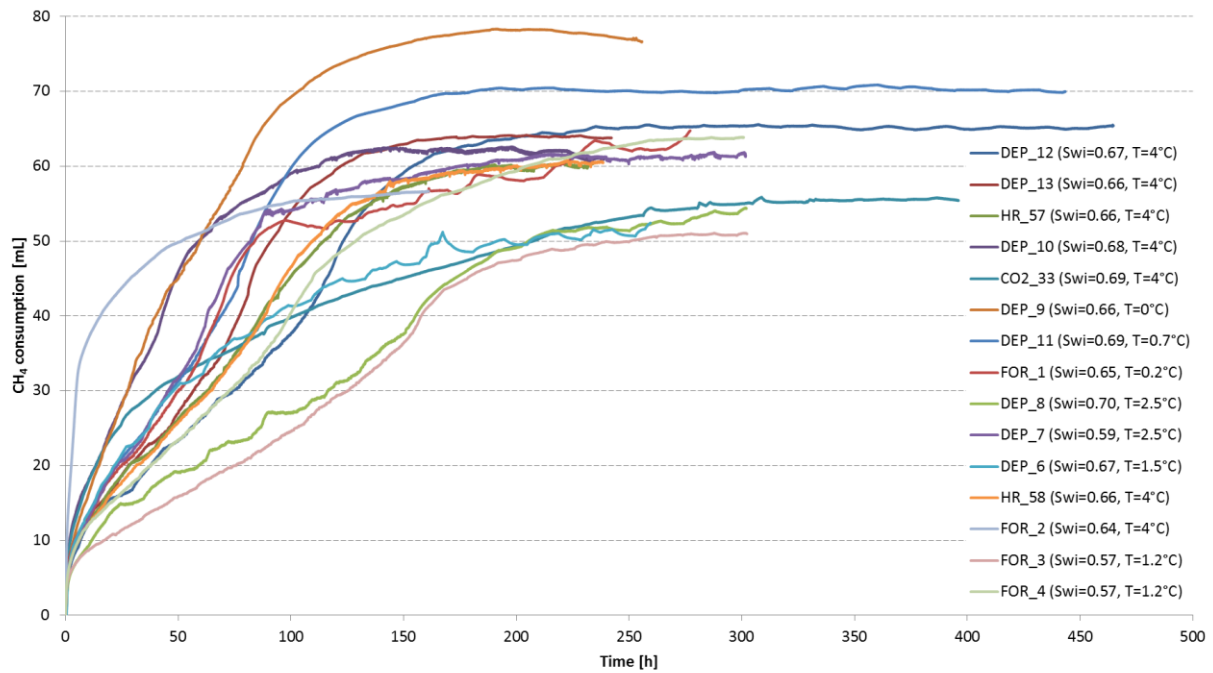

Figure 4.1a: Hydrate formation curve for experiment HR_57. The pressure was maintained at 83 bar and the core had an initial water saturation of 0.66 with 3.50 wt% salinity.
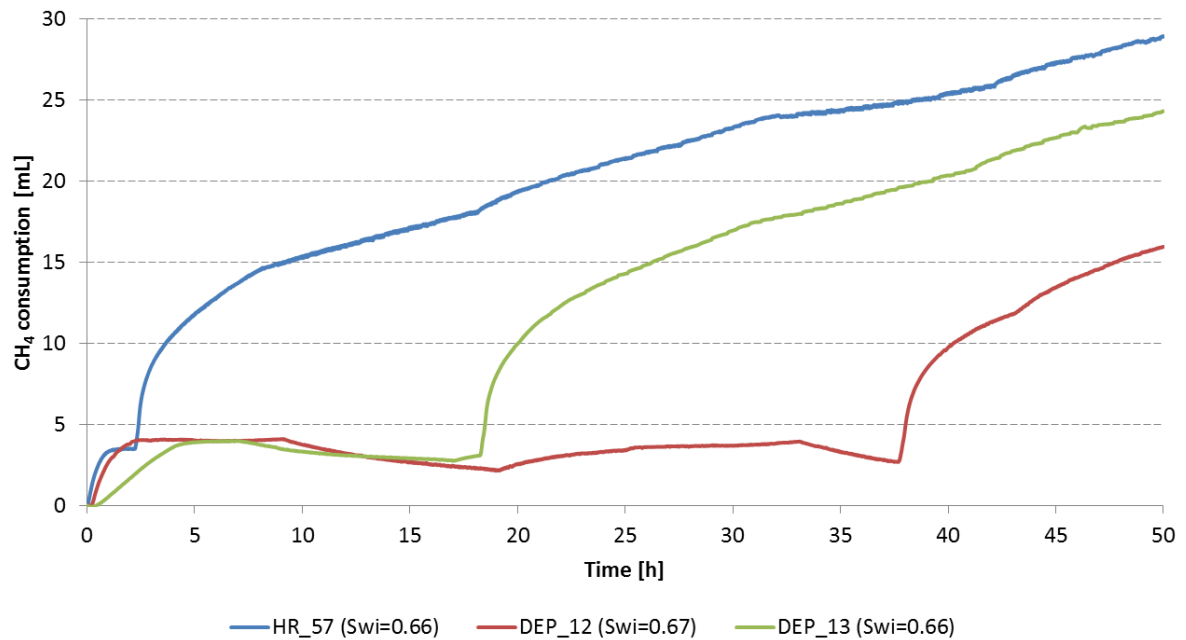
Figure 4.1b: Start of hydrate formation for three different cores. The horizontal plateau on each graph represents the induction time. All three formations were conducted with a pressure of 83 bar, a temperature of 4.0 °C and 3.50 wt% salinity.

Figure 4.1c gives an overview of consumed methane for all experiments. The final volume varies between 51 mL and 77 mL, and the shape of the curves is different between experiments. The following sections will deal with parameters that might affect hydrate formation, like temperature, initial water saturation and salinity. Ersland *et al.* (2009) highlight the important effect of initial water distribution on hydrate formation pattern. A homogenoues water distribution resolves in a homogenous growth pattern, while a heterogenous water distribution leads to a frontal growth moving through the core. However, this aspect is difficult to adress without proper imaging techniques. One should keep in mind that small differences in pore geometry and rock composition will have an impact on hydrate formation, and can lead to minor deviations from the trends obtained by studying individual parameters.
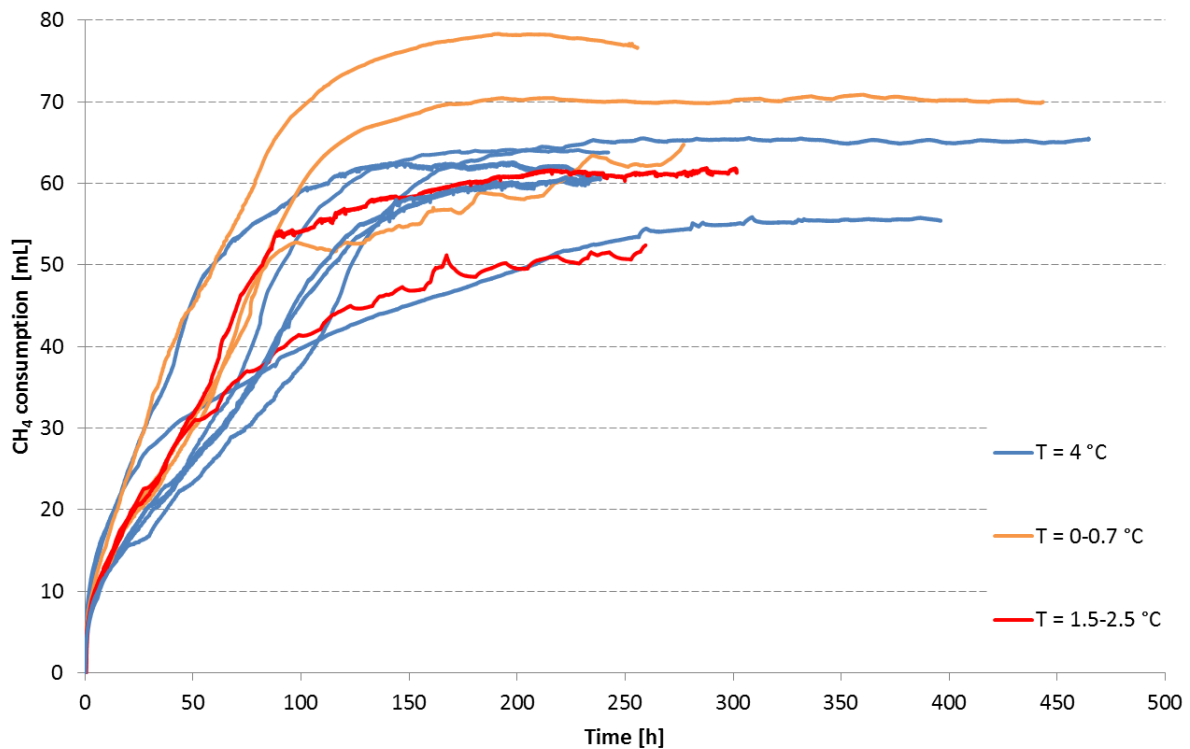
Figure 4.1c: Hydrate formation curves for all experiments. The pressure was set to 83 bar and the salinity was 3.50 wt%. Initial water saturation and formation temperature are denoted on the figure.

4.1.1 Effect of temperature

One may expect the formation rate to increase with decreasing formation temperature as the driving forces increase when the formation takes place well below hydrate stability temperature (Sloan, 1998). In accordance with this, DEP_9 (p=83 bar, T=0.0 °C, S_{wi}=0.66, salinity=3.50 wt%) which has the coldest formation temperature, has the second fastest hydrate formation. FOR_2 (p=83 bar, T=4.0 °C, S_{wi}=0.64, salinity=3.50 wt%) has a steeper incline in consumed methane volume, but this formation experienced an increased growth rate because it was a secondary formation. The core was previously saturated with hydrates, but the formation was not successfully completed since the pump volume was too low and the supply of methane gas was insufficient. The hydrate was then dissociated through thermal stimulation while keeping the pressure at 83 bar, and a new hydrate formation initiated when the core was re-cooled. The rate of hydrate formation is known to increase when hydrates are formed from components which previously have been part of another hydrate (Sloan and Koh, 2008). The phenomenon is called the "memory effect" and one proposed explanation for the increased formation rate is given by Rodger (2000): Liberated methane gas from dissociation of hydrates remains up-concentrated in the water phase and enhances the amount of water with access to methane molecules. This theory may explain the increased formation rate observed in FOR_2 as the solubility of methane gas in water has a stronger dependency on pressure than on temperature (Duan and Mao, 2006); the decrease in solubility associated with the temperature increase to around 20 °C was negligible compared with the increase in solubility as a result of keeping the pressure at 83 bar. Figure 4.1.1a shows formation curves according to temperature. There is a tendency for the coldest formations to be fastest, but the trend is not clear and more results are needed to state any conclusion. Mork (2002) found in her work that the degree of subcooling had no observable effect on formation rate. This is also supported by Kneafsey *et al.* (2007) who have observed decreasing rates with increasing driving forces with respect to both temperature and pressure. DEP_8 (p=83 bar, T=2.5 °C, S_{wi}=0.70, salinity=3.50 wt%) and FOR_3 (p=83 bar, T=1.2 °C,

50

S$_{wi}$=0.57, salinity=3.50 wt%) have slowest hydrate formations because of operational problems with the cooling bath which led to stepwise temperature reductions. This was also the case for experiment FOR_4 (p=83 bar, T=1.2 °C, S$_{wi}$=0.57, salinity=3.50 wt%) and these three experiments are not included in Figure 4.1.1a. The formation rate of experiment FOR_4 is not as influenced by the stepwise temperature reduction as FOR_3, see Figure 4.1c, and the initial water saturations and experimental conditions are identical for the two experiments. Disregarding the experiments with stepwise temperature reductions and looking at Figure 4.1.1a, it seems like the shape of the formation curves is insignificantly affected by formation temperature.

Figure 4.1.1a: Hydrate formation curves for twelve experiments diversified by temperature. The pressure was maintained at 83 bar and the salinity was 3.50 wt%. Initial water saturation varied between 0.57-0.70.

Figure 4.1.1b portrays final hydrate saturation as a function of formation temperature. Some experiments previously conducted by the hydrate research group are added to increase number of data points; only five experiments have been conducted previously with similar initial water saturation and salinity. The trend seems to be in favor of higher hydrate saturations at lower temperatures, but the effect is not apparent for the intermediate temperatures. There is a wide saturation span for experiments performed at 4.0 °C, indicating that the effect of temperature is limited when considering temperature discrepancies of 3-4 °C.
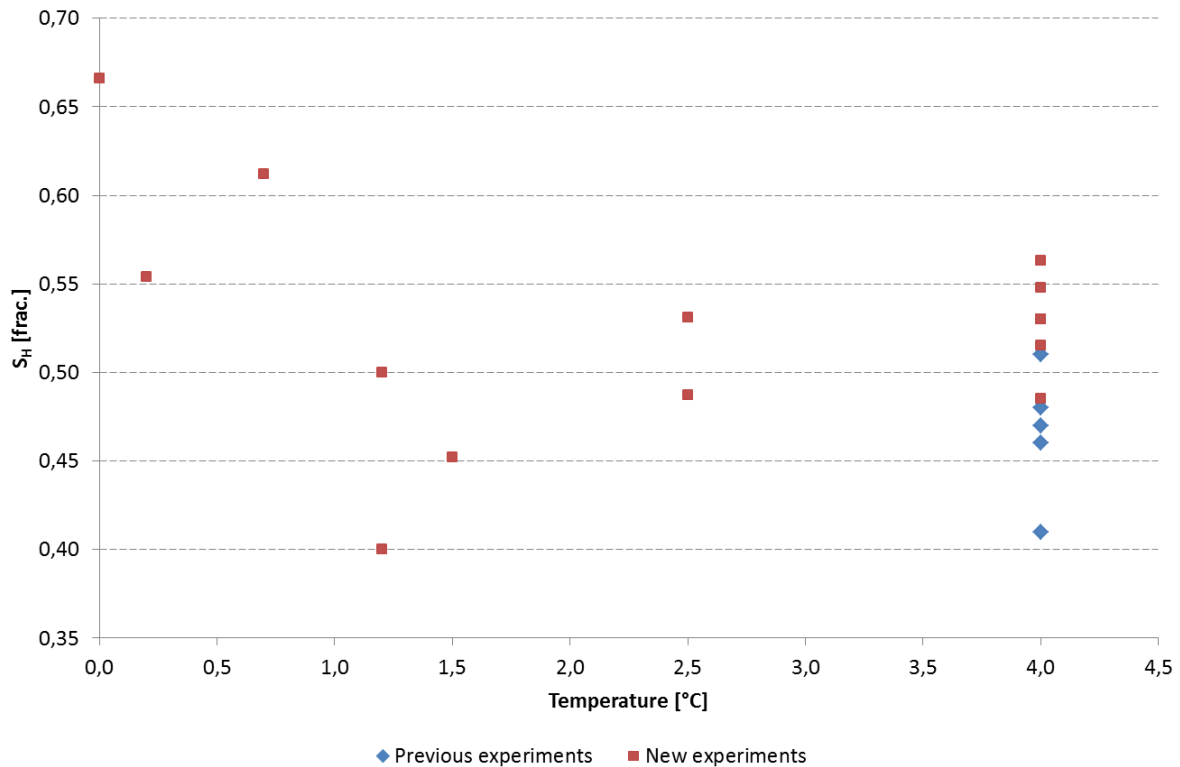
Figure 4.1.1b: Final hydrate saturation as function of formation temperature. The pressure was set to 83 bar and the salinity was 3.50 wt%. Initial water saturation varied between 0.57-0.70. Three identical values are observed on 4.0 °C and a hydrate saturation of 0.53. Previous experiments are collected from in-house database (Hauge, 2013).

4.1.2 Effect of initial water saturation

The initial water saturation has been kept within 0.57-0.70 in the experiments accomplished in this thesis. They can nonetheless serve to complement earlier work conducted by the hydrate research group, and in total the experiments can elucidate the effect of initial water saturation. Final hydrate saturation is plotted against initial water saturation in Figure 4.1.2a. The formation temperature was kept at 4.0 °C and the salinity was fixed on 3.50 wt%. The highest hydrate saturations seem to occur for intermediate water saturations between 0.40 and 0.70. Previous experiments seem to have a top in the middle of this interval, but the new experiments suggest that the hydrate saturation remains high until the end of this interval. More research is needed for water saturations between 0.50 and 0.60. The saturation of hydrates remains low outside the water saturation interval of 0.40-0.70. At low initial water saturations, the formation of hydrates is mainly limited by availability of water. When all the water is consumed, or if the salinity is increased to a level that inhibits further formation, hydrate formation stops and results in low saturations. At high initial water saturations, the amount of water and increasing salinity will probably not give the most decisive impact. In this case, the high water saturation implies less contact area between water and gas in the core. After initial hydrate formation has taken place in the surface area between water and gas, further growth will be inhibited by the hydrate layer which separates the fluids. Figure 4.1.2b shows a clear trend between initial water saturation and final water saturation. The final saturation is increasing with initial saturation, and this supports the above considerations and matches the findings of Hauge *et al*. (2012).
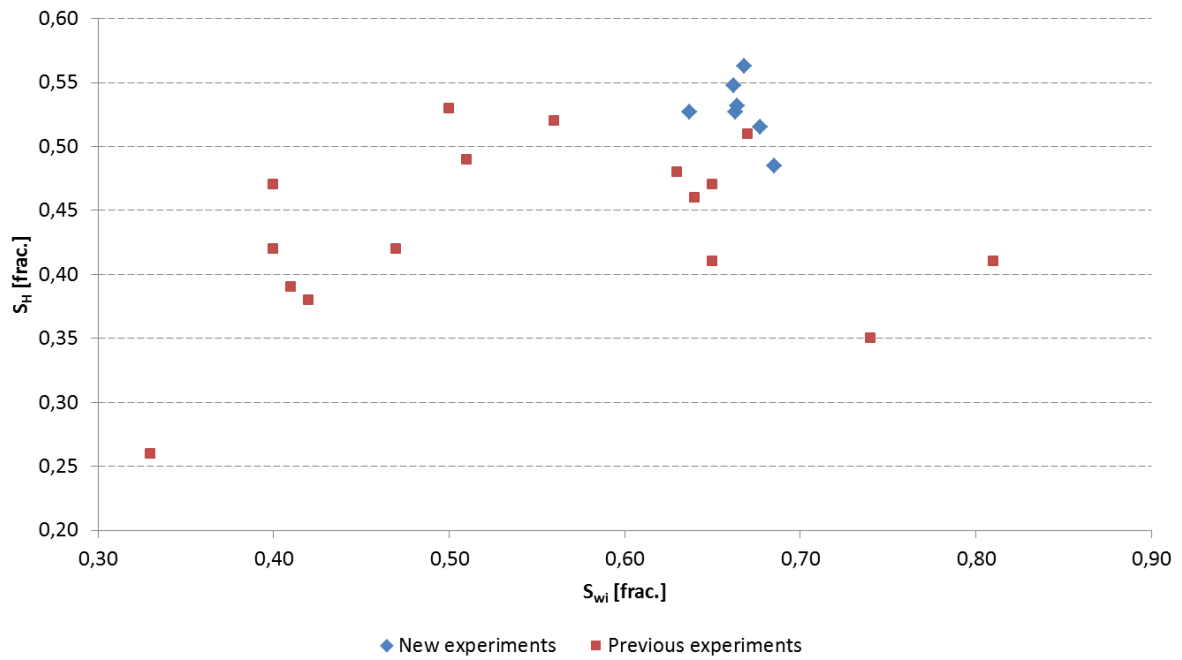
Figure 4.1.2a: Relationship between final hydrate saturation and initial water saturation. All formations were conducted with 83 bar, 4.0 °C and 3.50 wt% salinity. Previous experiments are collected from in-house database (Hauge, 2013).
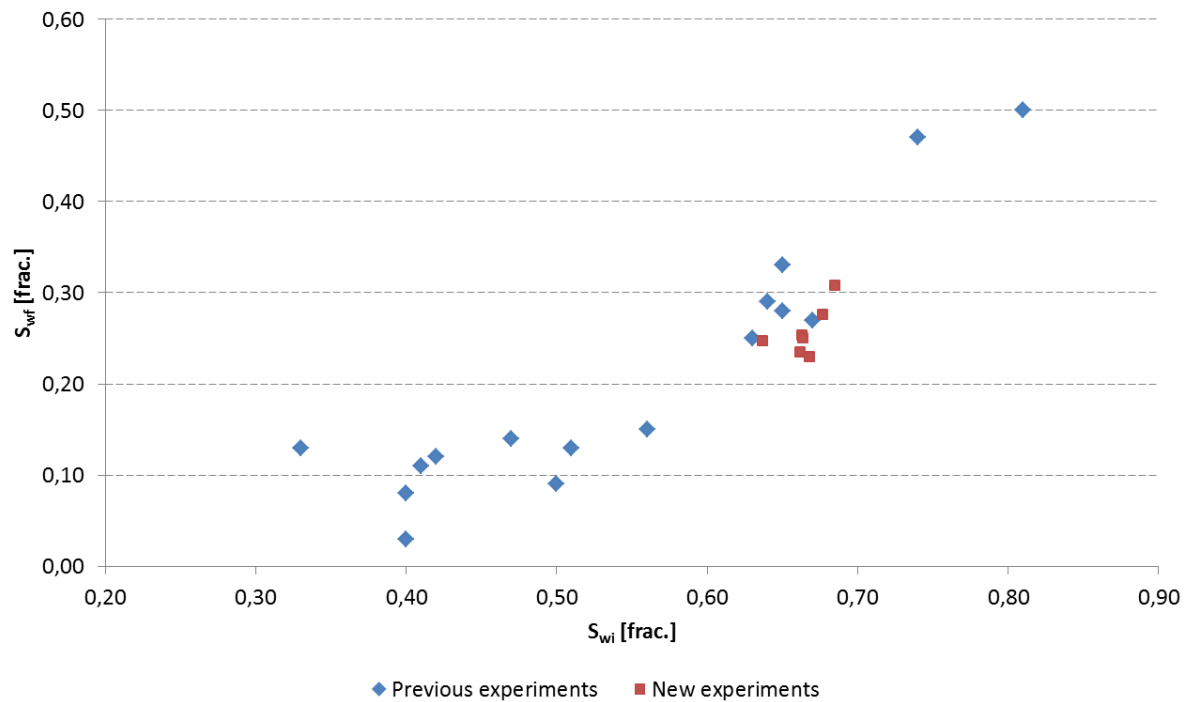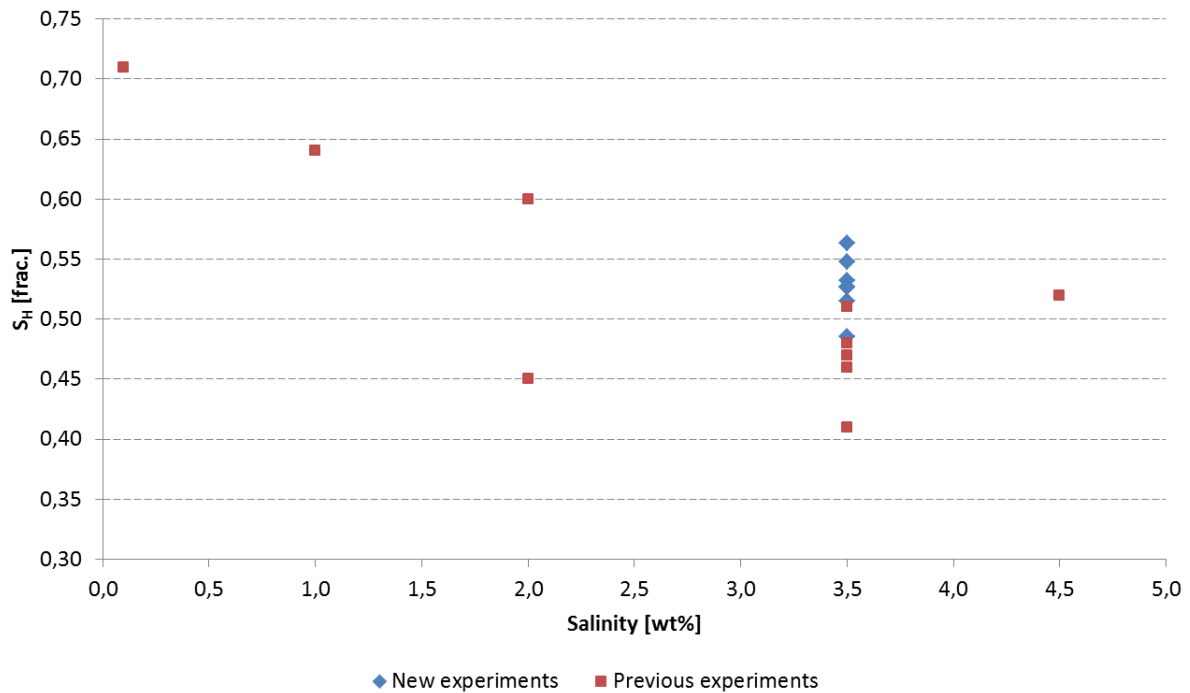

Figure 4.1.2b: Relationship between final water saturation and initial water saturation. All formations were conducted with 83 bar, 4.0 °C and 3.50 wt% salinity. Previous experiments are collected from in-house database (Hauge, 2013).

4.1.3 Effect of salinity

Figure 4.1.3 summarizes all experiments with initial water saturations ranging from 0.60 to 0.70 and with a formation temperature of 4.0 °C. The data points are scarce for low salinity values but they are trending towards higher hydrate saturations for lower salinity values. This indicates that the hydrate saturation is not only limited by a shielding hydrate layer between fluids for high initial water saturations, but that increasing salt content during formation will additionally decrease the final hydrate saturation for high initial water saturations. These findings are in accordance with Stevens *et al*. (2008) and Husebø *et al*. (2009).


Figure 4.1.3: Hydrate saturation as a function of initial water salinity. All formations were conducted with 83 bar, 4.0 °C and an initial water saturation ranging from 0.60 to 0.70. Previous experiments are collected from in-house database (Hauge, 2013).

4.1.4 Hydrate formation with resistivity measurements

Experiments HR_57 and HR_58 were supported with resistivity measurements during hydrate formation. Logging of resistivity is one way of characterizing hydrates located in the subsurface, and it is important to investigate the relationship between resistivity values and hydrate saturations. Figure 4.1.4a displays resistivity, methane consumption and temperature for the first ten hours of hydrate formation for HR_57 (p=83 bar, T=4.0 °C, S_{wi}=0.66, salinity=3.50 wt%). Both the resistivity and the methane consumption increase during the cooling period. The salt ions decrease their movability with decreasing temperature and the conductivity decreases. When the cooling is terminated, one hour with induction time follows and the resistivity stabilizes on around 9.5 Ωm. At the onset of massive growth, depicted by the sharp increase in methane consumption, resistivity drops with almost 3 Ωm. This effect was observed for both experiments and earlier by Birkedal *et al*. (2011).One possible explanation can be increased salt consentration at the interface between water and methane where the hydrate formation initiates. If hydrate formation happens uniformly throughout the core, the salt consentration will increase simultanously along the length of the core

54

and can contribute to an increase in conductivity at the early start of hydrate formation. Birkedal *et al.* (2011) points on the possibility of temperature increases from the exothermic formation reaction. Temperature readings from the core inlet surface do not show any sign of temperature alterations, but local temperature increases leading to an increase in conductivity cannot be disregarded.
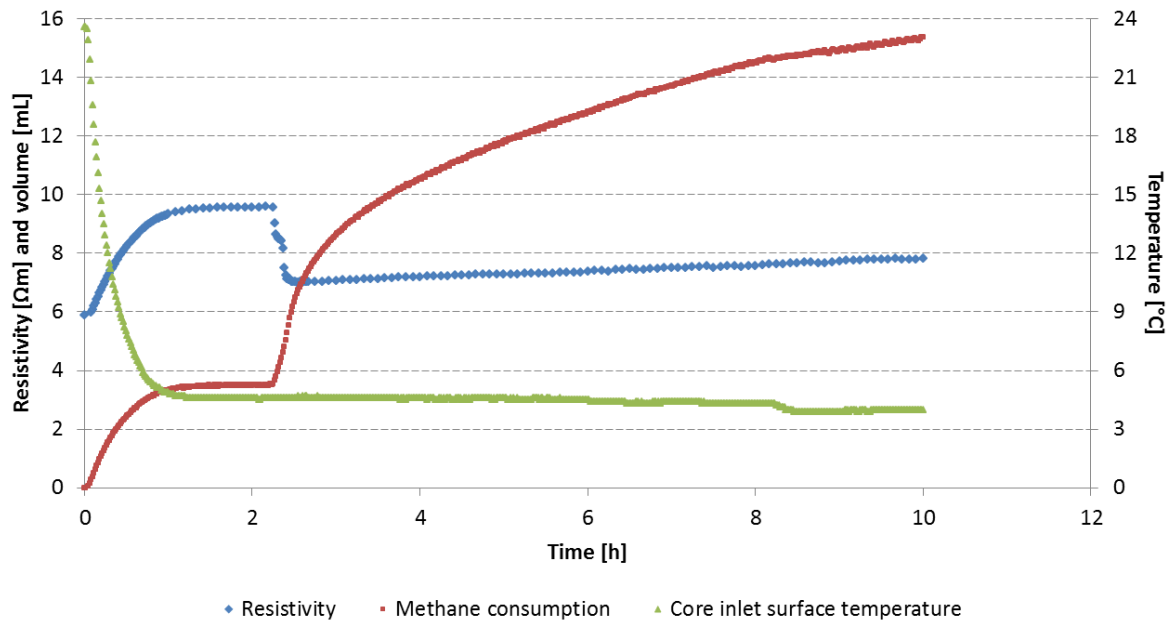
Figure 4.1.4a: Initial evolution of resistivity, methane consumption and temperature for HR_57. The pressure was maintained at 83 bar and the core had an initial water saturation of 0.66 with 3.50 wt% salinity.

The following two figures show resistivity as a function of time during the whole hydrate formation process. Figure 4.1.4b is from experiment HR_57 (p=83 bar, T=4.0 °C, S_{wi}=0.66, salinity=3.50 wt%) and Figure 4.1.4c is from HR_58 (p=83 bar, T=4.0 °C, S_{wi}=0.66, salinity=3.50 wt%). It is apparent from Figure 4.1.4b that the sharp increase in resistivity delays the increase in methane consumption by more than 100 hours. The initial resistivity of almost 10 Ωm is not recovered until the hydrate saturation reaches 0.28. In comparison other experiments recovered initial resistivity after a hydrate saturation of 0.20 (Ren *et al.*, 2009). A sharp increase in resistivity is not observed until the hydrate saturation researches 0.37. This indicates an underestimation of hydrate saturation during initial stage of formation. The increased salinity may compensate for the initial blocking and retention of charged particles and the resistivity increases sharply when the hydrate saturation becomes elevated enough to severely increase tortuosity and thereby lengthen the charged particles effective travel length. These considerations and the shape of the resistivity curve favor a uniform hydrate growth and homogenous initial water saturation. If the growth progressed from the ends of the core like a moving piston, the increase in resistivity would likely appear soon after hydrates had started forming. Final resistivity values level out at 60 Ωm, but there are noticeable fluctuations at the final stage of hydrate formation. At this point the water saturation has decreased to 0.25 and the resistivity is likely sensitive to small perturbations in water distribution. Local dissociation and reformation can lead to redistribution of hydrates and cause fluctuations in resistivity values. It should be noted that the reported hydrate saturations are based on PVT-data. The resistivity values can only be used to estimate water saturations. They cannot be used to infer mutually saturations between hydrates and free gas.
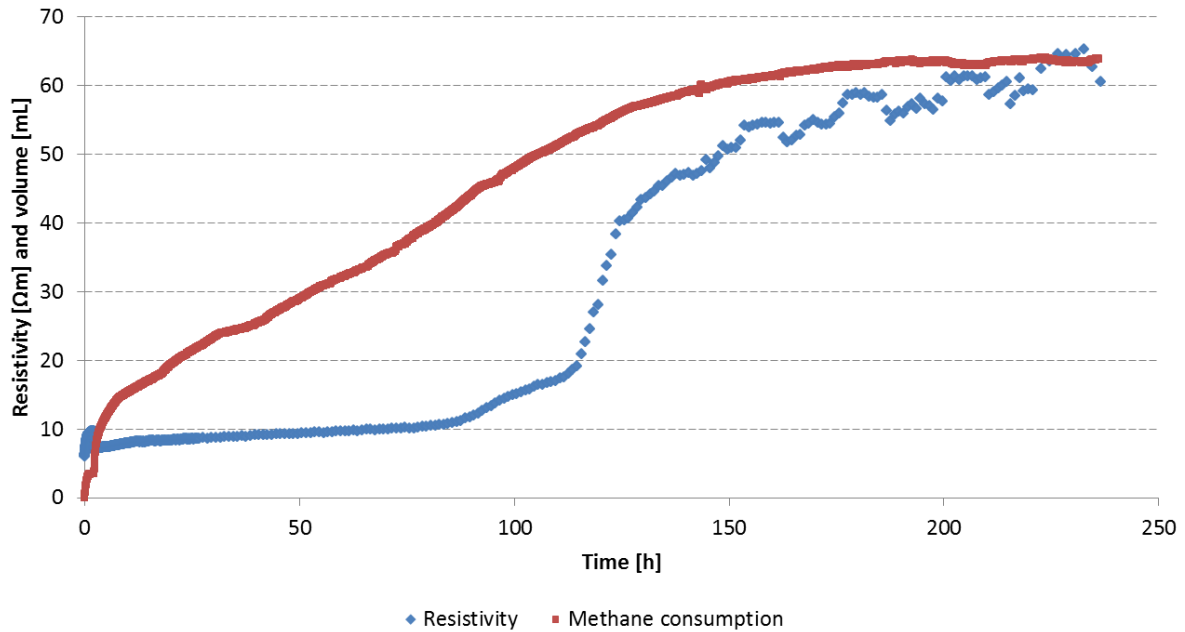
Figure 4.1.4b: Resistivity and methane consumption as functions of time for HR_57. Pressure and temperature were maintained at 83 bar and 4.0 °C, and the core had an initial water saturation of 0.66 with 3.50 wt% salinity.

Core HR_58 experiences a different resistivity evolution than HR_57, as seen in Figure 4.1.4c. The initial resistivity of almost 12 Ωm is recovered at a hydrate saturation of 0.10 and the resistivity increases faster. This points to a more piston-like hydrate growth than in the case of HR_57. The sharp increase in resistivity is less pronounced and comes at a later stage when hydrate saturation has reached 0.47. These observations regarding the hydrate growth pattern come exclusively from resistivity values as the shape of the methane consumption curves is similar between the two experiments. Final resistivities are both around 60 Ωm and are in good agreement with similar hydrate saturations.
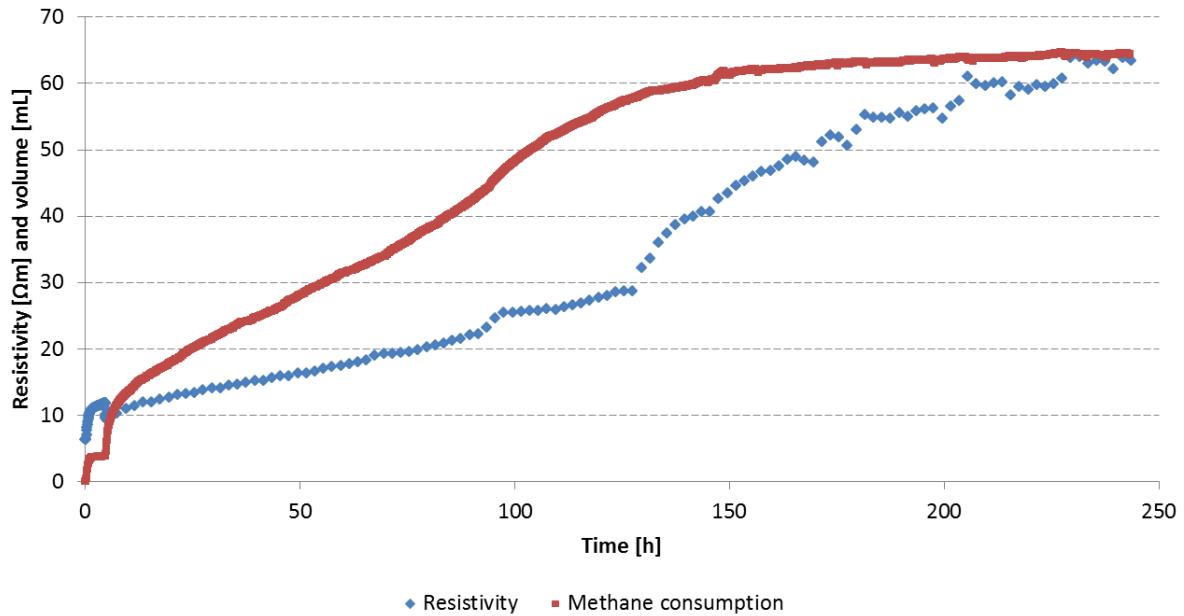
Figure 4.1.4c: Resistivity and methane consumption as functions of time for HR_58. Pressure and temperature were maintained at 83 bar and 4.0 °C, and the core had an initial water saturation of 0.66 with 3.50 wt% salinity.

In Figure 4.1.4d, water saturations calculated from PVT-data are plotted against water saturations calculated from resistivity values. The points should lie on the black diagonal if the two methods give equal saturations. The initial saturation points are fixed with respect to water saturation calculated from resistivity. This is done to avoid an apparent increase in water saturation due to the initial drop in resistivity. It is clear from the figure, as noted above, that the resistivity method gives an overestimation of water saturation during the beginning of the growth period. In the case of HR_58, this trend is quickly reversed and the resistivity calculations underestimate water saturations. Towards the end of the growth period, the degree of underestimation is pronounced for both cores. Hauge (2011) observed exactly the same trend in previously conducted experiments in the hydrate research group but the agreement between saturation values are better in these results. Notice that the saturations are calculated from *Archies 2. law* with fixed values of 1 and 2.17 for the proportionality constant *b* and saturation exponent *n*, respectively. The proportionality constant *b* is dependent on tortuosity and is expected to vary with increasing hydrate saturation. Modelling has shown that this also applies for the saturation exponent *n* (Spangenberg, 2001). The match between saturation values can be improved by empirical fitting of these parameters.
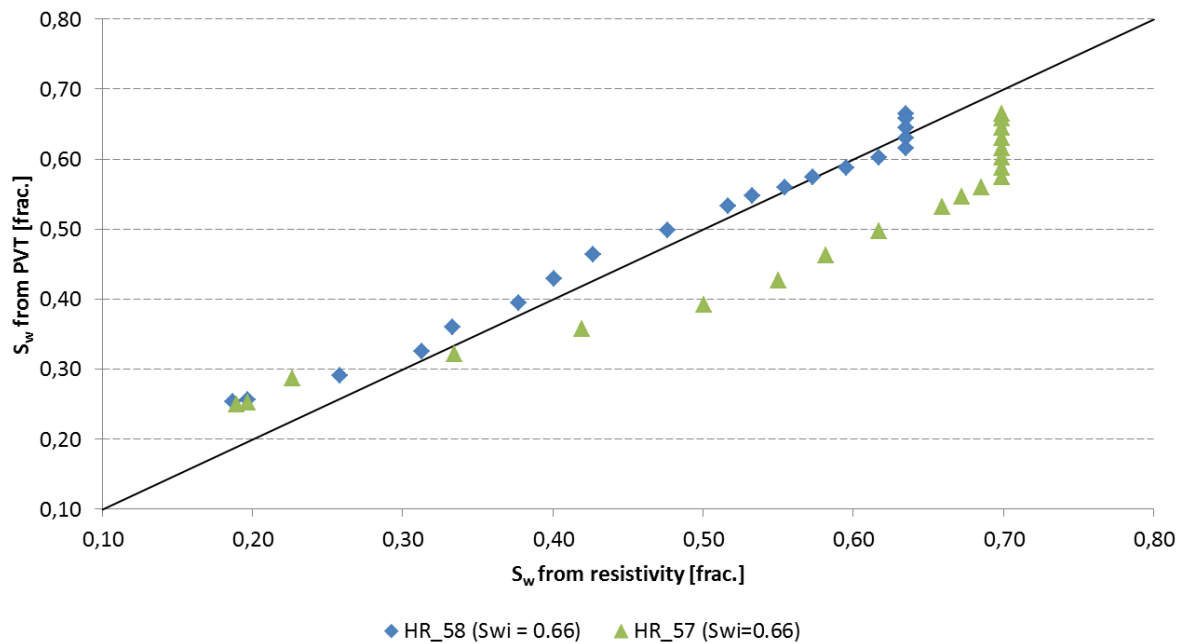
Figure 4.1.4d: Crossplot of water saturation calculated from PVT-data and resistivity values. Pressure and temperature were maintained at 83 bar and 4.0 °C, and the cores were initially saturated with water containing 3.50 wt% salinity.

4.2 CH$_4$-CO$_2$ exchange

Experiment CO2_33 was the only experiment which underwent CH$_4$-CO$_2$ exchange with subsequent monitoring of produced fluids. After hydrate formation, the core had obtained a hydrate saturation of 0.49 and a water saturation of 0.31. With almost one third of the pore volume occupied by water, pure nitrogen was first injected to see how the differential pressure evolved and to avoid possible formation of CO$_2$ hydrates. Pressure evolution with time is depicted in Figure 4.2a for the three first days of injection. The inlet pressure increased much faster than the outlet pressure, and injection was eventually stopped without any production on day 1. During the following night, inlet and outlet pressures had equalized and injection was recommenced with 60 mole% N$_2$ + 40 mole% CO$_2$. The inlet pressure immediately surpassed the outlet pressure, but eventually the outlet pressure became high enough to allow for production. The differential pressure dropped to zero again in the following night, and from day 3 and onwards there were no problems with the pressure response throughout the core. This shows that nitrogen can be used initially to effectuate proper flow in the core. One drawback with injection of pure nitrogen is significant dissociation of methane hydrates and production of water. However, it was not observed any water production from the mass flow meter; production of water would result in immense peaks in the mass flow.
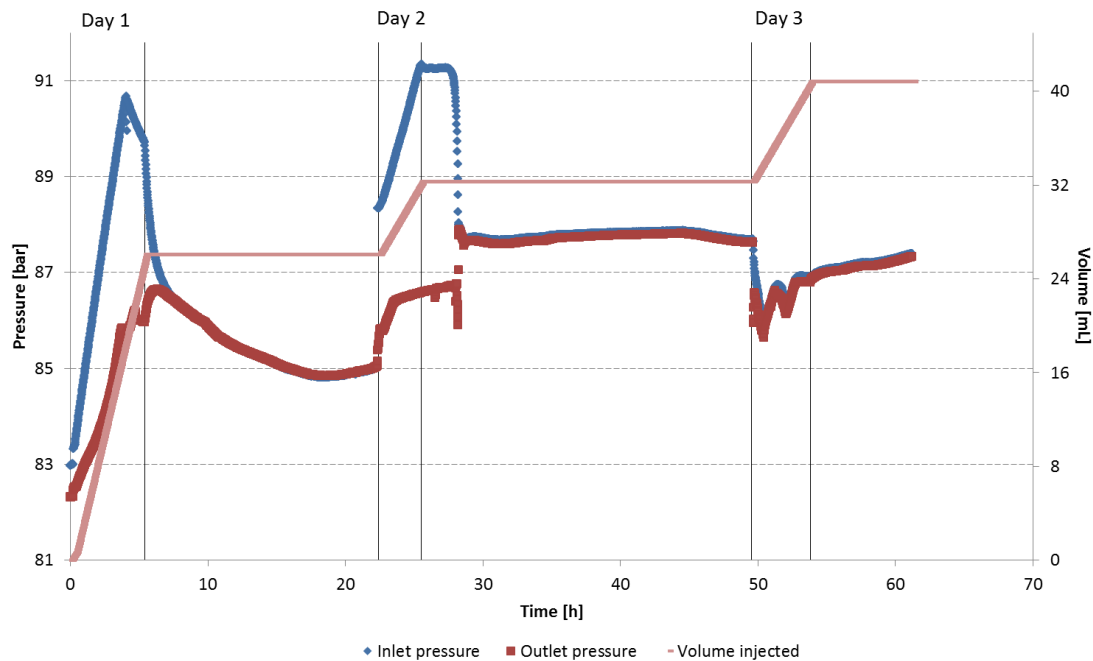
Figure 4.2a: Initial pressure evolution at inlet and outlet of core CO2_33. Temperature was maintained at 4.0 °C and initial saturation of hydrate and water were 0.49 and 0.31, respectively.

A mixture of 60 mole% N_2 + 40 mole% CO_2 was injected during daytime for nine consecutive days. The injection rate varied between 2-6 mL/h. Figure 4.2b gives an overview of different effluent molefractions as a function of injected pore volume. Each black vertical line represents a break in time from one day to another. The first day starts with no recognition of methane as the tubings were flushed with nitrogen (small amounts of CO_2 were present) prior to production. The molefraction of methane increases rapidly to over 90 % and is a result of free methane gas originally located in the core and inlet/outlet tubing. It is assumed that all free methane gas has been produced before hydrate-bounded methane is liberated. This is not entirely true but the assumption has no qualitative implications and is convenient for recovery calculations. The peak in methane molefraction is followed by an increase in nitrogen and CO_2 fraction. The molefraction of nitrogen reaches the injection value of 60 % after approximately 0.5 PV injected, whereas CO_2 reaches its injection value of 40 % after around 2 PV injected. This can be explained by CO_2 molecules exchanging with methane molecules in the hydrate. Formation of CO_2 hydrates with excess water will also contribute to a lower molefraction of CO_2. It can be seen that the molefraction of methane increases at the start of each day. CO_2 molecules will be able to diffuse deeper into the core and exchange with uncontacted methane hydrate during the periods of shut-off. Injection of CO_2 at daytime increases the concentration of CO_2 again and the driving forces for diffusion are reestablished. The molefraction of methane gets a new peak after 2.5-3 PV injected. A possible explanation for this peak can be redistribution of hydrates which enables CO_2 molecules to come in contact with previously unavailable methane hydrate. The production was intended to be prolonged beyond the nine days presented in Figure 4.2b, and that would have revealed if additional peaks in the molefraction of methane could occur.
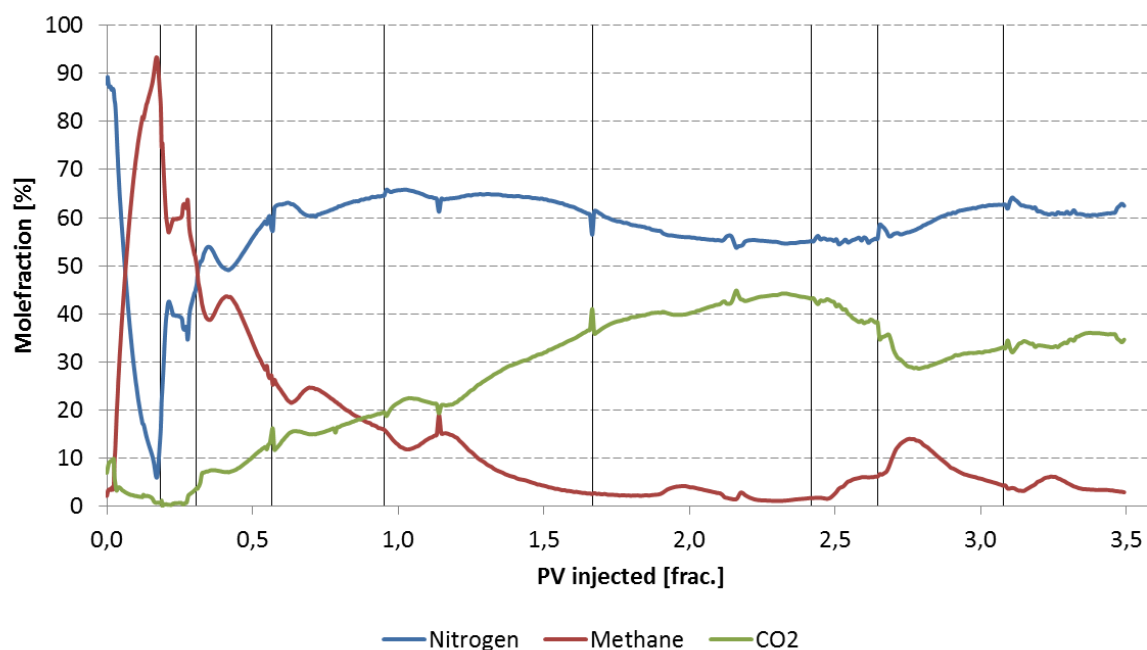
Figure 4.2b: Molefraction of effluents as function of pore volume injected in core CO2_33. A mixture of 60 mole% N_2 + 40 mole% CO_2 was injected with volume-rates ranging from 2 to 6 mL/h. Vertical bars represent breaks in time from one day to another.

The total production of methane (from free gas in the core and hydrate-bounded methane) reached almost 0.15 moles and resulted in a recovery of 0.44. The recovery of methane from hydrates was approximately 0.25, and Figure 4.2c presents cumulative methane produced and methane recoveries as function of pore volumes injected. Previously experiments conducted by the hydrate research group obtained methane recoveries from hydrates ranging between 0-0.52. Some of the earlier experiments had implemented a spacer dividing the core in two, and this artificial modification can be one reason for the high recovery values found by Graue *et al*. (2008). The main reason for the low recovery value in this experiment is likely due to a leakage that occurred after injection of around 1.7 pore volumes of fluid. The leakage was not discovered during the execution of the experiment, but Figure 4.2d indicates loss of produced fluids. Figure 4.2d displays cumulative amount of nitrogen produced [moles] as a function of cumulative amount of nitrogen injected [moles]. Initially the amount of nitrogen produced increases rapidly since the tubings originally were filled with nitrogen. The ratio between injected and produced amounts stays close to unity until the amount of injected nitrogen reaches 0.3 moles. This means that the amount of nitrogen injected equals the amount of nitrogen produced, as is expected from conservation of mass. Pressure and temperature conditions are outside of nitrogen hydrate stability, but minor amounts of nitrogen can exchange with methane molecules in the small cavities (Park *et al*., 2008). At the end of the experiment, the ratio between amount of nitrogen produced and amount of nitrogen injected drops to around 0.5, implying that half of the injected nitrogen is lost before flowing through the mass flow meter. Assuming a similar loss of methane gas at the end of production, the recovery of methane from hydrates is estimated to be 0.29. The occurrence of the leakage was probably situated at the safety pressure valve in front of the gas chromatograph, see Figure 3.1.1a. If the inflow pressure was set to high, the safety pressure valve would decrease the pressure by venting out some of the produced fluids. All other connections and valves are also prone to leakages and small leakages may transpire during ongoing experiments. The reported recovery values are hence conservative estimates. The experiment supports earlier

findings, see Section 2.1, and demonstrates a fast initial recovery which rapidly decreases. This can be explained by a slow diffusion driven exchange process once initial exchange has taken place by CO_2 in direct contact with methane hydrates. It seems like the high water saturation contributes to decrease the contact area between CO_2 and methane hydrates, and lowers the recovery rate as observed by Yang *et al*. (2008).
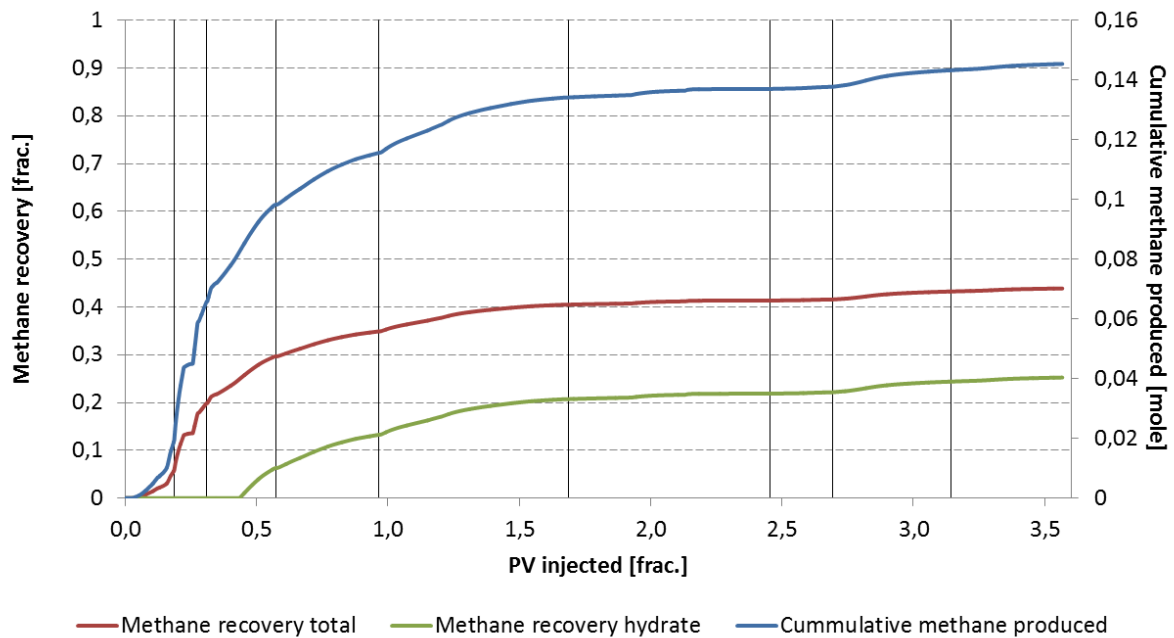

Figure 4.2c: Methane recovery and cumulative methane produced as function of pore volumes of fluid injected (CO2_33). Vertical bars represent a break in time from one day to another.
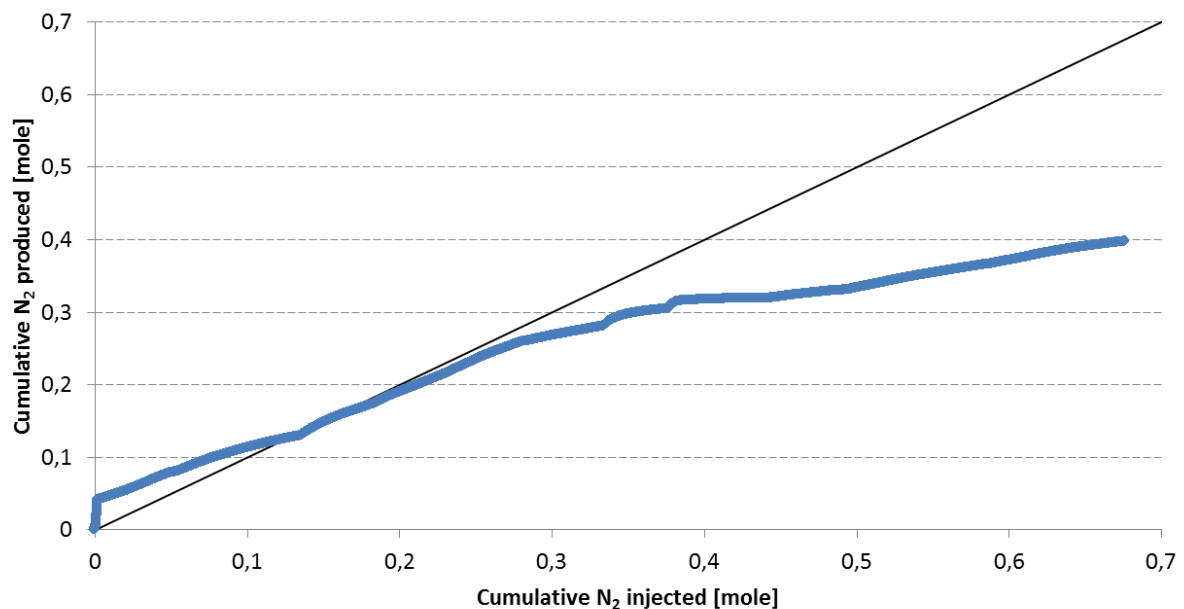

Figure 4.2d: Crossplot between amount of nitrogen injected and amount of nitrogen produced. Black diagonal is for reference.

## 4.2.1Injection of nitrogen leading to clogging of cores

Experiment FOR_1 ended with a hydrate and water saturation of 0.55 and 0.22, respectively, after completion of hydrate formation. The temperature was maintained at 0.5 °C and pure nitrogen was injected initially to observe the effect on differential pressure. Figure 4.2.1a gives an implicit overview of differential pressure and temperature as a function of injection time. The inlet pressure increases rapidly as nitrogen is injected, but there is no response on outlet pressure. The injection was stopped for one night, recommenced the day after, and then stopped for a timespan of approximately 26 days. During the long time period there is no sign of alterations in differential pressure. Outlet pressure is in fact monotonically decreasing, but that is because of a small leakage observed at an outlet connection, and led to termination of the experiment not long after. At the end, the inlet pressure was set to a constant pressure of 95 bar and the temperature was incrementally increased with a couple of degrees centigrade. The added heat resulted in expansion of gases and an increase in outlet pressure, but there is no sign on Figure 4.2.1a of improvements in connectivity. The most obvious difference between this experiment and experiment CO2_33 is the temperatures in which the experiments were carried through. This experiment was conducted with a formation and injection temperature of around four degrees centigrade less than CO2_33, and the hydrate saturation after formation was slightly greater. These differences can be enough to make the core impermeable to gas flow, but it is not possible to deduce whether the core was plugged or just the end-pieces. The experiment shows that pure nitrogen was not able to obtain flow even when applied for an extended period of time.
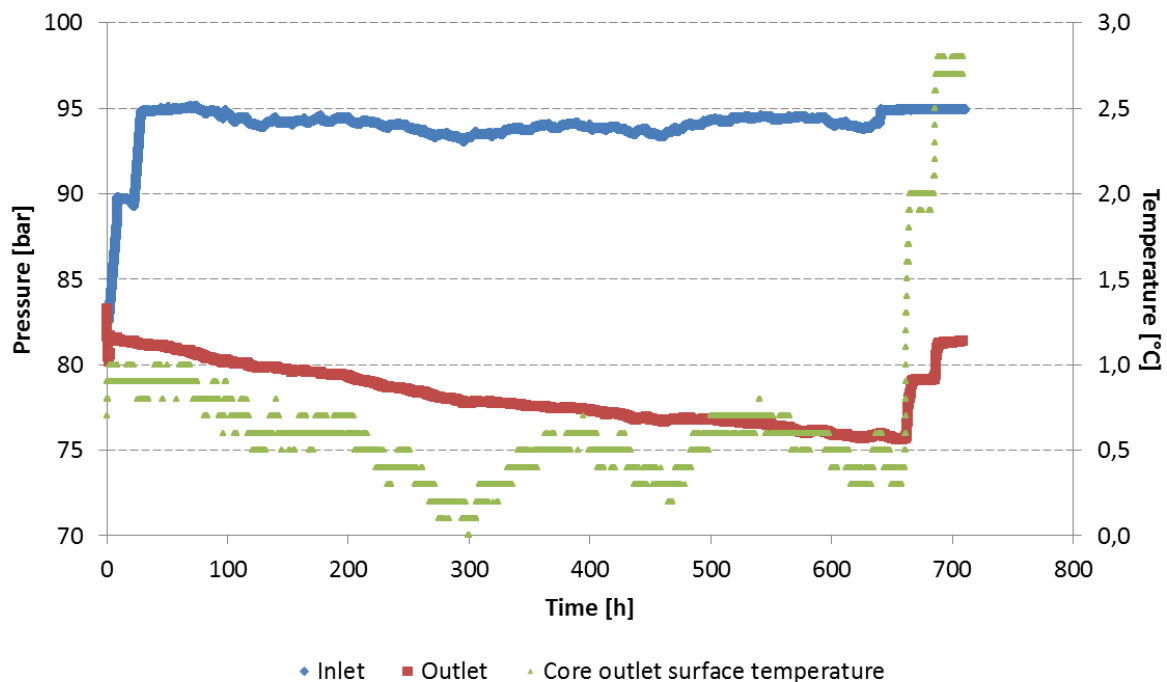
Figure 4.2.1a: Pressure evolution at inlet and outlet of core FOR_1, in addition with core outlet surface temperature. Initial saturation of hydrate and water were 0.55 and 0.22, respectively.

Another observation of nitrogen's incapability to restore flow is given in experiment DEP_11. The temperature was initially held at 0.7 °C and the core had a hydrate and water saturation of 0.61 and 0.21, respectively. Pure nitrogen was injected at inlet end and inlet pressure increased immediately to 95 bar without any effect at the outlet end. Inlet pressure was maintained at 95 bar for 15 days

and the temperature was increased to around 3.5 °C, still without any significant change in differential pressure. Nitrogen was then introduced at the outlet end and held at constant pressure 84.9 bar for one hour, before the pump was connected back to inlet end and held at constant pressure 93 bar. This point in time marks the start of Figure 4.2.1b. The final and only successful step towards obtaining connectivity was achieved after a short temperature increase to almost 8 °C. The outlet pressure mimics the temperature alteration but as the temperature is stabilized on 4.7 °C, the outlet pressure increases to the constant value of 93 bar. The pressure was then reduced to 86 bar from both inlet and outlet ends, and a mixture of 60 mole% N_2 + 40 mole% CO_2 was injected at the inlet end. Connectivity was now restored and outlet pressure corresponded with inlet pressure, as can be seen at the end of Figure 4.2.1b. Again it is not possible to determine if the hydrate plug was located in the core or in the end-pieces. However, thermal stimulation was demonstrated as a suitable technique to gain flow in a hydrate blocked core/production line.
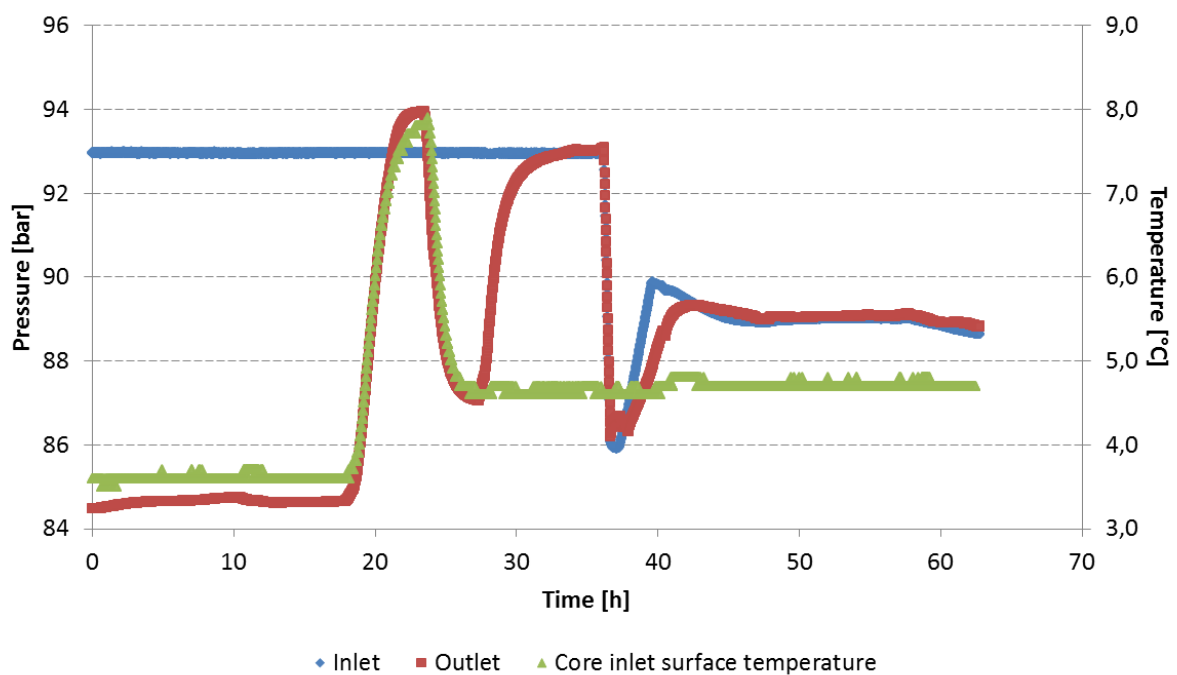
Figure 4.2.1b: Final pressure evolution at inlet and outlet of core DEP_11, in addition with core inlet surface temperature. Initial saturation of hydrate and water were 0.61 and 0.21, respectively.

In the aftermath of experiment FOR_1 and DEP_11, a new flow loop was implemented in setup B as described in Section 3.1.3. This modification makes it possible to conduct flow through the inlet end-piece and thereby deduce if the hydrate plug is situated there. A similar modification can be made on the outlet end-piece and will provide a possibility to determine if the core is clogged.

4.3 Pressure depletion

4.3.1 Pressure depletion of core containing a mixture of methane and CO_2 hydrates

When injection of nitrogen and CO_2 was terminated in core CO2_33, it was attempted to flush the core with methane gas. During pressure depletion of a mixed hydrate consisting of methane and CO_2, methane hydrates will dissociate first and free CO_2 in the core can create new CO_2 hydrates with liberated water. The intention was to displace all free CO_2 in the core to avoid reformation of CO_2 hydrates. The methane flush was not successful as the core got clogged, and depressurization was started with both nitrogen and CO_2 present in the core. Pressure was reduced from both ends of core down to 45.7 bar, and further downwards only from inlet side. Initial pressure steps are depicted in Figure 4.3.1a. The differential pressure decreases towards zero during the pressure step of 42.9 bar, which is the same pressure step as when dissociation is observed. In hindsight it is clear that the initial pressure steps were held in constant pressure for too short a time to determine if dissociation was initiated. Therefore it is not possible to conclude that hydrate dissociation did not start before 42.9 bar. It was anticipated that the dissociation pressure would be much lower since Hågenvik (2013) achieved dissociation at 34.5 bar for a mixed hydrate system with free nitrogen present. A more detailed analysis of dissociation pressure is presented later in this section.
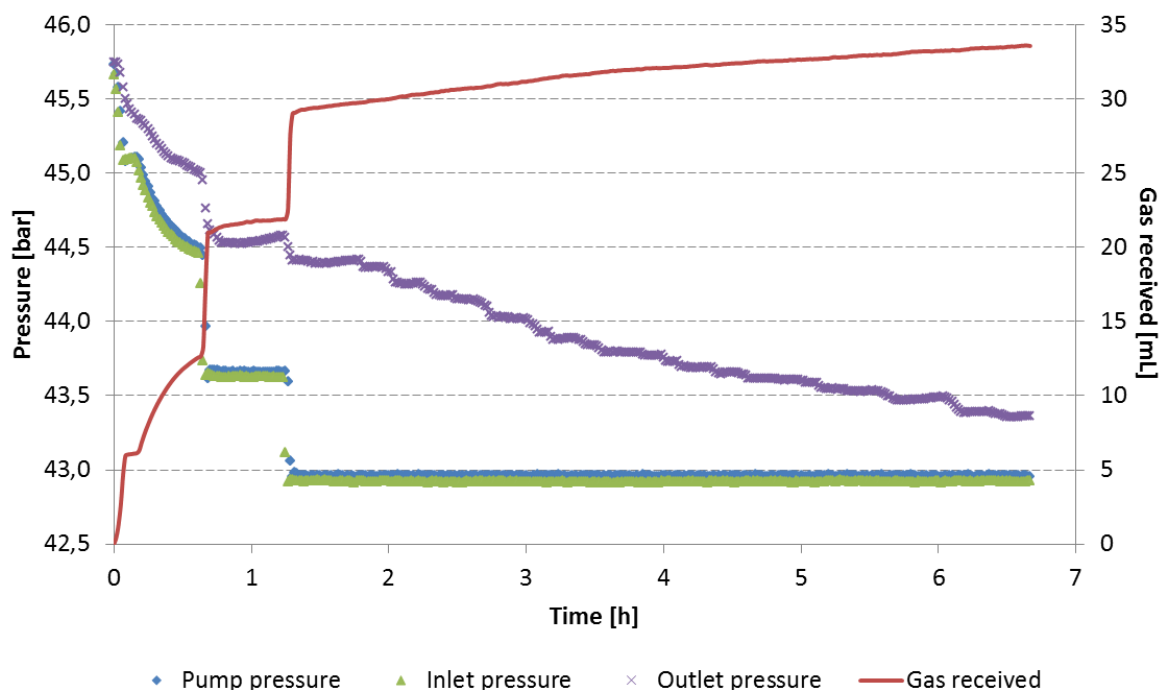
Figure 4.3.1a: Implicit representation of initial differential pressure during depressurization of core CO2_33. The core was depressurized from both ends down to 45.7 bar, and further pressure reductions were conducted from inlet side. Temperature was maintained at 4.0 °C.

Figure 4.3.1b presents received gas from every pressure step except the last one. The final pressure reduction was performed from 33.5 bar to 21.7 bar, but it was not enough volume left in the pump to receive all the liberated gas, so the pressure increased to 26 bar in the end. This led to an underestimation of received gas at the final pressure step, and the recovery of methane from

hydrates is calculated to 0.64. It should be noted that the recovery of methane already was 0.25 after the exchange process. The main reason for not achieving the theoretical value of unity is found in the stepwise depressurization scheme utilized in this thesis. Every pressure reduction was carried out by increasing the pump volume, and all liberated gas from dissociation during the actual pressure reduction was not detected. When the pressure reduction was finalized and the pump was set to constant pressure, liberated gas was detected as changes in pump volume. Recovery values of methane account for only phase two and three in the dissociation scheme of Xiong *et al*. (2012), see Chapter 2.2. Gas volumes presented in Figure 4.3.1b is not corrected for leakages, which also lead towards a reduction in methane recovery. The impact of leakages is however small, since the leakage rate was found to be 0.02 mL/h (at 83 bar) during hydrate formation and is likely smaller for lower pressures. The fluctuations in the volume graphs are caused by temperature variations during day and night.
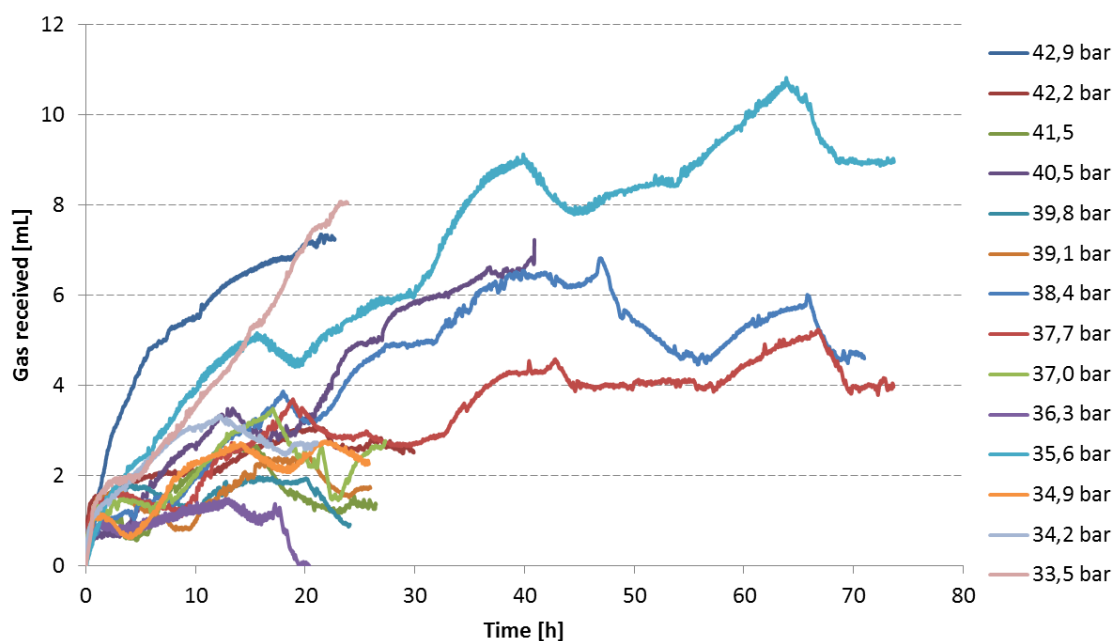
Figure 4.3.1b: Received gas volume for every pressure step conducted on core CO2_33, except for the last pressure reduction from 33.5 bar down to 21.7 bar. Note that each volume-graph denotes received volume at constant pressure, i.e. the volume change associated with reducing the pressure is not shown. The temperature was maintained at 4.0 °C.

It is clear from Figure 4.3.1b that the hydrate dissociated over a wide range of pressures. This is as expected since the hydrate is anticipated to exist in mixed form of both methane and CO_2 molecules. By coupling the amount of released gas at each pressure step to hydrate compositions calculated by CSMGem, one can compute a plot relating the hydrate composition to relative amount of hydrates. The amount of hydrates is normalized over all liberated gas during dissociation. It should be emphasized that Figure 4.3.1c serves as a qualitative figure, and the actual values need extended commenting. The key feature with Figure 4.3.1c is that it highlights the mixed nature of hydrates which have undergone CH_4-CO_2 exchange. Some of the methane hydrate has not been contacted by CO_2 molecules and is therefore intact after exchange. Methane hydrate closest to injected CO_2 fluid is maybe completely converted to CO_2 hydrates, with exception of small cavities which are best stabilized by methane molecules (Sloan, 1998). The amount of large cavities which have absorbed CO_2 molecules is likely decreasing towards more and more inaccessible methane hydrates. The result

of a CH_4-CO_2 exchange is a spectrum of different hydrate compositions, which is illustrated in Figure 4.3.1c.
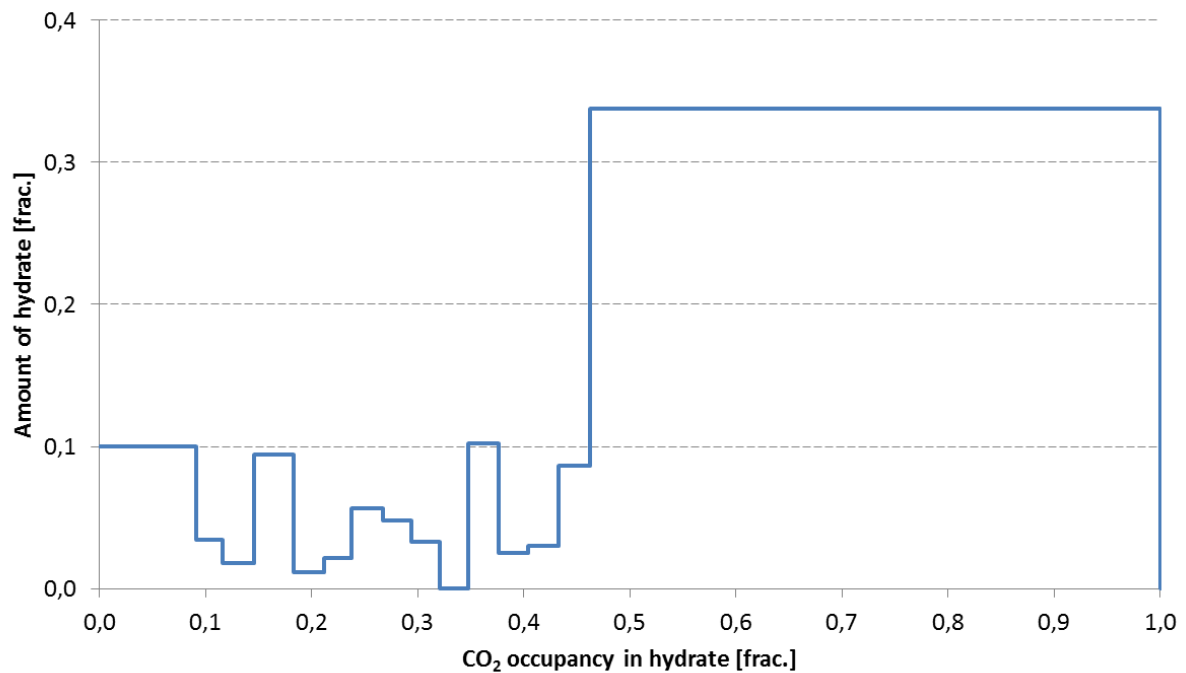
Figure 4.3.1c: Relative amount of hydrates with different composition (degree of CO_2 occupancy in hydrate) for core CO2_33. Hydrate composition is calculated by CSMGem and is based on distinct dissociation pressures.

Hydrate compositions shown in Figure 4.3.1c are calculated from CSMGem, which is a bulk hydrate simulator not directly analogous to this experiment, see Section 1.4.2. A comparison between methane hydrate dissociation pressures calculated by CSMGem and experimental values obtained in this thesis is presented in the next chapter. The experimental results show that even pure methane hydrates melt over a range of pressure values, and this will of course occlude the calculations behind Figure 4.3.1c, which are based on distinct dissociation pressures for different compositions. The calculations are inputted with a brine salinity of 3.50 wt%, but the initial salinity upon depressurization will be higher and decrease towards 3.50 wt% at the end. Compositions of hydrates with more than 50% CO_2 are not differentiated because of the final big pressure step from 33.5 bar to 21.7 bar. Pure CO_2 liberated in pressure steps down to 39.1 bar would experience a phase change from liquid to gas on its way from core to pump. But the presence of nitrogen and methane gas increase the pressure needed to liquidize CO_2 (Jung *et al.*, 2010), and the composite fluid will be a gas for all pressure steps. Finally, the dissociation pressures do not take into account the effect of nitrogen. Nitrogen gas will have a destabilizing effect on methane and CO_2 hydrates under the prevailing experimental conditions (Kvamme, 2015). The graph in Figure 4.3.1c should therefore be shifted rightwards compared with the x-axis since dissociation would happen at lower pressures without presence of nitrogen.

Core DEP_11 was depressurized from one end in two pressure steps: the first from 50.0 to 42.0 bar and the second from 42.0 to 27.0 bar. The recovery of methane is calculated to 0.50, and the main reason for the low value is loss of methane gas during the increase in pump volume which induces the pressure reduction. Differential pressure was monitored but a disconnection between pressure

66

transducers and computer led to loss of data. Figure 4.3.1d shows received gas volume and core surface temperature after first pressure reduction down to 42.0 bar. The temperature is initially reduced, partly because of the pressure reduction and partly because of the endothermic dissociation. When the dissociation process slows down, the temperature resumes its constant value controlled by the cooling bath. This illustrates that even a core surrounded by a constant temperature cooling jacket will be prone to temperature depressions during rapid dissociation.
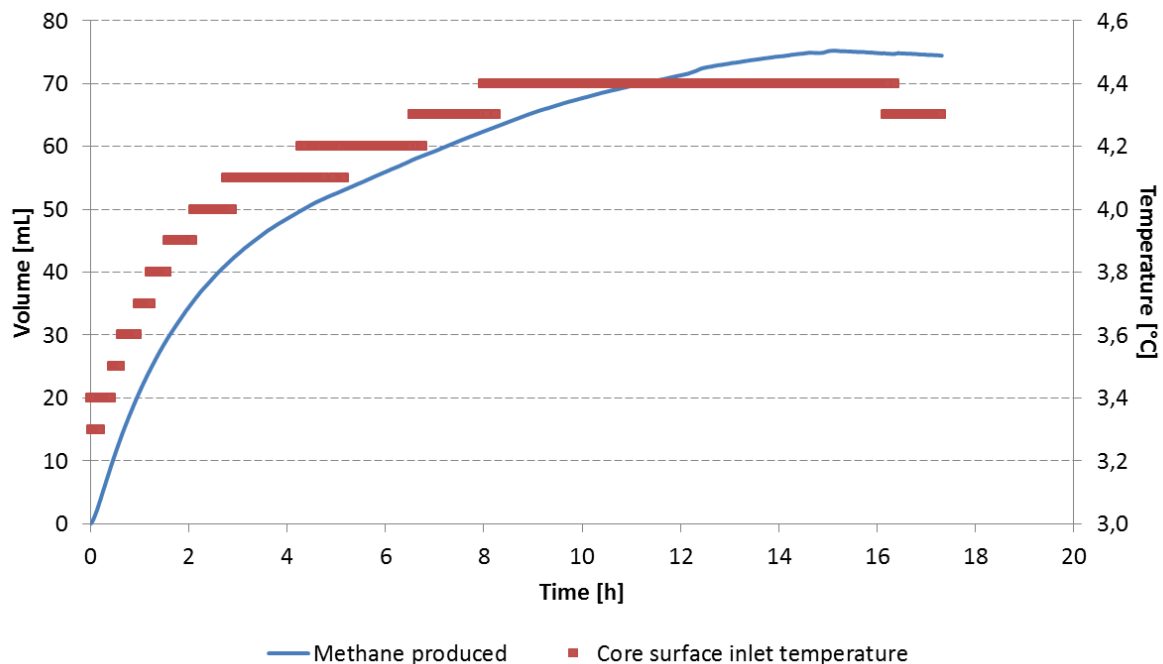

Figure 4.3.1d: Received gas during the first pressure step at 42.0 bar for experiment DEP_11. The volume change associated with reducing the pressure is not displayed.

4.3.2 Pressure depletion of cores containing pure methane hydrates

A total of nine cores, all containing pure methane hydrates, were pressure depleted using the stepwise depressurization technique described for CO2_33. All cores were slowly depressurized down to 48 bar from both ends, and further depressurized in increments of 0.7 bar from inlet side. When most of the methane gas was liberated, pressure was reduced in a big step down to somewhere between 27-30 bar. A summary of dissociation pressures and methane recoveries are presented in Table 4.3.2. The recovery values of methane are of minor importance and are obscured by the design of the depressurization scheme as discussed in Chapter 4.3.1. Methane recovery for experiment HR_58 is omitted because of trouble with the cooling bath which led to erroneous volume graphs. Two of the dissociations were complemented with resistivity measurements to add knowledge on initial flow behavior.

Table 4.3.2: List of average depressurization temperatures, methane recoveries and observed dissociation pressures

| Core ID	Depressurization Temp. [°C]	$R_{CH4/depressurization}$ [frac.]	Start of dissociation [bar]
DEP_6	1,7	0,83	39,6
DEP_7	2,8	0,75	39,3
DEP_8	2,8	0,62	40,0
DEP_10	3,6	0,59	44,3
DEP_9	-0,4	0,77	38,7
HR_57	4,0	0,69	45,2
DEP_13	4,0	0,79	45,2
DEP_12	4,0	0,67	47,3
HR_58	4,0	-	47,3

Figure 4.3.2a portrays a comparison of theoretical dissociation pressures and values obtained from the experiments. Theoretical values are calculated by CSMGem and are based on a brine salinity of 3.50 wt%. It seems to be a trend where the experimental dissociation pressures exceed the theoretical values, which indicates that methane hydrates are less stable in sandstone cores compared to bulk hydrates. The average pore diameter of the sandstone cores used in these experiments is 125 microns (Graue *et al*., 2008), and Uchida *et al*. (2004) found pores of maximum 50 microns to have a destabilizing effect on methane hydrates. The detection of dissociation pressure used in these experiments is not a sensitive approach, and initial small-scale dissociation is likely not captured in the timeframe of about 24 hours. Small fluctuations in temperature will also affect the dissociation pressure and temperature values presented in Table 4.3.2 are average temperatures. The inputted salinity of 3.50 wt% is an approximation since the salinity is up-concentrated during hydrate formation and will decrease back to 3.50 wt% during pressure depletion. Experiment DEP_6 (leftmost value in Figure 4.3.2a) experienced a high dissociation pressure compared to the theoretical value. The temperature sensor failed during pressure depletion in this experiment and an average temperature was stipulated based on the cooling bath. Based on Figure 4.3.2a and the measured dissociation pressure it seems like the temperature was closer to 2 °C in experiment DEP_6.
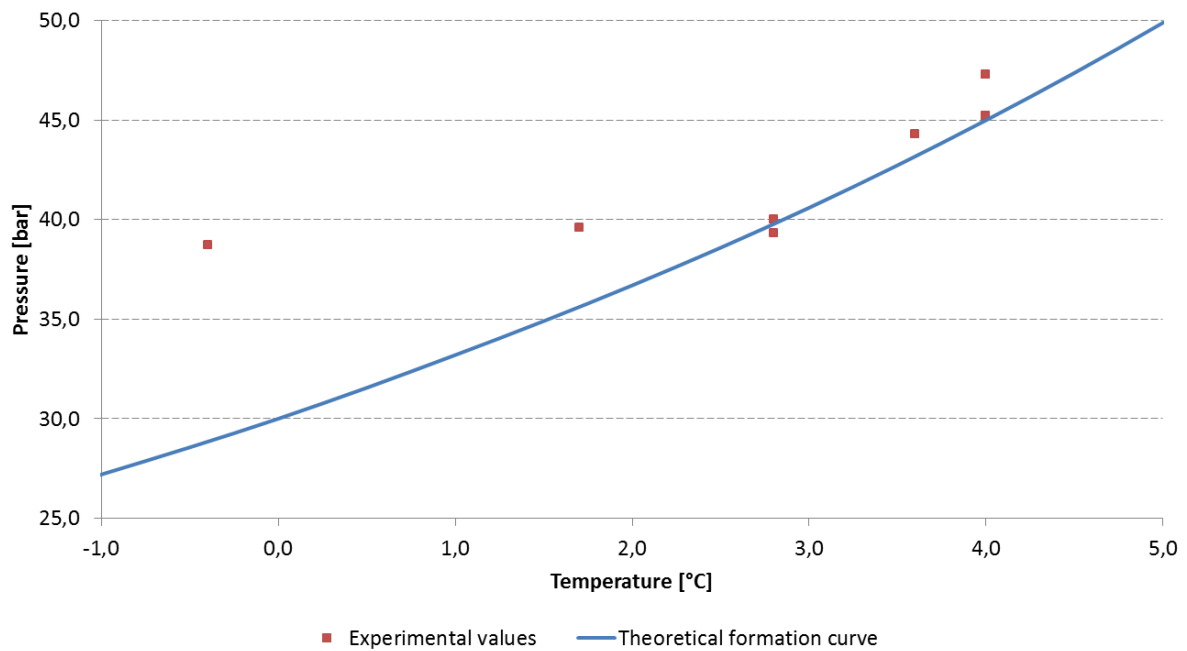
Figure 4.3.2a: Comparison of theoretical and experimental dissociation pressures. The theoretical formation curve is calculated by CSMGem with a brine salinity of 3.50 wt%. Two identical values are observed on both (4.0°C, 45.2 bar) and (4.0°C, 47.3bar).

Figure 4.3.2b gives an overview of produced methane at each pressure step for core DEP_8. Hydrate saturation prior to pressure depletion was 0.49 and temperature was maintained at 2.8 °C. Hydrate dissociation started when pressure reached 40.0 bar, and continued all the way down to 34.4 bar. The last pressure step was conducted between 34.4 bar and 27.0 bar and led to full dissociation. It is evident from Figure 4.3.2b that dissociation takes place over a range of pressure values, and this behavior was observed for all experiments. A few comments can be made to address this phenomenon, which was also observed by Ersland *et al.* (2009) who needed three pressure steps to complete dissociation. First of all, hydrates in a porous media will not be in complete thermodynamical equilibrium, see Section 1.4.2. This leads to a range of dissociation pressures corresponding to hydrates with different chemical potential instead of one distinct dissociation pressure. Secondly, the endothermic nature of hydrate dissociation will work to counteract further dissociation. The temperature is maintained at a constant value and the heat conductivity of the quartz mineral constituting the sandstone core is good, but local temperature drops may inhibit and prolonge hydrate dissociation. Lastly, salinity will decrease with increasing amount of dissociation and the remaining hydrate becomes more stable towards the water phase. The pressure depletion conducted by Ersland *et al.* (2009) had an initial water saturation of around 0.50 with only 0.1 wt% salinity. The brine salinity change will be less profound during dissociation in that case, and may explain why hydrate dissociation took place with fewer pressure steps. A varying brine salinity is one drawback working with closed water systems containing a static salt content.
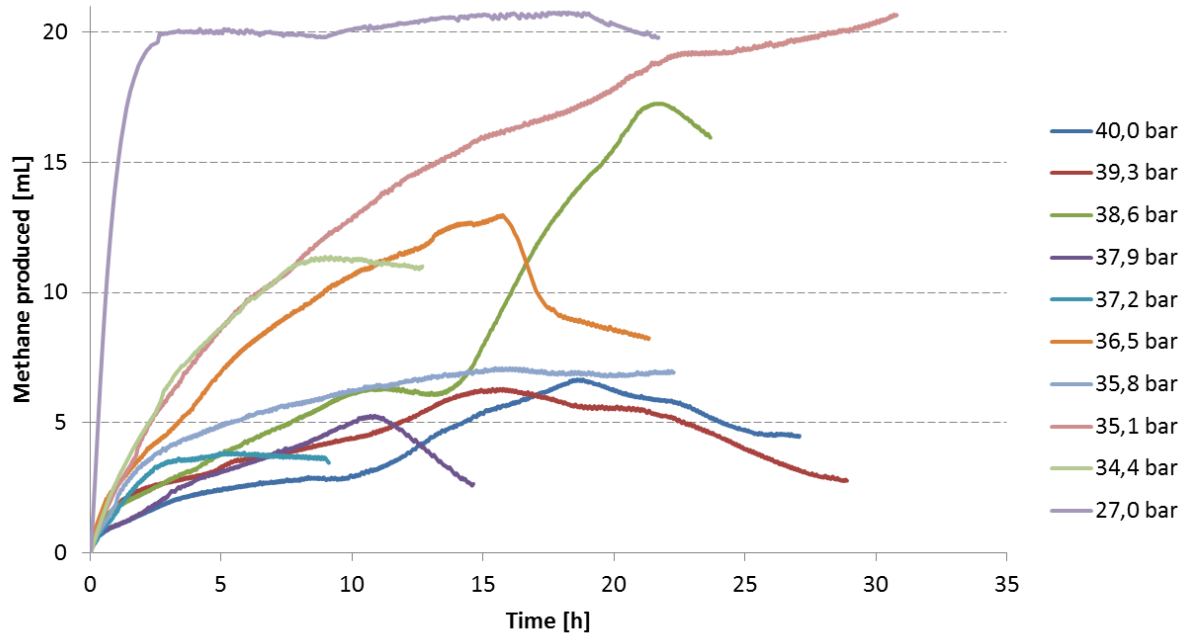
Figure 4.3.2b: Received methane volume for every pressure step conducted on core DEP_8. Note that each volume-graph denotes received volume at constant pressure, i.e. the volume change associated with reducing the pressure is not shown. Temperature was maintained at 2.8 °C and hydrate saturation prior to pressure depletion was 0.49.

Further insight to how hydrate dissociation takes place can be obtained by looking at when the methane gas is liberated. Figure 4.3.2c displays methane recovery for each pressure step for three cores depressurized at around 4 °C. X-axis shows how much pressure is reduced below the experimental observed dissociation pressure. The sum of all recoveries for each core equals the recovery values reported in Table 4.3.2. Every experiment has a peak in methane recovery when pressure is held 5-8 bar below the dissociation pressure. This could be explained by stronger driving forces as the pressure is decreased below dissociation pressure. Heat conductivity will be important and Lee *et al*. (2010a) observed fastest recovery by low driving forces, as rapid dissociation led to reformation of hydrates and clogging of core. For the stepwise depressurization technique utilized in this thesis, it is interesting to observe different methane recoveries for different pressure steps. A decreasing brine salinity during dissociation may explain why dissociation takes place over a range of pressure values, but it cannot explain why methane recovery peaks after 8-11 pressure steps. The impact of time is decisive and the initial pressure steps would produce more methane if they were held at constant pressure for more than around 24 hours. The experiments show that for a given amount of time and if the heat conductivity is good, methane recovery will be fastest when pressure is reduced well below dissociation pressure. There are some differences between experiments in the final stage of production. For example, core HR_57 experiences a methane recovery below 0.02 when pressure is reduced more than 7 bar below dissociation pressure. Experiment DEP_12 has a methane recovery around 0.07 when pressure is reduced more than 8 bar below dissociation pressure, indicating that a larger degree of hydrates have melted at a lower relative pressure compared with HR_57. This shows that more or less identical experiments with similar cores, hydrate saturations, temperatures and depressurization schemes, will respond different in a production scenario. Important parameters not investigated in these depressurization experiments are hydrate distribution and connectivity of phases. Released gas during initial dissociation may not be able to

create a continues phase and will not be produced in the pump until enough hydrates have melted to allow for a continues gas phase.
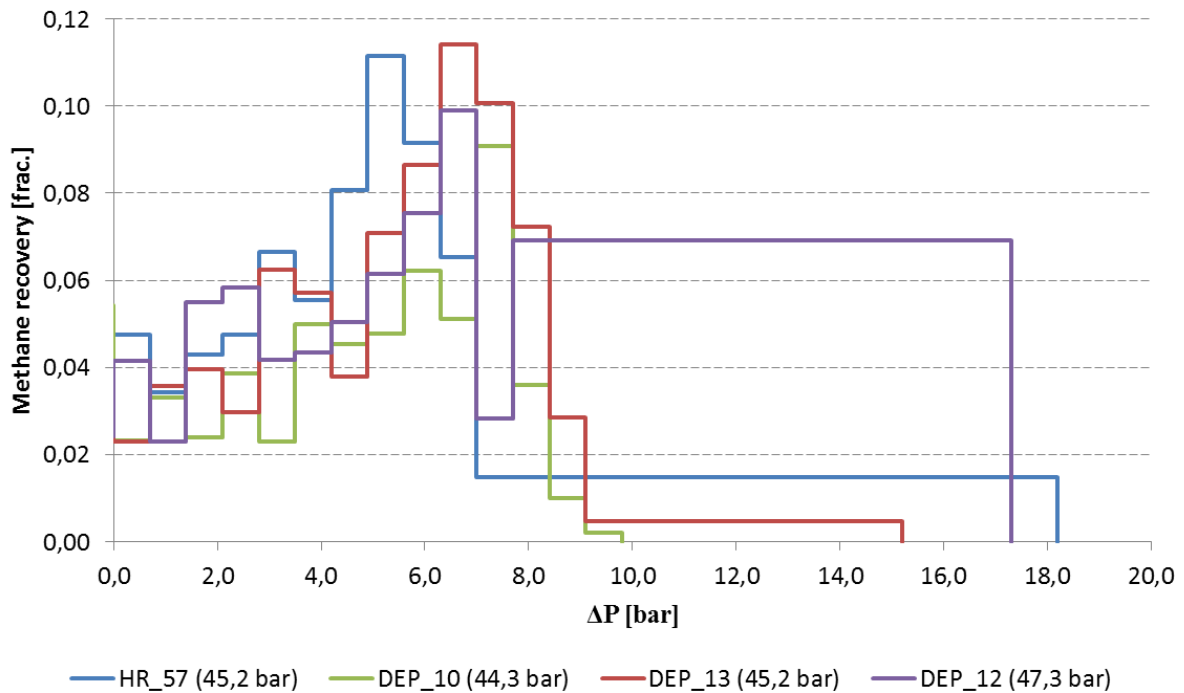
Figure 4.3.2c: Methane recovery from hydrates as a function of change in pressure. X-axis denotes pressure difference from observed dissociation pressure. Temperature was held at 4 °C and measured dissociation pressure is denoted in parentheses in the legend.

The three following figures display differential pressure at the first pressure steps for three different cores. Figure 4.3.2d presents differential pressure for experiment DEP_12. Pressure was reduced from both ends down to 48.0 bar and held at constant pressure for one day. Further reduction in pressure was operated from inlet side of core and hydrate dissociation initiated at the next pressure step down to 47.3 bar. The permeability of the hydrate saturated core was good and no differential pressure was observed. In experiment DEP_9, depicted in Figure 4.3.2e, the pressure was reduced from both ends down to 44.3 bar. Further reduction in pressure was operated from inlet side of core and an immediate differential pressure arose after the first pressure step. The differential pressure dropped to zero when pressure was reduced from 38.7 to 38.0 bar and hydrate dissociation started at 38.0 bar. Figure 4.3.2f shows differential pressure corresponding to the pressure step when hydrate started to dissociate for core DEP_10. Pressure was reduced from both ends down to 45.0 bar and the next pressure reduction from inlet led to an immediate differential pressure. Although inlet pressure was held at 44.3 bar, an initial pressure increase is observed as hydrates started to dissociate. The pump needed some time to adjust the pressure and compensate for liberated methane gas. Differential pressure was reduced to zero as hydrates dissociated and permeability was resumed.

Figure 4.3.2d: Initial pressure reduction for experiment DEP_12. Hydrate saturation prior to pressure depletion was 0.56 and temperature was maintained at 4.0 °C. Pressure decline down to 48.0 bar was operated from both ends; further reduction in pressure was conducted from inlet side of core.
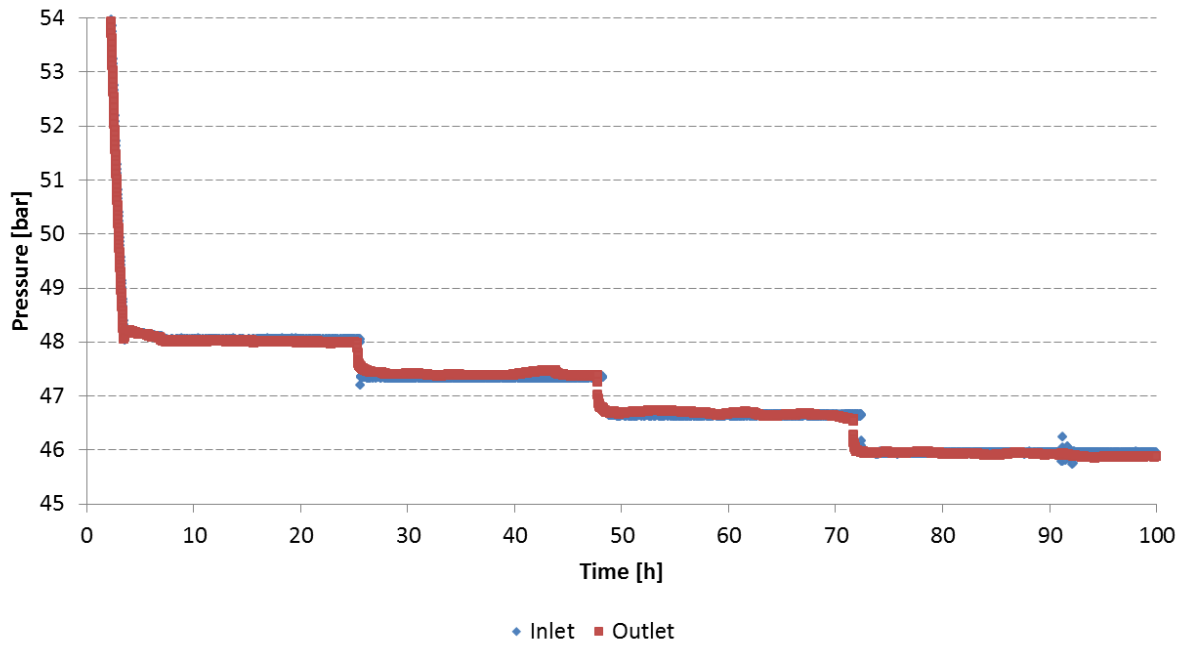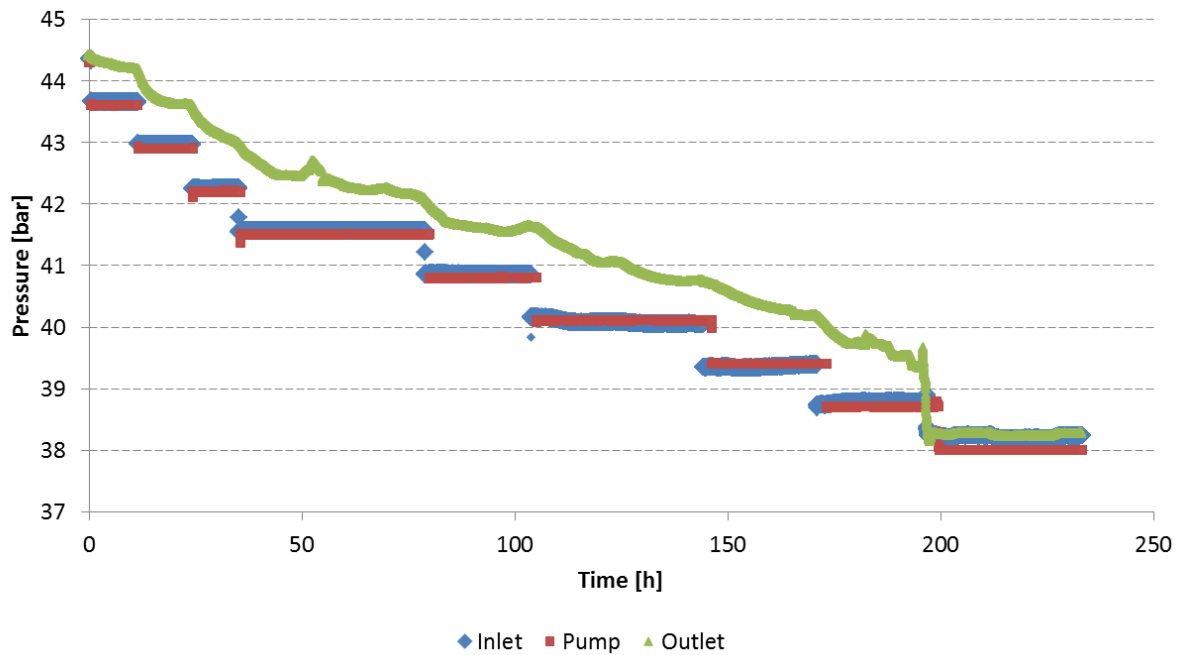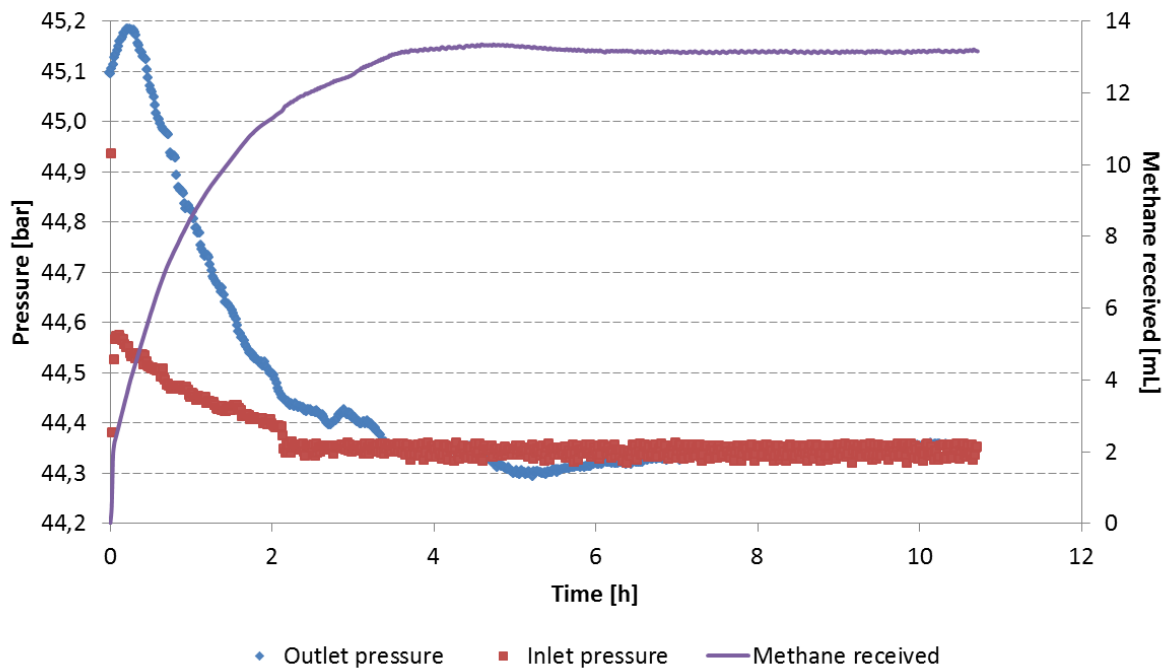

Figure 4.3.2e: Initial pressure reduction for experiment DEP_9. Hydrate saturation prior to pressure depletion was 0.67 and temperature was maintained at -0.4 °C. Pressure decline down to 44.3 bar was operated from both ends; further reduction in pressure was conducted from inlet side of core.

Figure 4.3.2f: Pressure step which resulted in initial hydrate dissociation in core DEP_10. Hydrate saturation prior to pressure depletion was 0.52 and temperature was maintained at 3.6 °C. Pressure decline down to 45.0 bar was operated from both ends; further reduction in pressure was conducted from inlet side of core.

The figures above illustrate the low permeability of the hydrate-filled cores and that the hydrate saturations are sufficiently high to sustain low differential pressures until dissociation is initiated. Some of the cores were tested to explore the magnitude of differential pressure which was needed to obtain flow. In experiment DEP_13, the pressure was reduced from 83 bar to 66 bar from inlet side, and outlet pressure was surveilled while keeping inlet pressure at 66 bar. As can be seen from Figure 4.3.2g, differential pressure drops towards zero indicating that a pressure difference of 17 bar is enough to induce flow. Experiment HR_57 was exposed to a lower pressure reduction from 83 bar down to 70 bar at inlet side, and now there was no sign of alterations in the outlet pressure. Inlet pressure was further decreased down to 60 bar, and soon after the outlet pressure dropped quickly and attained the same value, see Figure 4.3.2h. Exactly the same scheme was completed for experiment HR_58 and is displayed in Figure 4.3.2i. In this case differential pressure decreases towards zero at an inlet pressure of 70 bar, and further reduction of inlet pressure induces a temporarily differential pressure. Experiment HR_57 and HR_58, which had identical hydrate saturations and were subjected to the same pressure reduction scheme, are thus responding slightly different with respect to differential pressure. This is another sign pointing to a difference in hydrate distribution, as discussed in Section 4.1.4. However, these depressurization experiments alone cannot be used to unambiguously state that the cores had different flow properties; possible hydrate plugs located at end-pieces can lead to an erroneous assumption of a clogged core.
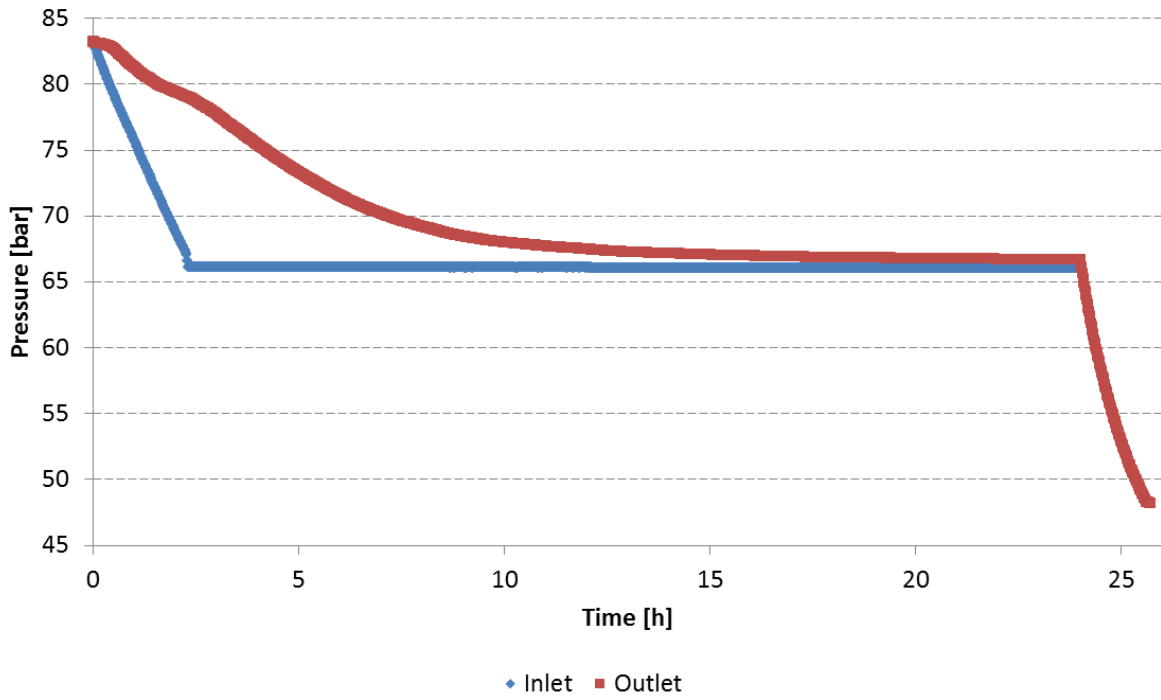
Figure 4.3.2g: Pressure response test for experiment DEP_13. Hydrate saturation prior to pressure depletion was 0.55 and temperature was maintained at 4.0 °C.
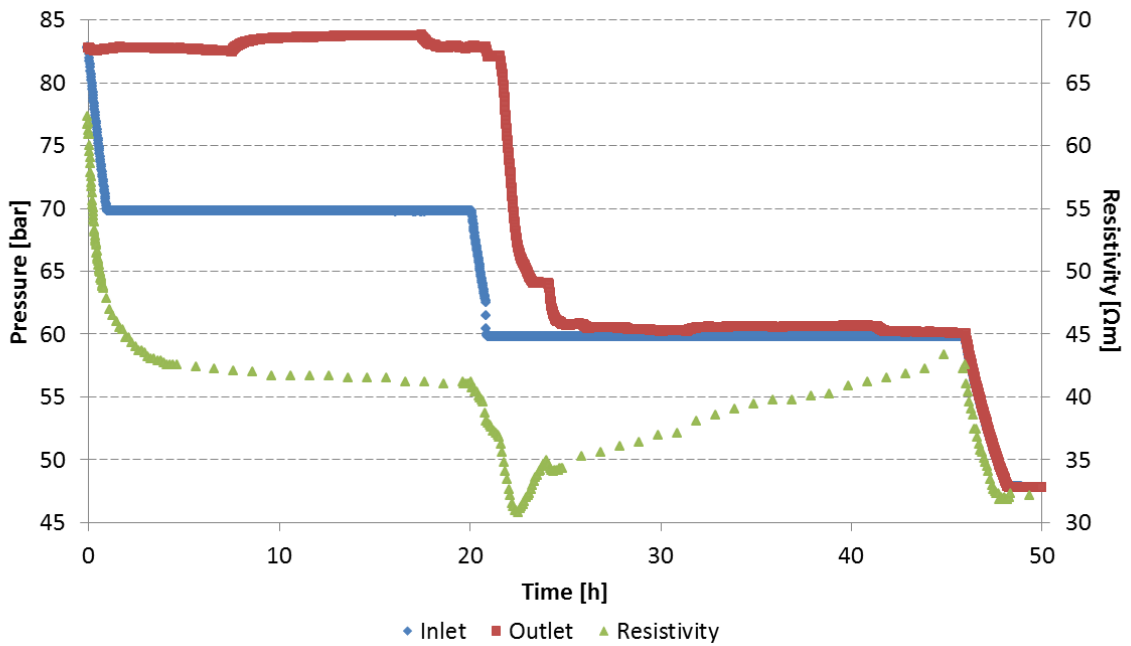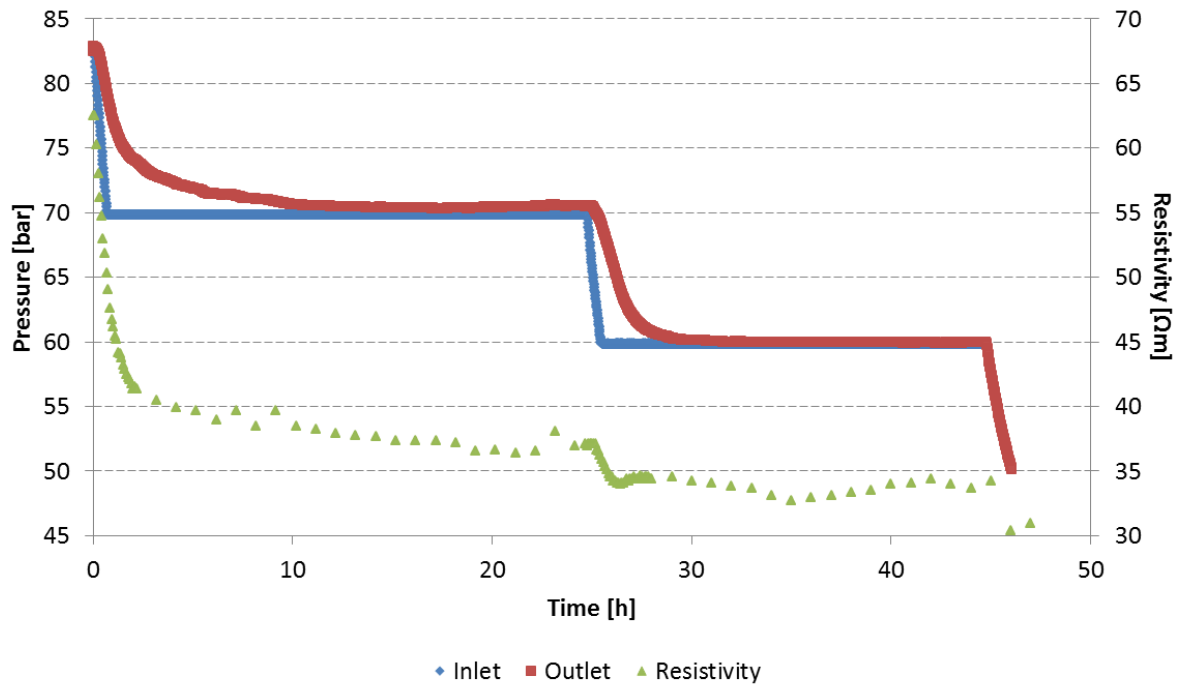

Figure 4.3.2h: Pressure response test for experiment HR_57 including resistivity measurements. Hydrate saturation prior to pressure depletion was 0.53 and temperature was maintained at 4.0 °C.

Figure 4.3.2i: Pressure response test for experiment HR_58 including resistivity measurements. Hydrate saturation prior to pressure depletion was 0.53 and temperature was maintained at 4.0 °C.

Both experiments HR_57 and HR_58 were complemented with resistivity measurements. The resistivity downswing following the initial pressure reduction is immense, and can be attributed to a relative increase in confinement pressure. As the pore pressure is lowered and confinement pressure is held at 110 bar, the floating end-piece will be pushed tighter against the core end and thereby decrease the resistivity. This is obviously a drawback with the relative simple resistivity measurement technique utilized in these experiments. An interesting difference between resistivity curves is the increase in resistivity when experiment HR_57 is held at 60 bar. Reformation of hydrates can be an explanation to this behavior. Xiong *et al*. (2012) observed formation of additional hydrates during initial pressure reduction, and justified the observation with a phenomenon known as the "Loricae effect" (Stern *et al*., 1996): Some of the water can be enclosed by hydrate and in that way be prevented from further growth as the supply of methane is limited. Initial pressure reduction leads to movement of phases and previously unavailable water can come in contact with methane gas creating potential for hydrate growth. Kneafsey *et al*. (2007) experienced a temperature increase upon initial pressure reduction, which also was attributed to the exothermic heat of additional hydrate formation.

Figure 4.3.2j shows resistivity values during the stepwise pressure reduction of core HR_57. Decline in resistivity is mainly because of continues increase in relative confinement pressure. The additional effect of a decreasing hydrate saturation after dissociation starts at 45.2 bar is not recognized on the resistivity graph. This means that it is not possible to differentiate between the contribution from hydrate dissociation and increasing relative confinement pressure. It would have been better to adjust the confinement pressure continuously for every pressure step. Best of all would be to conduct a more advanced resistivity measurement technique that is independent of confinement pressure. The resistivity values seem scattered in size, especially at the end, but this is mainly because of the compressed time-axis and the highly resolved y-axis. Figure 4.3.2k displays a fragment

of Figure 4.3.2j along with core inlet surface temperature and produced methane. The temperature variations are small and fluctuations in resistivity seem to be a result of instabilities related to flow in the core. After complete hydrate dissociation, the resistivity value stabilizes on 19-20 Ωm which is higher than the initial value of 9-10 Ωm. The same effect is observed for HR_58 and can be explained by a lower final water saturation compared with the initial water saturation. The pressure reduction scheme will probably retract some water from the core, especially during the initial pressure response test when differential pressures of 10-20 bar is applied. Loss of water before dissociation has started is even more crucial as this water is up-concentrated in salinity. Both final water saturation and salinity are expected to be lower than their original values, which yields a higher final resistivity.
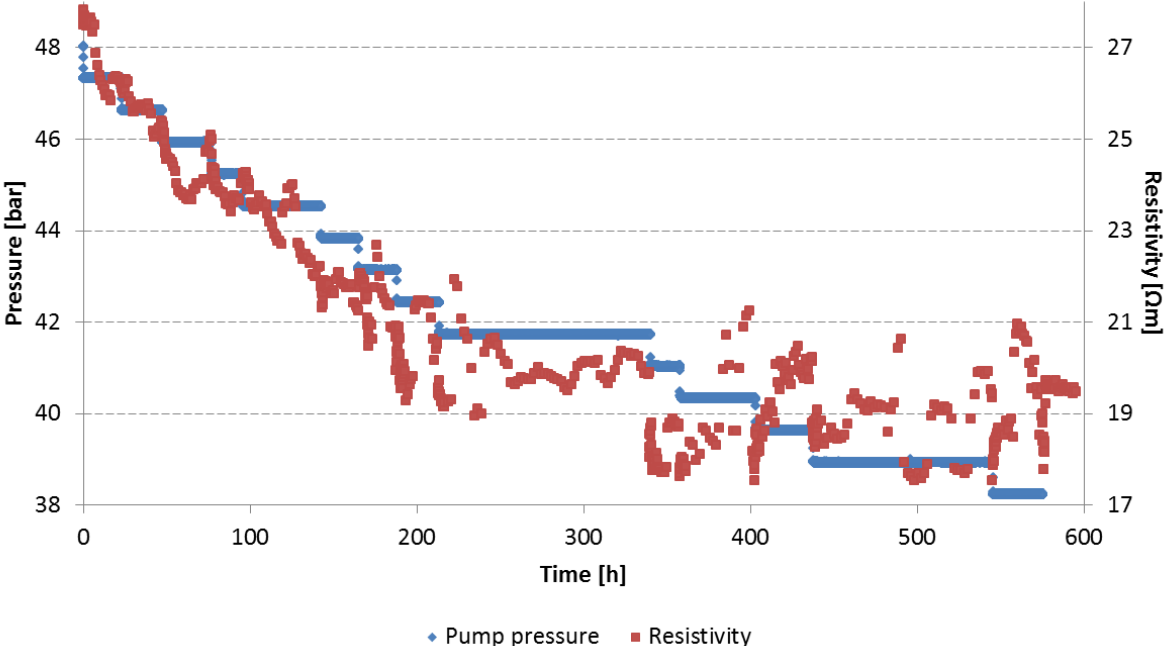
Figure 4.3.2j: Resistivity propagation during pressure reductions of 0.7 bar for HR_57. Confinement pressure is maintained at 80 bar and temperature is held at 4.0 °C. Start of hydrate dissociation is detected from the volume log at a pressure of 45.2 bar.
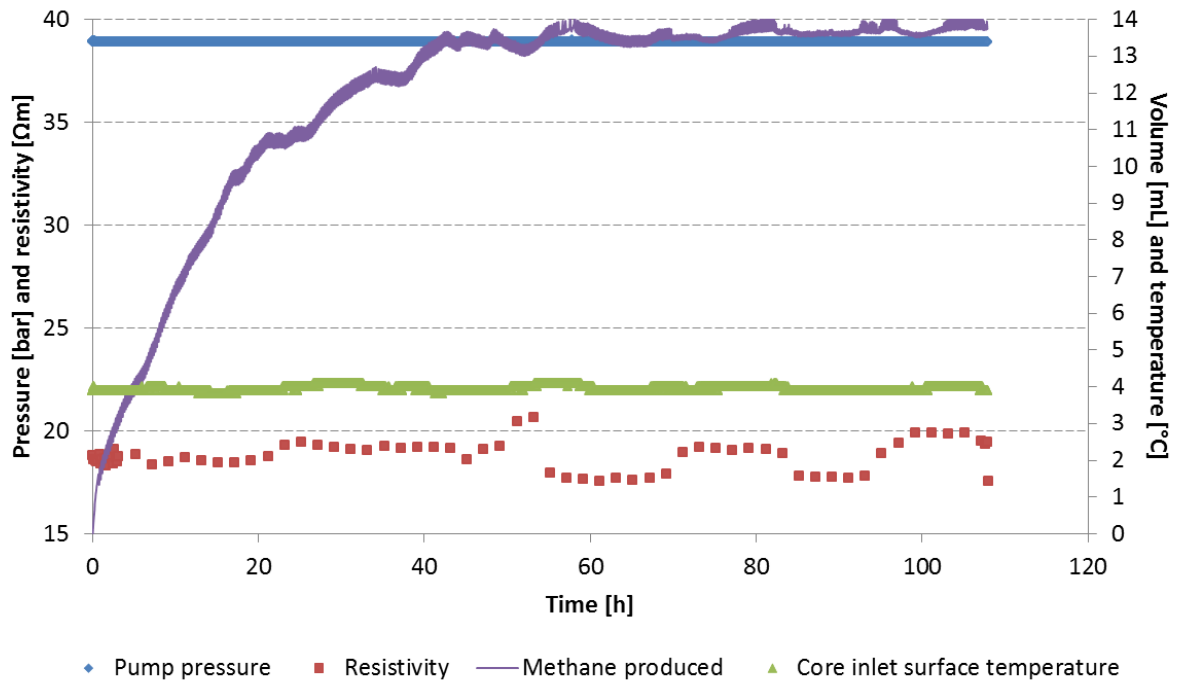
Figure 4.3.2k: Resistivity values at 38.9 bar along with temperature and produced volume of methane for HR_57.

4.4 MRI imaging

The imaging of cyclopentane hydrate dissociation conducted at the research department in Statoil was a first attempt to visualize hydrate dissociation in a newly installed MRI magnet. No cooling possibilities imposed dissociation induced by thermal stimulation as the hydrate saturated core was laid in room temperature during imaging. The dissociation time was not known in advance and the MRI magnet was set to obtain images every second hour. This imaging frequency turned out to be too low and all hydrates dissociated within the first two hours. Figure 4.4 displays images of the core in a time sequence of four hours. The first image, leftmost on Figure 4.4, is obtained immediately after the hydrate saturated core is placed inside the MRI magnet. Almost no signal indicates a successful hydrate formation since hydrogen atoms situated in the framework of hydrates have fast relaxation times which are not detected. The two other images are nearly identical since hydrate dissociation was completed within two hours, and the good signal quality stems from hydrogen atoms belonging to liberated water. The vertical white bars on the images obtained after dissociation are assumed to be signal coming from condensed water situated on the surface of the bubble wrap.

Time: 0 hour   Time: 2 hours   Time: 4 hours
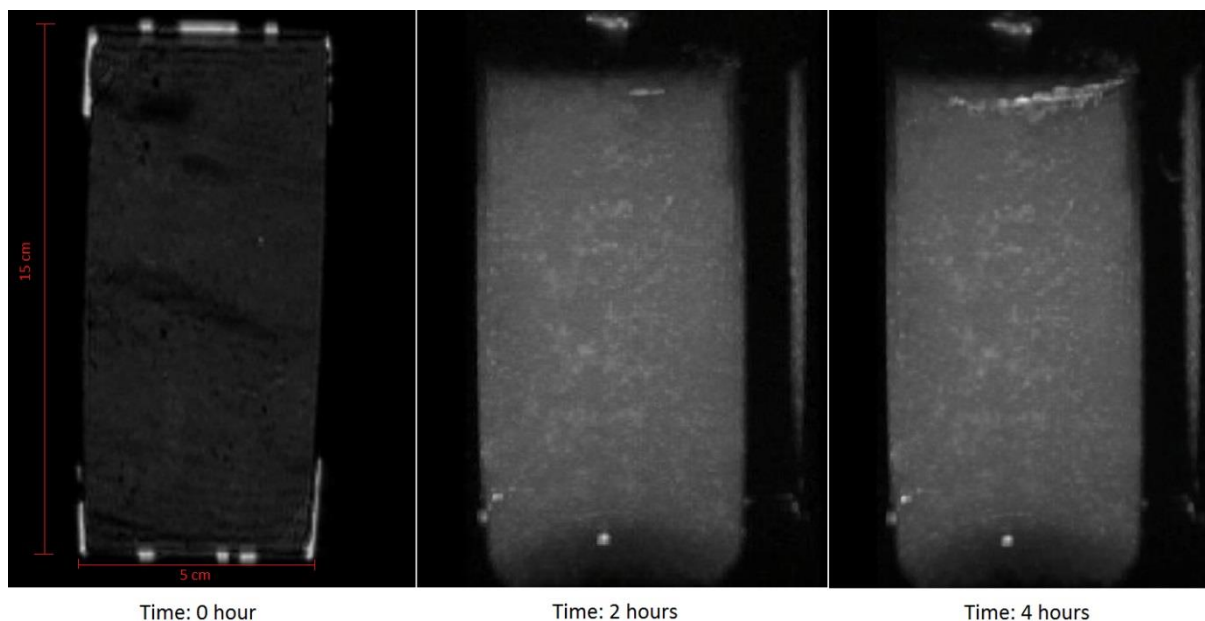
Figure 4.4: Sequence of images obtained from MRI showing a sandstone core filled with cyclopentane hydrates to the left. Hydrate dissociation was completed within two hours after the imaging sequence started and the image in the middle and to the right display the core saturated with brine and liquid cyclopentane.

The images shown above have no scientific value in themselves but present a first step in testing of the new MRI instrument. All of the experiments conducted as part of this thesis would benefit from obtaining *in situ* images during hydrate formation, CH_4-CO_2 exchange and depressurization. The MRI instrument may in future provide knowledge on water and hydrate distribution during formation and on flow properties during CH_4-CO_2 exchange and depressurization experiments.

4.5 Uncertainties

This chapter will deal with uncertainties and evaluate the contribution from both equipment uncertainties and errors resulting from experimental conditions. The known uncertainties in equipment used in this work are presented in Table 4.5a.

Table 4.5a: Equipment uncertainties specified by manufacturers

Equipment	Parameter	Uncertainty	Unit
Slide caliper	Length	0.01	cm
GF-3000 Digital Balance	Weight	0.02	g
ST Stigma 1000 and 500	Pressure	0.1	%
	Flow	0.1	%
HH506RA Thermometer	Temperature	0.1	°C

In addition to these instruments, there will be equipment uncertainties in the gas chromatograph, mass flow meter, pressure transducers and resistance logging device which are not available. The overall effect of equipment uncertainties is limited compared to experimental uncertainties and

assumptions made during calculations. This can be shown by an example, where the uncertainties related to geometric parameters of core CO2_33 are computed and used to calculate the uncertainty in initial water saturation. Uncertainties in composite values R are calculated from the following equation:

$$\sigma_R = \sqrt{\left(\frac{\delta R}{\delta x_1}\ \sigma_{x_1}\right)^2 + \cdots + \left(\frac{\delta R}{\delta x_n}\ \sigma_{x_n}\right)^2}$$ (4.5a)

where the standard deviations σ have been replaced with known or proposed uncertainties. If R is composed of a sum of variables: R = ax + by, Eq. 4.5a is easily simplified to:

$$\delta R = \sqrt{(a\delta x)^2 + (b\delta y)^2}$$ (4.5b)

If R is composed of a product of variables: R = $ax^n y^m$, Eq. 4.5a can be simplified to:

$$\delta R = R\sqrt{\left(n\frac{\delta x}{x}\right)^2 + \left(m\frac{\delta y}{y}\right)^2}$$ (4.5c)

Table 4.5b presents volumetric uncertainties for CO2_33 and they are based on Eqs. 4.5b and 4.5c along with equipment uncertainties found in Table 4.5a. The uncertainty in matrix density is not known and is not included in pore volume and porosity calculations. The uncertainty in brine density is omitted in the expression for initial water saturation.

Table 4.5b: Calculated uncertainties in initial parameters for experiment CO2_33

Parameter	Value	Uncertainty	Unit
Bulk volume	298	±1	mL
Pore volume	70	±1	mL
Porosity	0.234	±0.004	frac.
Initial water saturation	0.69	±0.01	frac.
Salinity	3.50	±0.01	wt%

The uncertainty in initial water saturation is ±0.01 [frac.] based on equipment uncertainties. The calculation of initial water saturation is based on the amount of water which has imbibed into the core, and some of the water will be located on the surface of the core and thereby influent the weight of the saturated core. Some of the water will also trickle down on the digital balance. If the amount of imbibed water is miss-quantified by one gram, it will lead to an offset of 0.015 [frac.] in water saturation for experiment CO2_33. This illustrates the importance of accuracy in experimental proceedings and the uncertainties in initial water saturations are expected to be ±0.02 [frac.]. The uncertainty in final hydrate saturation can be calculated by applying Eq. 4.5c to Eq. 1.4.1a. The uncertainty in methane volume is given by the pump uncertainty from Table 4.5a, and the value and uncertainty of the hydration number is given in Section 1.1.4. Methane density will vary with temperature, and although the equipment uncertainty of the thermometers is listed as ±0.1 °C,

observed temperature variations on the core surface resulting from different day and night temperatures have been quantified to ±0.3 °C. Temperature fluctuations in the pumps exposed to room temperature have been estimated to ±1 °C. The outcome of the calculations for experiment CO2_33 is an uncertainty in hydrate saturation of ±0.01 [frac.]. In this case there will also be experimental errors leading to an additional uncertainty in hydrate saturation. Leakages are accounted for by obtaining the leakage rate prior to hydrate formation and at the end of formation. The leakage rate is assumed to be constant in-between. A more pressing source of error is potential hydrate formation at the end-pieces and in tubings leading to the core, which will affect the amount of consumed methane. The overall effect on the uncertainty in hydrate saturation is difficult to quantify, but an estimate of ±0.02 [frac.] seems realistic.

The temperature variations will have a big impact on dissociation pressure, as a difference in core temperature from 4.0 °C to 4.3 °C results in a shift in theoretical dissociation pressure from 45.0 bar to 46.4 bar (calculated by CSMGem). The stepwise pressure reduction scheme utilized in this work is not a sensitive approach, and the uncertainty in the experimentally found hydrate dissociation pressures is at least ±1.4 bar. The biggest error of concern for the CH_4-CO_2 exchange experiment is leakages at the production lines and valves, which will dominate over equipment uncertainties in the gas chromatograph and mass flow meter. A leakage rate during production is not estimated and this rate will be dynamic and depend on the composition of the effluent. Leakages will lead to an underestimation of methane recovery and has been commented in Section 4.2. The equipment uncertainty in the LCR-meter conducting the resistance measurements is unavailable, but temperature variations and changes in relative confinement pressure will likely dominate over the equipment uncertainty. The resistivity readings are only used to display a trend during hydrate formation and pressure reduction, and calculated water saturations based on resistivity values are in good agreement with PVT-calculated water saturations.

The essence of this chapter is to present an overview of uncertainties related to values presented in this thesis, and to show the difficulty with determining the combined effect of equipment uncertainties and experimental uncertainties. The integrity of the results obtained by the hydrate research group is based on repetitive experiments which yield trends that to a small degree are influenced by uncertainties related to individual experiments.

5 Conclusions and Future Work

5.1 Conclusions

- Fifteen hydrate formations were successfully conducted in sandstone cores, supplementing previous research performed by the hydrate research group at the Department of Physics and Technology.
- Hydrate formations conducted with temperatures varying between 0-4 °C indicated insignificant changes in hydrate growth rate with temperature. The final hydrate saturation seemed to be elevated for formation temperatures less than approximately 1 °C.
- A binary mixture of 60% N_2 and 40% CO_2 [mole percent] was injected into one hydrate-filled core and methane gas was recovered. The initial rate of methane recovery from hydrates was high with a rapid decline.
- Pure nitrogen gas was unable to obtain flow in two hydrate-bearing cores with excess water.
- Hydrate dissociation was observed to occur gradually when pressure depleting cores stepwise from one end. Hydrate dissociation was found to start slightly above theoretical dissociation pressures.
- A first attempt of visualizing hydrate dissociation was successfully conducted with a newly installed MRI instrument.

5.2 Future work

It should be conducted more experiments on CH_4-CO_2 exchange in sandstone cores with high initial water saturations to investigate the effect of excess water on methane recovery. The fraction of injected nitrogen should be varied in order to maximize methane recovery, maintain injectivity and maximize CO_2 sequestration. Implementation of flow loops connected to end-pieces is suggested. This will enable the possibility for injection of gases/liquids and identify whether hydrate is blocking flow in the core or in the flow line. The experimental design of the MRI instrument should be further improved to allow for research on methane hydrates; a core holder with cooling jacket should be implemented to enable conditions of high pressures and low temperatures.

Nomenclature

n_w	Hydration number	-
ΔG	Gibbs free energy	[J]
r	Radius, Resistance	[m], [Ω]
Υ	Interfacial free energy	[J/m^2]
ρ^H_N	Molecular density	[mole/m^3]
$\Delta g^{phase\ trans.}$	intensive change in Gibbs free energy	[J/mole]
μ_w	Chemical potential of water	[J/mole]
v_i	Fraction of cavity type i per water molecule	-
h_{ij}	Cavity partitioning function for guest molecule type j in cavity i	-
c_{ij}	Langmuir constant	-
f^H_j	Fugacity of guest molecule type j in the hydrate phase	-
R	Gas constant	[J/mole*K]
T	Temperature	[K] or [°C]
x_w	Mole fraction of water	[frac.]
Υ_w	Activity coefficient of water	-
R	Electrical resistivity	[Ωm]
A	Cross-sectional area	[m²]
L	Length	[m]
$|Z|$	Absolute value of electrical impedance	[Ω]
ϑ	Electrical phase angle	[radian]
F	Formation factor	[frac.]
R_o	Resistivity of completely brine saturated formation	[Ωm]
R_w	Resistivity of the brine	[Ωm]
a	Proportionality constant in *Archies 1. law*	-
ϕ	Porosity	[frac.]
m	Cementation constant	-
I	Resistivity index	[frac.]
R_t	Resistivity of formation filled with water and hydrocarbons	[Ωm]
b	Proportionality constant in *Archies 2. law*	-
S_w	Water saturation	[frac.]
n	Saturation constant, number of components	-
V	Volume	[mL]
ρ	Density	[g/mL]
Mm	Molar mass	[g/mole]
n_w^H	Amount of water entering the hydrate	[mole]
C	Salt concentration	[wt%]
τ	Number of variables that must be defined in order to reach equilibrium	-
π	Number of phases	-
S_{wi}	Initial water saturation	[frac.]

S_{wf}	Final water saturation	[frac.]
S_H	Hydrate saturation	[frac.]
σ	Standard deviation	-
δR	Uncertainty in composite value R	-

Abbreviations

Frac.	Fraction
Wt%	Weight percent
Kcal	Kilocalorie
Ice Ih	Hexagonal ice
Å	Ångstrøm
Gt C	Gigatons of carbon
BSR	Bottom simulating reflector
GHSZ	Gas hydrate stability zone
GHOZ	Gas hydrate occurrence zone
HBL	Hydrate-bearing layer
Tcf	Trillion cubic feet
M-cage	Large cavity
S-cage	Small cavity
Cu m	Cubic meter
Bcf	Billion cubic feet
ESP pump	Electric submersible pump
Mscf	Million standard cubic feet
MRI	Magnetic resonance imaging
DC	Direct current
AC	Alternating current
CSMGem	Colorado School of Mines Gibbs free energy minimization
BPR	Backpressure regulator
GC	Gas chromatograph
MFM	Mass flow meter
LCR	Inductance, capacitance, resistance
PVT	Pressure, volume, temperature

References

Ahlbrandt, T. S., 2002. Future petroleum energy resources of the world. *International Geology Review,* 44(12), pp. 1092-1104.

Allred, A. L., 1961. ELECTRONEGATIVITY VALUES FROM THERMOCHEMICAL DATA. *Journal of Inorganic and Nuclear Chemistry,* 17(3-4), pp. 215-221.

Anderson, G., 2008. *Marine Science.* [Online]
Available at: http://www.marinebio.net/marinescience/02ocean/swcomposition.htm
[Accessed 4 December 2014].

Anderson, G. K., 2004. Enthalpy of dissociation and hydration number of methane hydrate from the Clapeyron equation. *Journal of Chemical Thermodynamics,* Volume 36, pp. 1119-1127.

Archie, G., 1942. The Electrical Resistivity Log as an Aid in Determining Some Reservoir Characteristics. *Transactions of the AIME,* 146(1), pp. 54-62.

Atkins, P. and De Paula, J., 2010. Atkins' Physical Chemistry. In: Oxford: Oxford University Press, p. 191.

Baldwin, B. A., Stevens, J., Howard, J., Graue, A., Kvamme, B., Aspenes, E., Ersland, G., Husebø, J., Zornes, D., 2009. Using magnetic resonance imaging to monitor CH4 hydrate formation and spontaneous conversion of CH4 hydrate to CO2 hydrate in porous media. *Magnetic Resonance Imaging,* 27(5), pp. 720-726.

Birkedal, K. A., Ersland, G., Hauge, L.P., Graue, A., Hester, K., Stevens, J. and Howard, J., 2011. *ELECTRICAL RESISTIVITY MEASURMENTS OF CH4 HYDRATE-BEARING SANDSTONE DURING FORMATION.* Edinburgh, Proceedings of the 7th International Conference on Gas Hydrates.

Boswell, R. and Collett, T., 2006. The Gas Hydrates Resource Pyramid. *Fire in the Ice (The National Energy Technology Laboratory Methane Hydrate Newsletter)*, Fall, pp. 5-7.

Bryn, P., Berg, K., Forsberg, C.F., Solheim, A. and Kvalstad, T.J., 2005. Explaining the Storegga Slide. *Marine and Petroleum Geology,* 22(1-2), pp. 11-19.

Chaplin, M., 2014. *WATER STRUCTURE AND SCIENCE.* [Online]
Available at: http://www1.lsbu.ac.uk/water/water_molecule.html
[Accessed 13 October 2014].

Circone, S., Kirby, S. H. and Stern, L. A., 2005. Direct Measurement of Methane Hydrate Composition along the Hydrate Equilibrium Boundary. *The Journal of Physical Chemistry B,* 109(19), pp. 9468-9475.

Collett, T., 2008. *Geology of Marine Gas Hydrates and Their Global Distribution.* Houston, Offshore Technology Conference.

Colorado School of Mines, 2009. *Center for Hydrate Research.* [Online]
Available at: http://hydrates.mines.edu/CHR/Software.html
[Accessed 4 February 2015].

Conn, J., 2012. *Clear Biology.* [Online]
Available at: http://www.clearbiology.com/water-molecule-worksheet/
[Accessed 27 October 2014].

Duan, Z. and Mao, S., 2006. A thermodynamic model for calculating methane solubility, density and gas phase composition of methane-bearing aqueous fluids from 273 to 523 K and from 1 to 2000 bar. *Geochimica et Cosmochimica Acta,* Volume 70, pp. 3369-3386.

Durham, W., Kirby, S., Stern, L. and Zhang, W., 2003. The strength and rheology of methane clathrate hydrate. *Journal of Geophysical Research,* 108(B4), pp. 1-11.

Environmental Protection Agency US, 2013. *Clean Energy.* [Online]
Available at: http://www.epa.gov/cleanenergy/energy-and-you/affect/natural-gas.html
[Accessed 18 December 2014].

Ersland, G., Birkedal, K. A. and Graue, A., 2009. *MRI characterization of hydrate growth pattern and production scenarios in sandstone.* Moscow, Conference in Gubkin Russian State University of Oil and Gas.

Ersland, G., Husebø, J., Graue, A., Baldwin, B., Howard, J. and Stevens, J., 2010. Measuring gas hydrate formation and exchange with CO2 in Bentheim sandstone using MRI tomography. *Chemical Engineering Journal,* 158(1), pp. 25-31.

Finney, J., 2006. *London Centre for Nanotechnology.* [Online]
Available at: http://www.london-nano.com/research-and-facilities/highlight/new-forms-of-ice
[Accessed 28 October 2014].

Graue, A., Kvamme, B., Baldwin, B., Stevens, J., Howard, J., Aspenes, E., Ersland, G., Husebø, J. and Zornes, D., 2008. MRI Visualization of Spontaneous Methane Production From Hydrates in Sandstone Core Plugs When Exposed to CO2. *SPE Journal,* 13(2), pp. 146-152.

Grover, T., Moridis, G. and Holditch, S. A., 2008. *Analysis of reservoir performance of Messoyakha Gas hydrate Field.* Vancouver, The International Society of Offshore and Polar Engineers.

Hågenvik, C., 2013. *CO2 Injection in Hydrate Bearing Sandstone with Excess Water.* Bergen: Master Thesis, University of Bergen.

Haligva, C., Linga, P., Ripmeester, J. and Englezos, P., 2010. Recovery of Methane from a Variable-Volume Bed of Silica Sand/Hydrate by Depressurization. *Energy and Fuels,* Volume 24, pp. 2947-2955.

Hauge, L.P., Birkedal, K., Ersland, G. and Graue, A., 2012. *Effects of Initial Saturation and Salinity on Methane Hydrate Growth in Sandstone.* San Francisco, Poster at American Geophysical Union.

Hauge, L. P. Ø., 2011. *Resistivity Measurements during Gas Hydrate Formation and Subsequent CO2 Exchange in Porous Sandstone.* Bergen: Master Thesis, University of Bergen.

Hauge, L. P. Ø., 2013. *In-house database.* Bergen: University of Bergen.

Haymet, A. and Barlow, T., 2006. Nucleation of Supercooled Liquids. *Annals of the New York Academy of Sciences,* 715(1), pp. 549-551.

Hester, K. C. and Brewer, P. G., 2009. Clathrate Hydrates in Nature. *Annual Review of Marine Science,* Volume 1, pp. 303-327.

Hossainpour, R., 2013. *Catalysts for Enhanced CO2-CH4 Exchange in Natural Gas Hydrates – An experimental feasibility study of exchange enhancement by use of chemical additives.* Bergen: Master Thesis, University of Bergen.

Husebø, J., 2008. *Monitoring depressurization and CO2-CH4 exchange production scenarios for natural gas hydrates.* Bergen: PhD Thesis, University of Bergen.

Husebø, J., Ersland, G., Graue, A. and Kvamme, B., 2009. Effects of salinity on hydrate stability and implications for storage of CO2 in natural gas hydrate reservoirs. *Energy Procedia,* 1(1), pp. 3731-3738.

International Energy Agency, 2014. *World Energy Outlook 2014, Executive Summary.* [Online]
Available at:
http://www.iea.org/publications/freepublications/publication/WEO_2014_ES_English_WEB.pdf
[Accessed 23 March 2015].

IPCC, 2014. *CLIMATE CHANGE 2014 Synthesis Report; Summary for Policymakers.* Geneva: Intergovernmental Panel on Climate Change.

Jeffrey, G. and McMullan, R., 1967. The Clathrate Hydrates. *Progress in Inorganic Chemistry,* Volume 8, pp. 43-108.

Jung, J., Espinoza, D. and Santamarina, J., 2010. Properties and phenomena relevant to CH4-CO2 replacement in hydrate-bearing sediments. *Journal of Geophysical Research,* Volume 115, pp. 1-16.

Kang, H., Koh, D., Kim, D., Park, J., Cha, M. and Lee, H., 2012. *Recovery of Methane Intercalated in Natural Gas Hydrate Sediments Using a Carbon Dioxide and Flue Gas Mixture.* Rhodes, Greece, Proceedings of the Twenty-second International Offshore and Polar Engineering Conference.

Kleinberg, R.L., Flaum, C., Griffin, D.D., Brewer, P.G., Malby, G.E., Peltzer, E.T. and Yesinowski, J.P., 2003. Deep sea NMR: Methane hydrate growth habit in porous media and its relationship to hydraulic permeability, deposit accumulation, and submarine slope stability. *Journal of geophysical research,* Volume 108, pp. 1-17.

Kneafsey, T., Tomutsa, L., Moridis, G., Seol, Y., Freifeld, B., Taylor, C. and Gupta, A., 2007. Methane hydrate formation and dissociation in a partially saturated core-scale sand sample. *Journal of Petroleum Science and Engineering,* 56(1-3), pp. 108-126.

Kvamme, B., 2014. *RE: PTEK232: Fundamentals of Natural Gas Hydrates and Practical Implications.* Bergen: University of Bergen.

Kvamme, B., 2015. Feasibility of simultaneous CO2 storage and CH4 production from natural gas hydrate using mixtures of CO2 and N2. *Canadian Journal of Chemistry,* pp. 1-11.

Kvamme, B., Graue, A., Buanes, T., Kuznetsova, T. and Ersland, G., 2007. Storage of CO2 in natural gas hydrate reservoirs and the effect of hydrate as an extra sealing in cold aquifers. *International Journal of Greenhouse Gas Control,* 1(2), pp. 236-246.

Kvenvolden, K. A., 1988. Methane hydrate - A major reservoir of carbon in the shallow geosphere?. *Chemical Geology,* 71(1-3), pp. 41-51.

Kvenvolden, K. A., 1993. Gas hydrates - geological perspective and global change. *Reviews of Geophysics,* 31(2), pp. 173-187.

Kvenvolden, K. A., 2002. Methane hydrate in the global organic carbon cycle. *Terra Nova,* 14(5), pp. 302-306.

Lee, H., Seo, Y., Seo, Y.T., Moudrakovski, I.L. and Ripmeester, J.A., 2003. Recovering Methane from Solid Methane Hydrate with Carbon Dioxide. *Angewandte Chemie International Edition,* 42(41), pp. 5048-5051.

Lee, J., Park, S. and Sung, W., 2010a. An experimental study on the productivity of dissociated gas from gas hydrate by depressurization scheme. *Energy Conversion and Management,* 51(12), pp. 2510-2515.

Lee, J., Santamarina, J. and Ruppel, C., 2010b. Volume change associated with formation and dissociation of hydrate in sediment. *Geochemistry Geophysics Geosystems, AN ELECTRONIC JOURNAL OF THE EARTH SCIENCES,* 11(3), pp. 1-13.

Lien, J. R., 2004. *PTEK211 Grunnleggende reservoarfysikk (Kjerneanalyse og logging).* Bergen: Institutt for Fysikk og Teknologi, UiB.

Makogon, Y. F., 2009. Natural gas hydrates - A promising source of energy. *Journal of Natural Gas Science and Engineering,* 2(1), pp. 49-59.

Makogon, Y., Holditch, S. and Makogon, T., 2005. Russian field illustrates gas-hydrate production. *Oil and Gas Journal,* Volume 103, pp. 43-47.

McGrail, B., Zhu, T., Hunter, R., White, M., Patil, S. and Kulkarni, A., 2004. *A new method for enhanced production of gas hydrates with CO2.* Vancouver, AAPG HEDBERG CONFERENCE, "Gas Hydrates: Energy Resource Potential and Associated Geologic Hazards".

McGrail, B.P., Schaef, H.T., White, M.D., Zhu, T., Kulkami, A.S., Hunter, R.B., Patil, S.L., Owen, A.T. and Martin, P.F., 2007. *Using Carbon Dioxide to Enhance Recovery of Methane from Gas Hydrate Reservoirs: Final Summary Report,* U.S.: Pacific Northwest National Laboratory, U.S. Department of Energy.

Moridis, G. J., 2002. *Numerical Simulation Studies of Thermally-Induced Gas Production From Hydrate Accumulations With No Free Gas Zones at the Mallik Site, Mackenzie Delta, Canada.* Melbourne, SPE conference.

Moridis, G. J., Collett, T.S., Pooladi-Darvish, M., Hancock, S., Santamarina, C., Boswell, R., Kneafsey, T., Rutqvist, J., Kowalsky, M.B., Reagan, M.T., Sloan, E.D., Sum, A.K. and Koh, C.A., 2011. Challenges, Uncertainties, and Issues Facing Gas Production From Gas-Hydrate Deposits. *SPE Reservoir Evaluation and Engineering,* 14(1), pp. 76-104.

Moridis, G. J. and Collett, T. S., 2003. *Strategies for gas production from hydrate accumulations under various geological and reservoir conditions.* Berkeley, Lawrence Berkeley National Laboratory.

Moridis, G. J., Collett, T.S., Boswell, R., Kurihara, M., Reagan, M.T., Koh, C. and Sloan, E.D., 2009. Toward Production From Gas Hydrates: Current Status, Assessment of Resources, and Simulation-Based Evaluation of Technology and Potential. *SPE Reservoir Evaluation and Engineering,* 12(5), pp. 745-767.

Moridis, G. J. and Sloan, E. D., 2007. Gas production potential of disperse low-saturation hydrate accumulations in oceanic sediments. *Energy Conversion and Management,* 48(6), pp. 1834-1849.

Mork, M., 2002. *FORMATION RATE OF NATURAL GAS HYDRATE. Reactor Experiments and Models.* Trondheim: Doktor Ingeniør thesis, Norwegian University of Science and Technology.

Ohgaki, K., Takano, K. and Moritoki, M., 1994. Exploitation of CH4 Hydrates under the Nankai Trough in Combination with CO2 Storage. *Kagaku Kogaku Ronbunshu,* Volume 20, pp. 121-123.

Ohgaki, K., Takano, K., Sangawa, H., Matsubara, T. and Nakano, S., 1996. Methane Exploitation by Carbon Dioxide from Gas Hydrates - Phase Equilibria for CO2-CH4 Mixed Hydrate System. *Journal of Chemical Engineering Japan,* 29(3), pp. 478-483.

Ota, M., Morohashi, K., Abe, Y., Watanabe, M., Lee Smith, R. and Inomata, H., 2005. Replacement of CH4 in the hydrate by use of liquid CO2. *Energy Conversion and Management,* 46(11-12), pp. 1680-1691.

Park, Y., Cha, M., Cha, H., Shin, K., Lee, H., Park, K., Huh, D., Lee, H., Kim, S. and Lee, J., 2008. *Swapping carbon dioxide for complex gas hydrate structures.* Vancouver, Proceedings of the 6th International Conference on Gas Hydrates.

Pearson, C., Halleck, P., McGuire, P., Hermes, R. and Mathews, M., 1983. Natural Gas Hydrates Deposits: A Review of in Situ Properties. *The Journal of Physical Chemistry,* 87(21), pp. 4180-4185.

Ramstad, T., Idowu, N., Nardi, C. and Øren, P., 2012. Relative Permeability Calculations from Two-Phase Flow Simulations Directly on Digital Images of Porous Rocks. *Transport in Porous Media,* 94(2), pp. 487-504.

Ren, S., Liu, Y., Liu, Y. and Zhang, W., 2009. Acoustic velocity and electrical resistance of hydrate bearing sediments. *Journal of Petroleum Science and Engineering,* pp. 1-5.

Rodger, P. M., 2000. Methane Hydrate: Melting and Memory. *Annals of the New York Academy of Sciences,* Volume 912, pp. 474-482.

Ruppel, C., 2011. Methane Hydrates and the Future of Natural Gas. *MITEI Natural Gas Report, Supplementary Paper on Methane Hydrates*.

Rutqvist, J., Moridis, G., Grover, T. and Collett, T., 2009. Geomechanical response of permafrost-associated hydrate deposits to depressurization-induced gas production. *Journal of Petroleum Science and Engineering,* Volume 67, pp. 1-12.

Rutqvist, J. and Moridis, G. J., 2007. *Numerical Studies on the Geomechanical Stability of Hydrate-Bearing Sediments.* Houston, Offshore Technology Conference.

Schoderbek, D., Martin, K.L., Howard, J., Silpngarmlert, S. and Hester, K., 2012. *North Slope Hydrate Fieldtrial: CO2/CH4 Exchange.* Houston, Arctic Technology Conference.

Seo, Y.-T., Lee, H. and Yoon, J.-H., 2001. Hydrate Phase Equilibria of the Carbon Dioxide, Methane, and Water System. *Journal of Chemical and Engineering Data,* 46(2), pp. 381-384.

Sloan, E. D., 1998. *Clathrate Hydrates of Natural Gases.* 2nd ed. New York: Marcel dekker, Inc.

Sloan, E. D., 2003. Fundamental principles and applications of natural gas hydrates. *Nature,* Volume 426, pp. 353-363.

Sloan, E. and Koh, C., 2008. *Clathrate Hydrates of Natural Gases.* 3rd ed. Boca Raton, FL: CRC Press.

Spangenberg, E., 2001. Modeling of the influence of gas hydrate content on the electrical properties of porous sediments. *Journal of Geophysical Research,* 106(B4), pp. 6535-6548.

Stern, L., Kirby, S. and Durham, W., 1996. Peculiarities of methane clathrate hydrate formation and rheology, and the associated superheating of water ice. *Science,* Volume 273, pp. 1843-1848.

Stevens, J., Baldwin, B., Graue, A., Ersland, G., Husebø, J. and Howard, J., 2008. Measurements of Hydrate Formation in Sandstone. *Petrophysics,* 49(1), pp. 67-73.

Stillinger, F. H., 1980. Water revisited. *Science,* 209(4455), pp. 451-457.

Uchida, T., Takeya, S., Chuvilin, E., Ohmura, R., Nagao, J., Yakushev, V., Istomin, V., Minagawa, H., Ebinuma, T. and Narita, H., 2004. Decomposition of methane hydrates in sand, sandstone, clays, and glass beads. *Journal of Geophysical Research,* 109(5), pp. 1-12.

Uchida, T., Takeya, S., Ebinuma, T. and Narita, H., 2001. *Replacing methane with CO2 in clathrate hydrate: Observations using Raman spectroscopy.* Collingwood, CSIRO Publishing.

Wischnewski, B., Date unknown. *Peace software.* [Online]
Available at: http://www.peacesoftware.de/einigewerte/einigewerte_e.html
[Accessed 2014-2015].

Xiong, L., Li, X., Wang, Y. and Xu, C., 2012. Experimental Study on Methane Hydrate Dissociation by Depressurization in Porous Sediments. *Energies,* 5(2), pp. 518-530.

Yamamoto, K. and Dallimore, S., 2008. Aurora-JOGMEC-NRCan Mallik 2006-2008 Gas Hydrate Research Project Progress. *Fire in the Ice, Methane Hydrate Newsletter,* 8(3), pp. 1-5.

Yamamoto, K., Terao, Y., Fujii, T., Ikawa, T., Seki, M., Matsuzawa, M. and Kanno, T., 2014. *Operational overview of the first offshore production test of methane hydrates in the Eastern Nankai Trough.* Houston, Offshore Technology Conference.

Yang, J., Chapoy, A., Tohidi, B., Jadhawar, P., Lee, J. and Huh, D., 2008. *Thermodynamic Conditions and Kinetics of Integrated Methane Recovery and Carbon Dioxide Sequestration.* Houston, Offshore Technology Conference.

Yousif, M., Li, P., Selim, M. and Sloan, E., 1990. Depressurization of Natural Gas Hydrates in Berea Sandstone Cores. *Journal of Inclusion Phenomena and Molecular Recognition in Chemistry,* Volume 8, pp. 71-88.

Zhao, J., Xu, K., Song, Y., Liu, W., Lam, W., Liu, Y., Xue, K., Zhu, Y., Yu, X. and Li, Q., 2012. A Review on Research on Replacement of CH4 in Natural Gas Hydrates by Use of CO2. *Energies,* 5(2), pp. 399-419.